Ultrafast Electronic Processes at Nanoscale Organic-Inorganic Semiconductor Interfaces

Patrick Wallace Parkinson

Brasenose College

University of Oxford

A thesis submitted for the degree of

Doctor of Philosophy

Michaelmas 2008

List of published papers:

- *Dimensionality-dependent energy transfer in polymer-intercalated SnS_2 nanocomposites*, **P Parkinson**, E Aharon, MH Chang, C Dosche, GL Frey, A Köhler and LM Herz, *Physical Review B*, 75, 165206 (2007)

- *Transient terahertz conductivity of GaAs nanowires*, **P Parkinson**, J Lloyd-Hughes, Q Gao, HH Tan, C Jagadish, MB Johnston and LM Herz, *Nano Letters*, 7, 2162-2165 (2007)

- *Conductivity of nanoporous InP membranes investigated using terahertz spectroscopy*, SKE Merchant, J Lloyd-Hughes, L Sirbu, IM Tiginyanu, **P Parkinson**, LM Herz, and MB Johnston, *Nanotechnology*, 19, 395704 (2008)

- *Efficient generation of charges via below-gap photoexcitation of polymer-fullerene blend films investigated by terahertz spectroscopy*, **P Parkinson**, J Lloyd-Hughes, MB Johnston, and LM Herz, *Physical Review B*, 78, 115321 (2008)

Figure 1: Photograph of the PLUC system used in this thesis.

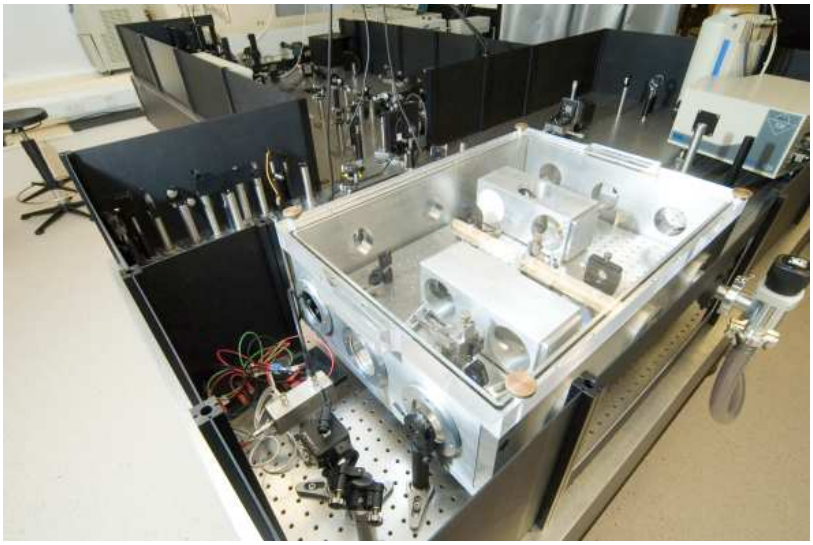

Figure 2: Photograph of the Amplifier OPTP system used in this thesis.

Abstract: Ultrafast Electronic Processes at Nanoscale Organic-Inorganic Semiconductor Interfaces

Patrick Wallace Parkinson, Brasenose College, submitted for the degree of DPhil in Michaelmas term 2008

This thesis is concerned with the influence of nanoscale boundaries and interfaces upon the electronic processes that occur within both organic and inorganic semiconductors. Photoluminescent polymers, highly conducting polymers and nanoscale inorganic semiconductors have been investigated using state-of-the-art ultrafast optical techniques, to provide information on the sub-picosecond photoexcitation dynamics in these systems.

The influence of dimensionality on the excitation transfer dynamics in a conjugated polymer blend is studied. Using time-resolved photoluminescence spectroscopy, the transfer transients both for a three-dimensional blend film, and for quasi-two-dimensional monolayers formed through intercalation of the polymer blend between the crystal planes of a SnS_2 matrix have been measured. A comparison of the experimental data with a simple, dimensionality-dependent model is presented, based on point dipole electronic coupling between electronic transition moments. Within this approximation, the energy transfer dynamics are found to adopt a three-dimensional character in the solid film, and a two-dimensional nature in the monolayers present in the SnS_2-polymer nanocomposite.

The time-resolved conductivity of isolated GaAs nanowires has been investigated by optical-pump terahertz-probe time-domain spectroscopy. The electronic response exhibits a pronounced surface plasmon mode that forms within 300 fs, before decaying within 10 ps as a result of charge trapping at the nanowire surface. The mobility has been extracted using the Drude model for a plasmon and is found to be remarkably high, being roughly one third of that typical for bulk GaAs at room-temperature and indicating the high quality and low bulk defect density in the nanowires studied.

Finally, the time-resolved conductivity dynamics of photoexcited polymer-fullerene bulk heterojunction blends for two model polymers, P3HT and MDMO-PPV, blended with PCBM are presented. The observed terahertz-frequency conductivity is characteristic of dispersive charge transport for photoexcitation both at the $\pi-\pi^*$ absorption peak (560 nm for P3HT), and significantly below it (800 nm). The photoconductivity at 800 nm is unexpectedly high, which is attributed to the presence of a charge transfer complex. In addition, the excitation-fluence dependence of the photoconductivity is studied over more than four orders of magnitude. The time-averaged photoconductivity of the P3HT:PCBM blend is over 20 times larger than that of P3HT, indicating that long-lived positive polarons are responsible for the high photovoltaic efficiency of polymer:fullerene blends. At early times ($\sim$ ps) the linear dependence of photoconductivity upon fluence indicates that interfacial charge transfer dominates as an exciton decay pathway, generating charges with mobility of at least $\sim 0.1 \mathrm{cm}^2\mathrm{V}^{-1}\mathrm{s}^{-1}$. At later times, a sub-linear relationship shows that carrier-carrier recombination effects influence the conductivity on a longer timescale ($> 1\,\mu$s).

Acknowledgements

I would like to acknowledge the help and support of many people for making the work presented in this thesis possible, and importantly, enjoyable. Primarily, I would like to thank my supervisor Dr. Laura Herz for continual help, advice and encouragement over the last three years. For help and support, particularly with the more involved aspects of terahertz spectroscopy I am indebted to Dr. Michael Johnston of the Terahertz Photonics group at the Clarendon Laboratory, University of Oxford. Additionally, I would like to thank my group members and office-mates old and new : Enrique Castro-Camus, James Lloyd-Hughes, Suzannah Merchant, Ming-Hua Chang, Xinlong Xu, Stefan Schmid, Amy Stevens, Priti Tiwana, and Carl Headley. For their support, chats, tea and general good humour, I am very grateful.

Much of the work presented in this thesis has been made possible by collaborations with colleagues from around the world. In particular: The samples studied in Chapter 4 were provided by Prof. Gitti Frey of the Department of Materials Engineering, Technion Institute of Technology, Haifa, Israel and additional spectroscopy and sample preparation was performed by Dr. Carsten Dosche and Prof. Anna Köhler from the Chemical Physics Department, University of Potsdam, Germany; The samples and the electron microscopy in Chapter 5 were provided by Dr. Michael Gao and Prof. Chennupati Jagadish of Electronic Materials Engineering Department of the Australian National University, Canberra, Australia.

I owe a huge amount of gratitude to my parents, sister, and friends in Nottingham for support, entertainment and happy distractions over the last few years, particularly when I have been getting restless in Oxford! This work is dedicated to Daniel and Matt, for a lifetime of friendship and happiness and who are sorely missed.

Lastly but certainly not least – thank you to Tasha, for being supporting, loving, caring and always smiling!

Contents

1 Introduction **1**
- 1.1 Ultrafast timescales . . . 3
- 1.2 Overview of this thesis . . . 4

2 Electronic processes in organic semiconductors **7**
- 2.1 Introduction to conjugated polymers . . . 7
  - 2.1.1 Electronic structure of carbon . . . 8
  - 2.1.2 Single particle excitations . . . 11
  - 2.1.3 Excitons . . . 13
- 2.2 Conjugated polymer spectra . . . 16
  - 2.2.1 Stokes shift . . . 19
- 2.3 Exciton dynamics . . . 22
  - 2.3.1 Fundamentals of exciton dynamics . . . 22
  - 2.3.2 Exciton migration mechanisms . . . 25
  - 2.3.3 Exciton Traps . . . 28
- 2.4 Polaron dynamics . . . 33
  - 2.4.1 DC mobility . . . 36
  - 2.4.2 AC mobility . . . 38
  - 2.4.3 Polaron trapping . . . 39
- 2.5 Inorganic Semiconductors . . . 41
  - 2.5.1 Band transport . . . 42

3 Experimental Methods **47**
- 3.1 Steady-state techniques . . . 48
- 3.2 Time-resolved spectroscopy . . . 49
  - 3.2.1 Optical pump-probe spectroscopy . . . 50
  - 3.2.2 Ultrashort amplified laser pulses . . . 50
  - 3.2.3 Non-linear optics . . . 53
- 3.3 Experimental details . . . 57
  - 3.3.1 Photoluminescence up-conversion . . . 57
  - 3.3.2 Optical-pump terahertz-probe spectroscopy . . . 63
  - 3.3.3 Extracting the complex conductivity of a sample . . . 75
  - 3.3.4 Interpretation of the photoconductivity . . . 80

4 Energy dynamics in Polymer-intercalated SnS_2 nanocomposites 83
4.1 Background : White-light emitting OLEDs . . . 83
4.2 Experimental details . . . 85
4.3 Results from time-resolved photoluminescence spectroscopy . . . 87
4.4 Discussion of dimensionality-dependent energy transfer . . . 92
4.5 Summary . . . 97

5 Transient terahertz photoconductivity of GaAs nanowires 100
5.1 Background . . . 101
5.2 Sample characteristics . . . 103
5.3 Discussion . . . 107
5.3.1 Pump fluence dependence of conductivity . . . 109
5.4 Surface Passivation . . . 112
5.4.1 Etch and passivation protocol . . . 112
5.4.2 Carrier lifetime . . . 113
5.4.3 Stability of surface passivation . . . 115
5.5 Summary . . . 116

6 Sub-gap OPTP studies of Polymer:Fullerene blends 119
6.1 Background: Organic photovoltaics . . . 120
6.2 Sample preparation . . . 122
6.3 Experimental Results . . . 126
6.4 Discussion . . . 134
6.4.1 Carrier generation and recombination . . . 135
6.4.2 Dependence of charge carrier conductivity on excitation fluence 138
6.5 Conclusions . . . 145

7 Conclusion 147
7.1 Future work . . . 150

A Pump-probe analysis for thin non-uniform media 151

Chapter 1

Introduction

Technological development in the 21st century has revolved around computing, high-speed communication, and a host of electronic devices that are used in every-day life. Since the development of semiconductor transistors in 1947 [1], efforts to improve optoelectronic and semiconductor device technology have focused upon increased speed and efficiency and reduction in cost of inorganic semiconductors, primarily silicon. However, a promising class of semiconductors known as conjugated molecular materials has also undergone 40 years of intensive research, originating with the discovery of electroluminescence in a molecular crystal – anthracene – in 1962 [2]. The earliest studies of conjugated molecular materials established that the mechanism behind electroluminescence was recombination of electron-hole pairs in a radiative process [3]. This provided evidence for the existence of a band-gap within these materials, allowing comparison with inorganic semiconductors studied in the well understood field of solid state physics [4]. More recently, the possibility of controlling the band-gap of organic semiconductors has allowed the use of a variety of conjugated polymers in many applications, including highly sensitive chemical sensors [5], field-effect transistors (OFETs) [6], solar cells (OPVs) [7] and high efficiency organic light-emitting diodes (OLEDs) [8, 9]. There are many advantages of using conjugated polymer semi-

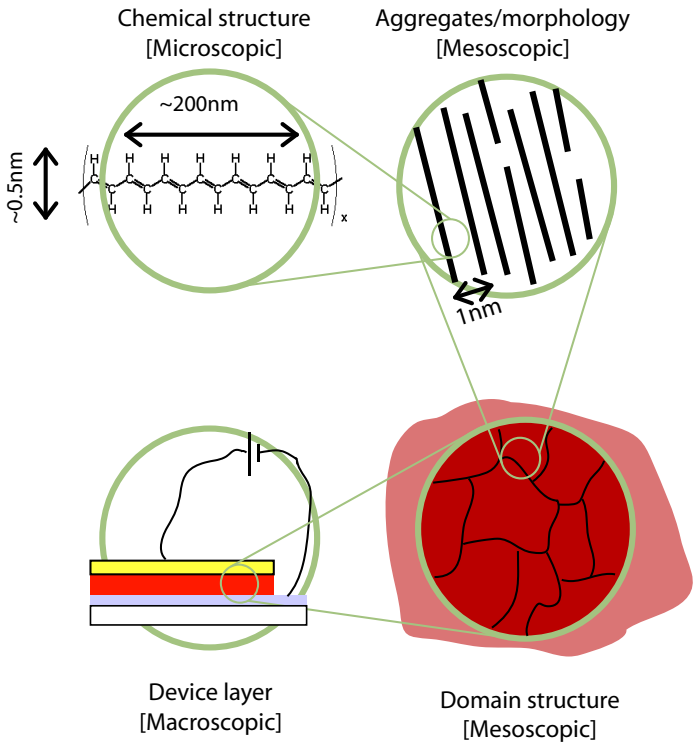

Figure 1.1: Schematic giving an example of the levels of structure within a solid-state polymeric device, such as an OLED. The dimensions given are approximate, and taken from X-ray diffraction measurements [10]. Electronic processes and coupling at every level influence the macroscopic properties of the final device.

conductors for optoelectronic devices in comparison with their inorganic counterparts, in particular, the chemical tunability of the semiconductor band-gap, and their solution processibility, which enables cheap and relatively simple roll-to-roll production of large area optoelectronics.

Although there is now a wide-scale commercialisation of organic optoelectronics – particularly in the field of OLEDs – the underlying physical processes are not well understood. This is due to the complex interplay of a host of physical processes: the interaction of the electronic and vibrational states; the electronic interactions between and within semiconducting regions; polymer aggregation; blended polymer phase segregation; and the macroscopic incorporation of these materials into devices, as shown in Figure 1.1. Systematic studies of these properties have been impeded by two major

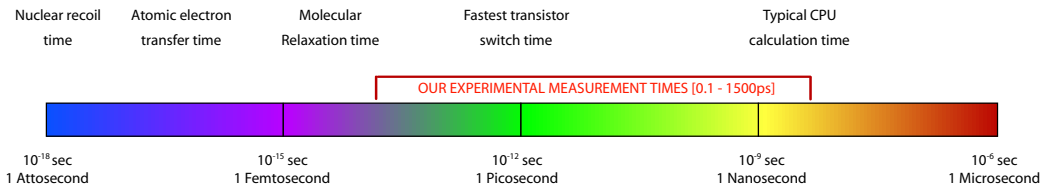

Figure 1.2: Schematic illustration of the timescales of electronic and nuclear motion in the solid-state, as well as more common markers. Also marked is the experimental time resolution of the techniques presented in this thesis.

obstacles. Firstly, the electronic processes tend to occur deep within the polymer bulk while the behaviour at the surface or at interfaces can be radically different, meaning experimental techniques requiring electrical contact to the material are inappropriate for determining the intrinsic properties. Secondly, the strong coupling between the electronic and vibrational states lead to processes which occur on ultrafast timescales, requiring experiments with an equally fast response time. The work presented in this thesis focuses on new techniques that are able to investigate electronic processes on the femtosecond (1×10^{-15} s) to nanosecond (1×10^{-9} s) timescale, using a non-contact approach.

1.1 Ultrafast timescales

The timescales over which electronic processes in organic semiconductors occur are controlled by the interactions with the polymer environment. In 'soft' polymeric systems at room temperature, the polymer lattice is able to vibrate or rotate relatively freely, which leads to quasi-particle hopping, trapping and recombination on ultrafast timescales. While these timescales are common in solid-state physics, they remain far outside of the realm of the everyday events on the human scale. On these timescales, light itself is only able to move a matter of centimetres, and great care must be taken in the designing and operation of experiments that work on these scales. Accordingly, in the time-resolved experiments discussed in this thesis, ultrashort pulses ($\sim$50 fs,

equal to 1.5 μm in length in air at the speed of light) rather than electronic devices are used as our stopwatch, and in the now common optical pump-probe experiments these pulses can be used to initiate and to measure electronic dynamics in a sample. Figure 1.2 provides a schematic view of the timescales of atomic and molecular processes, and the capabilities of the techniques presented in this thesis.

1.2 Overview of this thesis

The overarching theme of the work reported herein is the effect of nanoscale interfaces upon the electronic properties of semiconductors. As described in Chapter 2, a particular kind of interface known as a bulk heterojunction is of particular interest, where high ratio of extracted charges to incident photons is required. Chapter 2 contains a review of the literature regarding organic semiconductors and the electronic processes that occur in them. In particular, the nature and behaviour of photoexcitations are described, and the evolution of the resultant electronic state is examined. The basic theories developed in this chapter are required to explain the physics of all of the nanoscale systems reported in the remainder of this thesis.

Chapter 3 describes the experimental setups used to investigate nanoscale interfaces, and the analytical tools required to interpret the data. For the work presented in this thesis, two time-resolved systems were used: Photoluminescence upconversion spectroscopy (PLUCS) is used to determine the luminescence properties of a sample as a function of time, while optical-pump terahertz-probe time-domain-spectroscopy (OPTP-TDS) is used to investigate the dynamical conductivity of photoinjected species in semiconductors. These tools form the experimental basis for the work presented, and represent the cutting edge of non-contact ultrafast spectroscopy. The interaction of the terahertz pulse with a photoexcited system is explored, and the interpretation of the spectroscopic information in order to model the electronic

processes within the sample is discussed.

In Chapter 4, the application of nanoscale interfaces to optimise a white-light OLED is presented. White-light emission has proven to be a particular challenge for scientists working in the field of OLEDs. The traditional approach revolves around the blending of polymers with different emission wavelengths to achieve full visible-spectrum emission. While the band-gap tunability of organic semiconductors would appear to be perfectly suited to this approach, the energy transfer from sites of higher energy to those of lower energy is so rapid that emission occurs from the lowest energy sites only. In the approach reported in Reference [11], the intercalation of red (MEH-PPV), green (F8BT) and blue (F8) emitting polymers into a SnS_2 nanocomposite has resulted in stable while light emission. The physical mechanism for the reduction in energy transfer rate is explored using the PLUCS experiment. The results presented in Chapter 4 reveal that the inhibition of energy transfer is related to the dimensionality of the energy transfer, and may be predicted using existing theory.

The impact of reducing the physical size of an inorganic semiconductor is investigated in Chapter 5, in which the electronic processes that occur within photoexcited Gallium Arsenide (GaAs) nanowires are compared with their bulk counterpart. In this experiment, the nanowires have a typical size of 7 μm in length by 50 nm in diameter, and are photoexcited by an ultrafast above band-gap pulse. These dimensions are an order of magnitude larger than those necessary to observe one-dimensional quantum confinement. However, bulk-like electronic behaviour was not observed; an unexpected conductivity transient was seen, and was attributed to the presence of a quasi-particle known as a localised surface plasmon. The energy of the absorption band of the surface plasmon provides a direct handle on the carrier density within the nanowires, permitting extraction of the carrier mobility and scattering rate with relatively few assumptions. The primary findings include the ultrashort carrier lifetime in the nanoscale material (possibly due to a large surface trap density) and a

large carrier mobility of around 1/3 of that seen in bulk GaAs. The impact of surface trap states upon the carrier dynamics is explored in more detail, by treating the surface using a surface passivation technique. A decrease in trap density is observed (as expected for a surface-trap dominated system), however no significant increase is seen in the carrier lifetime. An optimised surface passivation protocol is likely to be able to allow the trap density and hence the carrier trapping rate to be controlled through an all-chemical process.

Chapter 6 returns to organic semiconductors to address the microscopic influence of a bulk heterojunction upon exciton dissociation and mobility. Two state-of-the-art polymer:fullerene blends (used for photovoltaics) are investigated using time-resolved conductivity measurements. By comparing both above- and below-gap optical excitation, a surprisingly high value of conductivity is found for the latter. The mechanism behind interfacial exciton dissociation is addressed, and our results confirm the existence of a sub-gap charge transfer state. This is an intermediate state between the mobile exciton and the fully charge-separated state, with a distinctive sub-gap absorption feature. Additionally, by varying the incident pump-powers by over four orders of magnitude we are able to observe the effect of bimolecular charge annihilation, and find that this two-particle form of charge recombination is the primary mechanism for charge loss in these systems.

Finally, Chapter 7 provides a conclusion of the work in this thesis, along with an outlook and future experiments that could extend the experimental findings reported here.

Chapter 2

Electronic processes in organic semiconductors

2.1 Introduction to conjugated polymers

The exciting applications under investigation in conjugated polymer research stem from their semiconducting nature, in turn arising from the interactions between delocalised π-electrons and polymer periodicity. The origin of the delocalisation lies in the nature of the electronic structure of covalently bonded carbon atoms. In this chapter, the fundamental origin of this semiconducting nature will be described, and the creation, transport and annihilation processes of the primary photoexcitation species will be addressed. Hückel molecular orbital theory will be introduced to simplify the quantum mechanical description of conjugated hydrocarbons. The Born-Oppenheimer approximation will be used to simplify the picture of electronic processes in organic semiconductors, and the theory of Su, Schreiffer and Heeger (SSH) will be covered to describe an early quantum mechanical approach towards describing the photoexcited species. The topic of bulk heterojunctions will be introduced, and various mechanisms behind exciton dissociation will be discussed in the

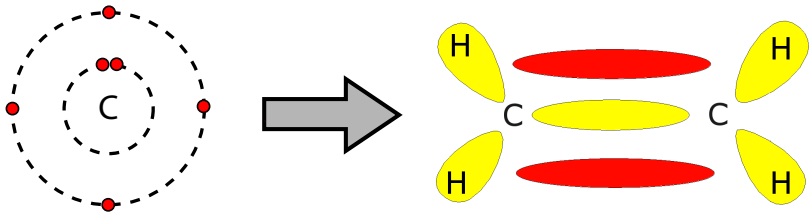

Figure 2.1: The electronic structure of carbon is shown in this schematic, along with the resultant sp^3 hybridisation upon incorporation into an Ethene molecule. Hybridisation leads to three σ orbitals forming the strong covalent bonds that provide structure (shown in yellow), and one delocalised π electron per carbon centre (shown in red).

context of improving photovoltaic device performance. Finally, energy transport and trapping mechanisms will be introduced for both charged and uncharged excitations in polymeric semiconductors.

2.1.1 Electronic structure of carbon

Carbon (C_{12}^6) has the electronic structure $1s^2 2s^2 2p^2$. When two or more carbon atoms bond, there is a possibility of single, double or triple covalent bonds forming between adjacent carbon atoms. In double or triple bonds, quantum mechanics predicts hybridisation of these electronic states, mixing the valence s and p states into 3 or 2 sp^2 (σ) bonds and 1 or 2 π bonds, respectively (see Figure 2.1) [12]. The π bond (arising from the P_z electron state) is the delocalised state, and its existence implies that the hydrocarbon is conjugated (as opposed to saturated) [13]. The conjugation length is the effective extent of delocalisation of the π electrons within the molecule, and is determined primarily by chemical structure, but also conformational structure, the presence of aromatic side groups (also known as pendant groups) or electron traps (i.e. oxygen [14]), the surrounding chemical environment (particularly polymer aggregation [15]) and boundary defects.

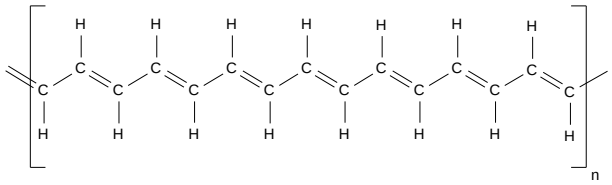

Figure 2.2: Chemical structure of *trans*-polyacetylene.

2.1.1.1 Extended polymers

Hückel molecular orbital theory (HMO) was developed from 1931 to 1937 by E. Hückel [16, 17], and presents a mathematical method to treat the properties of hydrocarbons with more than one π electron. By treating the combined wavefunction of all π electrons in a polymer as being *molecular* orbitals (as opposed to atomic orbitals) perturbed by the atomic cores, it can be shown that the quantum mechanical picture is very similar to that of a one-dimensional crystalline lattice. HMO is the equivalent of the tight-binding model used in the field of inorganic semiconductors [18]. Hückel theory is best applied to "alternant" hydrocarbons – those with alternating single and double bonds (for example *trans*-polyacetylene, Figure 2.2), providing one free π electron for each carbon core.

For the purposes of studying the electronic processes within these materials, we can neglect the electronic interactions of the σ electrons. The π electrons are the least strongly bound electrons, and therefore most easily excited. However, the σ electrons do play an indirect role as mediators of conformational and vibrational structure[1].

For a solid-state physics perspective, given one electron per atom, it would appear that an extended conjugated molecule would have a metallic conductivity – indicated by a half filled Brillouin zone, as shown in Figure 2.3a. However, it is found that alternant polymers are unstable with respect to dimerisation leading to an effective doubling of the real-space extent of the unit cell. In reciprocal k-space, this has the

[1] In the presence of certain side groups, however, the $\sigma \rightarrow \pi^*$ transition can be promoted to an energetically favourable transition.

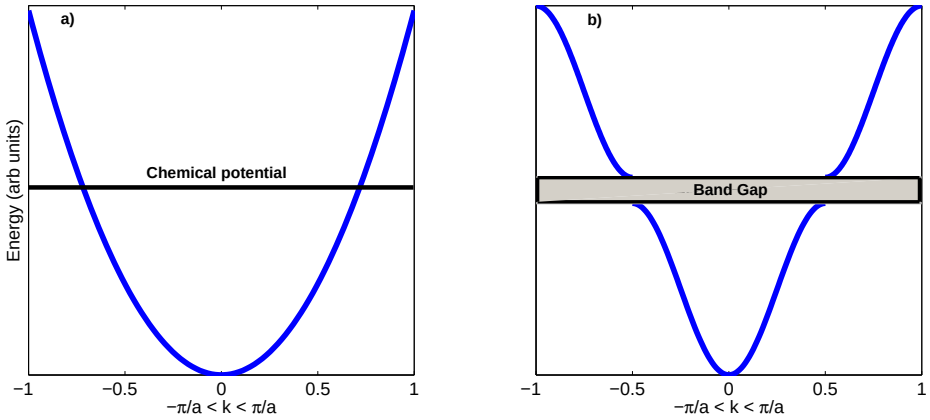

Figure 2.3: Brillouin-zone diagram of a) normal and b) dimerised conjugated polymer. Note the creation of a new gap at the original chemical potential due to dimerisation, resulting in semiconducting behaviour.

effect of producing an energy gap at $k = \pm\pi/2a$ (where a is the traditional real-space unit-cell size), corresponding to a gap at the chemical potential of the material (Figure 2.3b). By considering the similarity of this dimerisation to the Peierls effect within inorganic crystals, it can be shown that a periodic modulation of the crystal structure results (Figure 2.4) [4]. This reduces the electronic energy, in turn ensuring the stability of the dimerised state. The overall effect of this process turns the substance into an insulator, or – depending on the size of the band gap – a semiconductor. The terminology used in the field refers to the lower, valence level as the π bonding state, whilst the upper conduction band is known as the π^* anti-bonding state, with the ground state energy-gap termed $E_{\pi-\pi^*}$.

The success of HMO at describing the hydrocarbon-based conjugated polymers is based around the fact that it – similar to the tight binding model – is a symmetry rooted theory [12, 20]. As a centrosymmetric structure, the carbon backbone lends a defined axis to these polymers, allowing for traditional group-theory symmetry to be applied to our conjugated systems. With this basic theory, the fundamental excited states of the polymer can now be investigated.

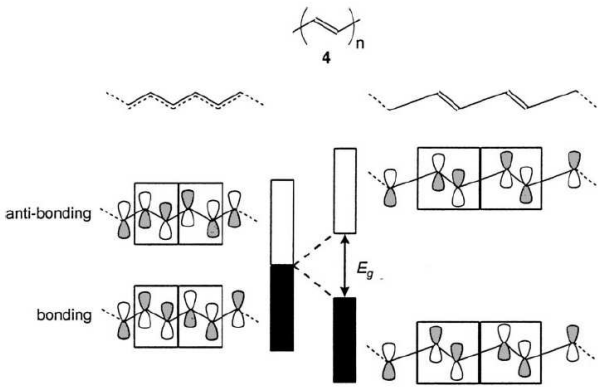

Figure 2.4: A schematic of band gap formation by localisation of double bonds in *trans*-polyacetylene. The physical effect of dimerisation is shown at the top of the figure, while the effect upon electronic states is shown below. The lowering of the ground state energy makes the dimerised state energetically favourable. Taken from Reference [19].

2.1.2 Single particle excitations

The polymer depicted in Figure 2.4, *trans*-polyacetylene, has been quantum mechanically modelled using a tight-binding Hamiltonian by Su, Schreiffer and Heeger in 1979 [21, 22]. The fundamental charge carrier in the system was shown to be a *soliton* rather than a band excitation (as would be expected in room temperature inorganic semiconductors). A soliton can be understood to resemble a moving domain wall between two conjugated segments, and – as a quasi-particle – has an associated charge, mass, spin and energy. The effective mass of a soliton on *trans*-polyacetylene is estimated to be approximately $m_s^* \approx 6m_e$ leading to a relatively mobile carrier, with an energy in the middle of the band-gap [21]. Solitons may be unoccupied states, or may be occupied by an electron or hole leading to an electronic charge of $(0,+e,-e)$ and a spin of $(1/2,0,0)$ respectively. All of these states have an energy in the middle of the band-gap, however, a further solution to the quantum mechanical model was shown to exist by Campbell and co-workers [23]. This newly discovered state corresponded to a polaron, the quasiparticle representing the interaction of a charge carrier and a phonon. This state turns out to be more general than the soliton state, as it does

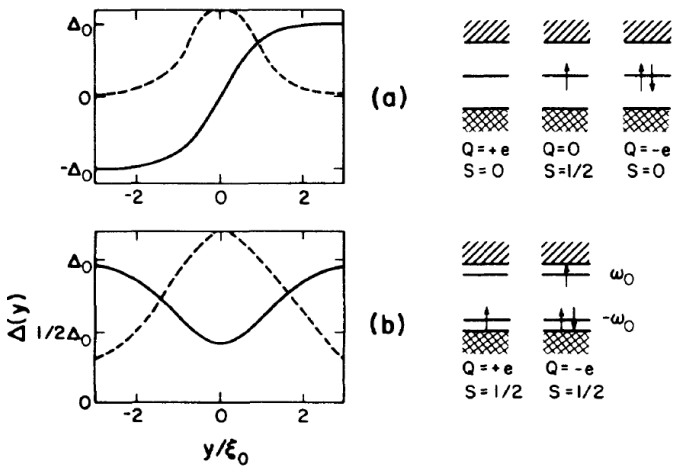

Figure 2.5: A comparison of the "gap parameter" and electron density (solid line and dashed line) for a) a soliton and b) a polaron, as a function of the on-chain position. The schematic to the right shows the positioning of the states within the band-gap, in various states : a) positive, neutral and negatively charged solitons and b) positive and negatively charged polarons. In the caption, Q represents the quasi-particle charge, and S represents the spin. Taken from Reference [24].

not require a degenerate ground-state polymer. The energy of the polaron does not lie at the centre of the gap, but is composed of two localised one-electron eigenstates with energies that lie in the band-gap at $\epsilon = \pm\hbar\omega_0$, where ω_0 is related to the phonon energy [24]. Figure 2.5 schematically depicts the difference between the two types of quasi-particles, soliton and polaron. The study of solitons or polarons is of particular importance in the field of doped organic semiconductors and where long-lived charge states exists, and (in the case of polarons) sub-gap optical absorption states can be seen using standard spectroscopic techniques. In the work presented in this thesis, only polarons will be considered.

Polarons in organic semiconductors are usually associated with mono-polar injection, either through doping [25] or electrical injection [26, 27]. As will be explained in the next section, photoexcitation rarely leads to efficient charge generation and excitons are the typical photoexcited species. Photogeneration rates for polarons in pristine polymeric semiconductors lie in the region of 10^{-3} to 0.1 polarons per inci-

dent photon [28]. Sections 2.3.3.1 and 6.4 have more detail on the mechanisms behind charge generation in organic semiconductors.

2.1.3 Excitons

In the majority of undoped organic semiconductors at room temperature there are very few free carriers in either the conduction or the valence bands. The absorption of a photon by a π electron in the valence level will result in its promotion into the conduction band, and the creation of a hole in the valence band. The lack of intrinsic free carriers leads to a low-level of electronic screening, and allows for the interaction of the electron and hole to form a hydrogenic system known as an exciton. Excitons in general can be separated into two species – Wannier-Mott excitons with a large radius of orbit and low energies; and Frenkel excitons with small radii and larger binding energies. In conjugated polymers, the excitons created are local to the molecule, indicating Frenkel-type excitons. Polarisation studies by Raucher *et al.* have shown that the primary photoexcitation modes in conjugated polymers are indeed excitons, rather than free carriers [29]. In the case of poly(para-phenylenevinylene) (PPV), Chandross *et al.* have shown the primary photoexcited species to be excitons, requiring the inclusion of explicit Coulombic interactions to describe the electronic state of the conjugated system [30, 31]. For this reason, we can describe these neutral excitations as a fundamental energy carrier in most conjugated polymers, and their movement as the fundamental pathway for energy migration.

The definition of exciton binding energy (E_g) in organic semiconductors is more complicated than that of their inorganic counterpart, due to the strong coupling between the polymer backbone geometry and the excitonic state. A good working definition can be found in Reference [32], in which Brédas *et al.* suggest that the binding energy is the difference in energy between creating the excitonic state, and the creation of two oppositely charged, spatially separated and geometrically-relaxed

polarons. Theoretical predictions and experimental measurements of the binding energy of excitons have widely varied in the literature. Chandross *et al.* have shown E_g of 0.9 eV in MEH-PPV, however energies from 0.4 eV [33] to 1.1 eV [34] have been suggested in similar polymeric systems. Typically a distribution of exciton binding energies will exist in a polymeric system. This is because of the distribution of conjugated segments, each with specific electronic properties. It is often useful to introduce the concept of 'spectroscopic units' – a synonym for conjugated segments – to describe a portion of a polymer chain with a single unbroken conjugated segment and associated energy levels and electronic dipole moment. Breaks in the conjugation may arise from bond dislocations, physical breaks, twists or the presence of electron donating or accepting dopants. By comparing the spectrum of PPV polymer to PV oligomers, Woo *et al.* estimated the typical spectroscopic unit length to be between 10 and 17 phenyl rings [35].

2.1.3.1 Exciton creation-photoexcitation

Excitons can be created in any of the ways available to excited electronic states. In many experimental scenarios, direct optical excitation is used[2]. As a photon is a spin-1 particle, it can only excite an exciton into a spin singlet state, unless higher order, multi-photon excitation occurs. However, if, due to the specific symmetry of the polymer, the triplet state lies at a lower energy than the singlet state, the exciton can non-radiatively decay into a triplet state via a vibrational transition involving spin-orbit coupling (known as an intersystem crossing, and to be discussed later).

Until this point we have assumed that the polymer backbone does not react to the creation of an exciton, except as a static background field. However, as the creation of a mobile exciton leads to removal of a π-conjugated electron from the backbone,

[2]For spectroscopic measurements, photoexcitation is typically used, whilst for device measurements, electrical injection of charges is more common. An exception is charge-modulation spectroscopy, where the differential absorption spectrum is measured with and without injected charges. In the current thesis, only photoexcitation is used.

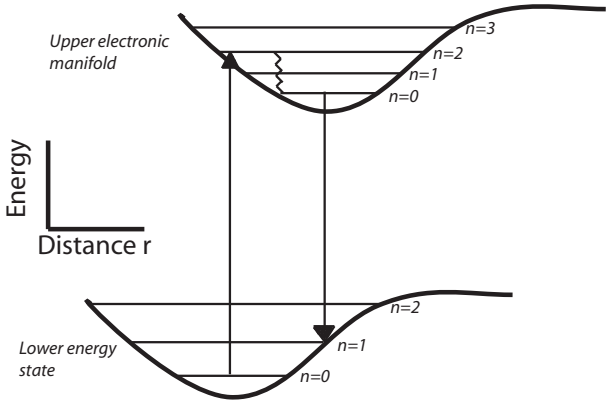

Figure 2.6: Molecular potential energy curves, with Franck-Condon transitions indicated by vertical arrows. The transition denoted with a wavy line is a non-radiative transition between a higher vibrational state of the upper electronic state, and the ground vibrational state. The difference in energy between the excitation transition and the emission transition is the Stokes shift. Adapted from Reference [36].

creating a saturated bond, we would expect a dynamical change in the conformation of the polymer. This, in turn results in a time-varying potential in which the exciton may respond. This could lead to an extremely complicated picture, in which the electronic response is strongly coupled to the polymer backbone relaxation, and vice versa. The solution to this is expressed in the Franck-Condon principle (as depicted in Figure 2.6), which states that during an electronic transition, the electronic state changes so fast that the conformational change can be neglected. This leads to the Born-Oppenheimer approximation, that the change in distance between nuclei is negligible over the time period of the electronic transition [36], or more formally, that the true molecular wavefunction of a conjugated polymer may be adequately separated into $\Phi = \phi_{\text{electronic}}\phi_{\text{nuclear}}$ on the timescale of an electronic transition, where $\phi_{\text{electronic}}$ and ϕ_{nuclear} are the wavefunctions of the electronic state and the nuclear conformational state, respectively [20]. The interaction is not negligible at later times however, and the Born-Oppenheimer approximation cannot be used for the long-term analysis of the spatial migration and energy evolution of the exciton.

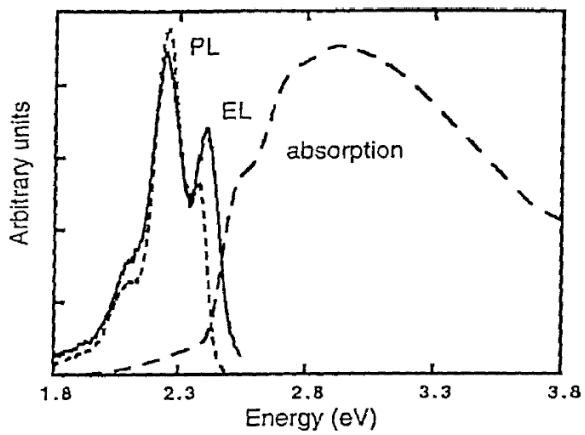

Figure 2.7: The optical absorption, photoluminescence (PL) and electroluminescence (EL) of a typical conjugated polymer (PPV, poly(phenylene vinylene)) are shown. Note the shift in energy between the peak absorption and peak emission, and the strong structure visible in the luminescence. Taken from Reference [37].

2.2 Conjugated polymer spectra

Both the emission and absorption spectra of conjugated polymers arise due to the distribution of energy levels in the ensemble of spectroscopic units; these are in turn a result of the interaction of the carbon molecular spectra, with perturbations due to the extended delocalisation of the π-electrons, the Peierls effect, on-chain vibrational modes, and excitonic processes to name but a few. The most important factor determining the shape of the absorption spectrum is that of the band-gap formed by the Peierls effect. A typical absorption spectrum is shown in Figure 2.7. We can begin to understand and even predict the shape of the absorption and emission spectrum by considering the processes involved linking the electronic and vibrational energy levels in the polymer.

Conjugated polymers are only able to absorb above band-gap radiation, with the minimum energy required being the difference between the highest energy vibrational level in the lower band (known as the HOMO, highest occupied molecular orbital) and the vibrational ground state of the conduction band level (the LUMO, or lowest

unoccupied molecular orbital). Because of the strong coupling between the polymer backbone and the electronic state, electronic transitions are typically accompanied by vibrational motion, forming what is termed a vibronic transition. As stated above, while these are strongly associated, within the Born-Oppenheimer approximation, the energy of a molecule can be separated into

$$E_t = E_e + E_v + E_r \tag{2.1}$$

referring to the electronic, vibrational and rotational components of the energy - we may consider there to be no direct coupling. These are given in order of relative magnitude, with typical energies of the electronic transitions being in the visible region ($\sim$ 2 eV), vibrational transition in the near infra-red ($<$ 1 eV to as low as 1 meV) [38], and rotational energies in the far infra-red ($\sim$meV) [36].

Following the procedure in Reference [39], the rate of emission or absorption may be given by Fermi's Golden rule,

$$W_{if} = \frac{2\pi}{\hbar} \left|\mathbf{M}_{if}\right| g(\hbar\omega) \tag{2.2}$$

where $g(\hbar\omega)$ is the density of states at a specific photon energy, and $\mathbf{M}_{if}$ is the matrix element of the transition, given by,

$$\mathbf{M}_{if} = \langle \psi_{final} | V(\mathbf{r}) | \psi_{initial} \rangle \,. \tag{2.3}$$

For electromagnetic photon-mediated transitions, $V(\mathbf{r})$ is given by the electric dipole moment interaction. The potential representing the interaction of a photon with an electric dipole is given by,

$$V(\mathbf{r}) = e\mathbf{r}.\mathbf{E}, \tag{2.4}$$

where $\mathbf{E}$ is the electric field and $\mathbf{r}$ is the effective dipole vector. Note that the form

of Equations 2.3 and 2.4 requires the parity of the wavefunction to change during the transition. We can describe the total molecular wavefunction as

$$\phi = \psi_j(r, Q)\chi_{jm}(Q)\psi_{\mathrm{s}}, \tag{2.5}$$

where the first term represents the electronic component – j denotes the electronic state – as a function of r and Q, the electronic and nuclear (configurational) coordinates of the system. The second term represents the vibrational component, where m is the vibrational state within the jth electronic state. The final term, ψ_{spin}, represents the spin state of the system. The Franck-Condon principle implies that the electronic dipole moment in Equation 2.4 interacts only with the electronic state; in this case, the rate can be separated and expressed as

$$\mathbf{W}_{if} \propto \left|\left\langle \psi_{e_i}|V(\mathbf{r})|\psi_{e_f}\right\rangle\right|^2 \left|< \chi_{v_i}|\chi_{v_f} >\right|^2 \left|< \psi_{s_i}|\psi_{s_f} >\right|^2 \tag{2.6}$$

where the first term arises from the electronic wavefunction overlap under the effect of the dipole moment operator, the second term represents the vibrational state overlap, and the third term occurs due to the spin projection of the electron. It is important to note that as a consequence of the Franck-Condon principle and the negligible momentum of a photon, direct transitions from the ground state are often to a vibrationally excited state of the upper state (see Figure 2.6). This equation is valid both for photon absorption and photon emission.

If any term in Equation 2.6 is zero, then the transition becomes forbidden. One such situation occurs when a singlet exciton non-radiatively decays to a triplet state (intersystem crossing). Decay to the ground state would then be a spin-forbidden transition, and is prevented by the Pauli exclusion principle[3]. As there is threefold

[3]The processes in which triplet-excitons may radiatively decay is known as phosphorescence, however, this typically occurs at a much lower rate than the fluorescent decay of singlet states.

degeneracy in the triplet system, if it is energetically favourable to allow full mixing between spin states and the lifetime of the excitons τ_{ex} is significantly longer than the intersystem crossing time τ_{isc}, up to 75% of the initially photogenerated excitons will result in triplets.

2.2.1 Stokes shift

Once an excited state has been formed, a variety of processes are available. Neglecting intrachain and interchain energy migration (to be discussed in a later section), we consider the excited state to remain localised. As a consequence of the Franck-Condon principle, at some point following the electronic transition, the polymer backbone will begin to relax before emitting a photon. A four stage processes occurs, as demonstrated in Figure 2.8. In the special case near nuclear equilibrium, the molecular potentials can be assumed to be parabolic and the potential minima will be separated by a configurational coordinate ΔQ which represents the change in the polymer backbone geometry between the ground ($m = 0$) and excited state. Under this approximation, the term $\left|< \chi_{v_i} | \chi_{v_f} >\right|^2$ – known as the Franck-Condon factor f – can be calculated analytically and expressed as

$$f_{0,f} = \frac{S^m}{m!} e^{-S}, \tag{2.7}$$

where m is the vibrational mode number. S is known as the Huang-Rhys factor and is equal to [36]

$$S = \frac{1}{2} \frac{k(\Delta Q)^2}{\hbar\omega}. \tag{2.8}$$

In Equation 2.8, k is the force constant of the vibrational motion and $\hbar\omega$ is the phonon energy. The Huang-Rhys factor is related to the number of phonons that are emitted during the configurational relaxation, therefore $S\hbar\omega$ is approximately the energy difference between the unexcited ground state and exited ground state energy,

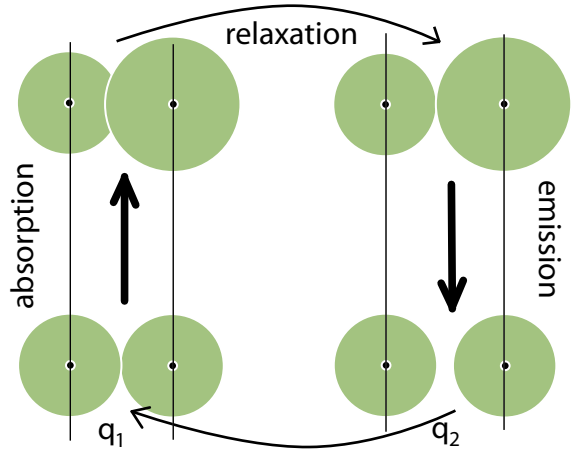

Figure 2.8: Schematic representation of the processes that occur during vibronic transitions, where q_1 and q_2 are the equilibrium separations of the nuclei in the ground and excited states. The first step is absorption of a photon, resulting in a change in the bond-lengths in the material. Secondly, and over a slower timescale, the bonds relax to their excited equilibrium position. At a later time, a photon is re-emitted, returning the system to the ground electronic state. Finally, the bonds relax back. Adapted from Reference [13].

known as the 'Stokes shift', as demonstrated schematically in Figures 2.8 and 2.9 [40]. As the emission of a phonon is a fast processes in comparison with the lifetime of the excited electronic state of the system, both emission and absorption of photons tend to occur from the lowest excited vibrational state. This is known as Kasha's rule[4]. The most common phonon modes that couple to the electronic state are carbon-carbon stretching and ring breathing, both with energies in the region of 0.2 eV, which give rise to the characteristic shape of the absorption and emission spectra in conjugated polymers. Also shown in Figure 2.9 is the possibility of spectral overlap between emission and absorption. This becomes important in allowing exciton migration, as described in the next section.

[4] *"The emitting level of a given multiplicity is the lowest excited level of that multiplicity"* [41]. This rule is not strict however, and has been found to have exceptions.

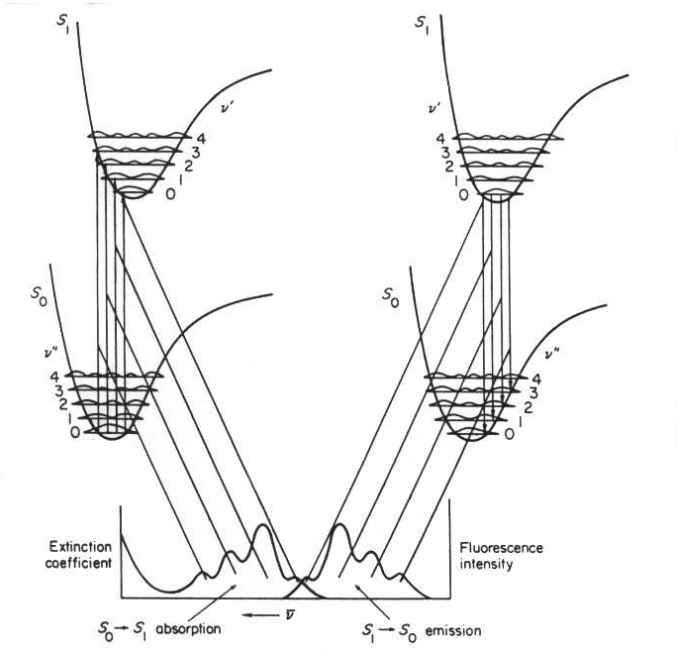

Figure 2.9: Simplified potential energy curves demonstrating how a mirror-image relationship can arise between absorption and emission bands. Taken from Reference [42].

2.2.1.1 Broadening

In reality, when considering the bulk properties of conjugated polymers a variety of real-world processes act to change the absorption and emission spectrum. Broadening of a spectrum can be attributed to four main causes: inhomogeneity in the exciton energy due to the distribution in polymer conjugation length, a variation in polymer local chemical environment, torsional vibration leading to closely spaced replica (typically separated by tens of meV) and finally due to lifetime-limiting effects, such as intermolecular collisions (in solution). The absorption spectrum tends to be broader than photoluminescence spectrum, as while all spectroscopic units take part in the absorption process, the down-hill exciton dynamics within a bulk polymer lead to preferential emission from spectroscopic units in a low-energy subset of states.

2.3 Exciton dynamics

The lifetime of excitons within conjugated polymer systems can be long compared to the timescale of vibrational effects, and are typically in the tens to hundreds of picoseconds regime [43]. In this time, the excitons are able to migrate between spectroscopic units upon the same molecule (often termed energy migration) and those in separate molecules (termed energy transfer) via a variety of processes.

The mechanism underlying either migration or transfer depends on the physical size of the jump and the energetic reward for the process. The longest range mechanism is photon emission and re-absorption, with no limit on the distance of the jump (it is the only mechanism that occurs when the donor and acceptor spectroscopic units[44] are $\gg$ 100Å). However, an overlap between the fluorescence spectrum and the absorption spectrum is essential. The next most distant process is accounted for by a resonant or Förster transfer. This also requires a spectral overlap between the donor emission spectrum and acceptor absorption spectrum[5]. The mechanism is a coherent dipole-dipole interaction, and will be the main method we consider for intermolecular transfer. Finally, as the exciton may initially be considered to have the same size as that of the spectroscopic units, intramolecular migration may occur when the wavefunction of the exciton extends into a neighbouring conjugation region – simply put, quantum mechanical tunnelling. The relative importance of these mechanisms has been modelled by Beljonne *et al.* [45].

2.3.1 Fundamentals of exciton dynamics

Excitons are understood to migrate along a polymer backbone through inter-atomic coupling. This takes the form of a random walk, as modelled in Reference [45]. The extended delocalisation of the π electrons acts as a sea through which excitons may

[5]In the case where the donor and acceptor spectroscopic units are of the same chemical species, this overlap will be determined by the Stokes shift, as described in Section 2.2.1.

permeate. Following the extensive model presented by Bässler *et al.* we may consider the polymer as a network of sites with positional and energetic disorder [46, 47]. The energetic disorder is simulated by a variation in the density of states.

The excitons tend to migrate from spectroscopic units of higher energy to those of lower energy. This effect has been experimentally observed in time-resolved fluorescence spectroscopy; the time-resolved spectra of the excitons exhibits a red-shift with increasing time (Figure 2.10) [48, 49]. It has also been observed by Müller *et al.*, using site-selective single molecule spectroscopy [50]. The lowest energy state (where the excitons will tend to end up) will be the section of backbone with the longest conjugation length. However, not all emission occurs from the low energy sites – emission often occurs before the excitation reaches this section, and it is possible that energy will become stuck in a non-radiative trap. For instance, in isolation and in a pure sample, the overall intensity of emission drops exponentially with time, reflecting the decay in exciton population. However, in blended host-guest systems [51], or systems with specific exciton dissociation sites [52], the exciton lifetime will follow a more complex model; Chapters 4 and 6 have more details on this topic.

In addition to spectral overlap, an important parameter may be the physical separation of conjugated regions. For instance, if *trans*-polyacetylene were to undergo a conformational change to *cis*-polyacetylene, conjugation regions become separated and wavefunction tunnelling migration becomes less effective than other mechanisms. It has been suggested that intrachain migration can be promoted by enforcing a rigidly linear conformation of the polymer backbone, and experimental evidence seems to support this theory [43, 49, 54]. The case of intramolecular and intermolecular energy transfer are treated separately below; in all but the most pathological cases such as single molecule spectroscopy [55], or extreme dilution in a matrix [56], both types of transport will be present. In a bulk solid, a suitable energy offset between polymer chains [51] or the appearance of mesoscopic ordering may even lead to the promotion

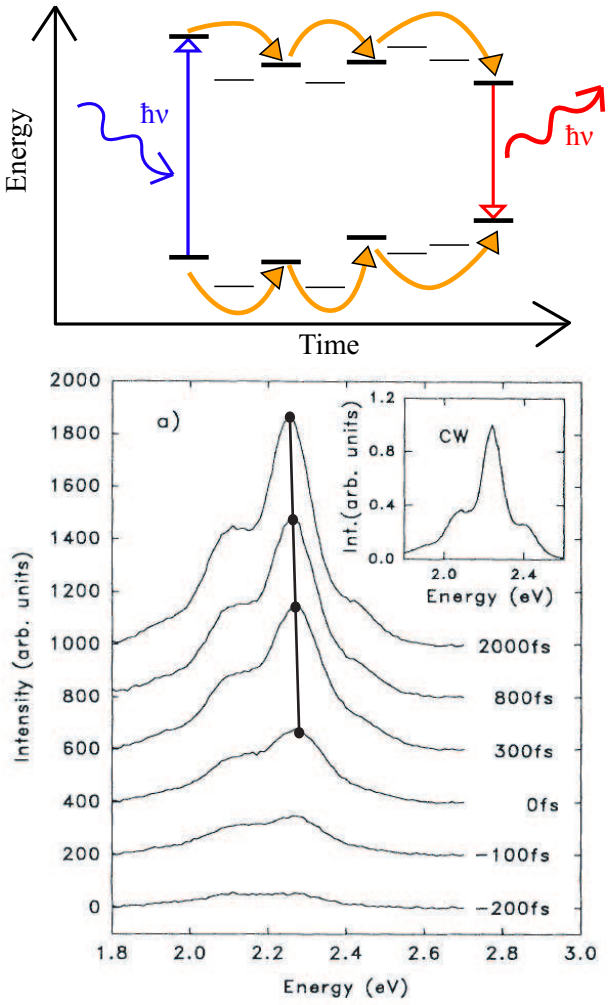

Figure 2.10: The downhill energy dynamics are depicted; the upper pane schematically shows the time evolution of the exciton energy with an initially high energy exciton migrating to lower energy sites before emitting a lower energy photon, while the lower shows typical fluorescence data taken by Kersting *et al.* [53] showing the resulting redshift over the first two picoseconds.

of interchain energy transfer over intrachain.

2.3.2 Exciton migration mechanisms

In the trivial re-absorption case described above, the donor exciton recombines emitting a photon, which is absorbed by a remote acceptor. This processes has the net effect of appearing to extend the exciton lifetime, typically from τ to somewhere on the order of 2τ [36]. It must be taken into account when considering time resolved spectroscopy, as the higher energy photons are more readily reabsorbed (due to enhanced spectral overlap with the absorption spectrum), leading to a lifetime extension at higher energies; it may be avoided by preparing thin solid samples with a low optical density. A standard photoluminescence experiment will normally be arranged such that re-absorption has a negligible effect on the measurements.

2.3.2.1 Förster transfer

Förster transfer is described by a coherent quantum mechanical model. For allowed singlet transitions, this is the primary mechanism of energy transfer. The theory was first developed by J. and F. Perrin [57, 58], but extended by Förster in 1948 [59, 60]. It is a non-radiative, Coulomb-mediated interaction; for a two molecule system (A and D denote the acceptor and donor, respectively) the process is given by $D^* + A \rightarrow D + A^*$ where the excited states are marked with *. In this case, the wavefunction of the excitation is described by the linear superposition,

$$\psi_{\mathrm{TOT}}(t) = C_1(t)\psi_A^*(t)\psi_D(t) + C_2(t)\psi_A(t)\psi_D^*(t). \tag{2.9}$$

The coefficients are constructed such that $|C_1(t)|^2$ and $|C_2(t)|^2$ describe the probability of the excitation occurring on the donor or acceptor.

The rate of transfer was modelled by Perrin [58] as being proportional to the

electromagnetic interaction between the electric field due to the exciton and the dipole moment of the acceptor,

$$K_{D\to A} \propto \mathbf{E}_D.\mathbf{p}_A \propto \left[3(\mathbf{r}.\mathbf{p}_A)(\mathbf{r}.\mathbf{p}_D) - \mathbf{p}_A.\mathbf{p}_D\right] \frac{1}{R^3} \tag{2.10}$$

where $\mathbf{p}$ is the dipole moment, $\mathbf{E}$ is the electric field vector, and R is the mean separation between donor and acceptor molecules. This is valid in the 'strong coupling regime', where the intermolecular electronic interaction is stronger than the vibrational coupling. It was found that this R^{-3} dependence was not representative; in 1948, Förster recognised that this was only valid if the donor and acceptor wavefunctions remained coherent throughout the transfer [59, 60]. Due to the rapid relaxation of vibronic transitions, the acceptor quickly dephases as it non-radiatively decays to the ground vibrational state during the transfer. Förster's addition to the understanding of this interaction led to the concept of the 'very-weak-coupling' limit transfer rate,

$$K_{D\to A} = \frac{1}{\tau_D}\frac{1}{R^6}\left(\frac{3}{4\pi}\int \frac{c^4}{\omega^4 n_0^4} F_D(\omega)\sigma_A(\omega)\, d\omega\right) \tag{2.11}$$

where $F_D(\omega)$ is the fluorescence emission spectrum of the donor, and $\sigma_A(\omega)$ is the acceptor absorption cross section. By collecting the terms constant over the polymer, the transfer rate can be expressed in terms of a critical distance R_0,

$$K_{D\to A} = \frac{1}{\tau}\left(\frac{R_0}{R}\right)^6 \tag{2.12}$$

which was found to fit the data more accurately.

2.3.2.2 Excitonic tunnelling and exchange

It is also possible – in highly aggregated materials – for excitons to tunnel between polymer strands as neutral excitations via intermolecular orbital overlap (IOO). As

only singlet (emissive) excitons may be transferred through the Förster and trivial re-absorption interactions, IOO is the only mechanism available to triplet states. In polymer ensembles with a high level of mesoscopic ordering, this can lead to the delocalisation of the exciton in two-dimensions, creating what are known as "intermolecular exciton states" [61, 62]. In addition, electron exchange (Dexters mechanism) is one example of a non-radiative energy transfer mechanism, and has a rate exponentially proportional to the donor-acceptor separation. Combining these coupling regimes requires modelling coherent, incoherent, and classical approaches [36]. Kenkre and Knox developed an approach based up generalised master equations [63, 64] able to model both the strong and very-weak coupling regimes.

2.3.2.3 Excitation transfer in an ensemble

Equation 2.12 describes the interchain Förster transfer rate between a single donor-acceptor pair. In reality, the pair is unlikely to exist in isolation; an ensemble must be considered, requiring a spatial average of this rate over the extent of the bulk polymer. For the three-dimensional case we may follow the derivation in Reference [65] and write the time dependent density of excitations as

$$\bar{\rho}(t) = \exp\left(-\frac{t}{\tau_D} - \beta t\right) \tag{2.13}$$

where τ_D is the characteristic lifetime of the excited donor state, and

$$\beta = \sqrt{\pi}\frac{c_A}{c_0}\frac{1}{\sqrt{\tau_D}}. \tag{2.14}$$

Here, c_A represents the concentration of acceptors in the ensemble, and c_0 is a critical concentration. This model has been extensively investigated for a variety of molecular and supra-molecular substances [51, 66–69]. The effect of dimensionality on donor-acceptor excitation transfer is investigated in more detail in Chapter 4.

2.3.3 Exciton Traps

After the excitation of an exciton in a molecule, energy transfer occurs until the exciton decays – radiatively or non-radiatively – or is trapped. Traps arise due to substituting aromatic groups on the polymer with heavy atoms, or electron withdrawing groups. Heavy atoms have a large spin-orbit coupling effect, which promotes the intersystem crossing [36]. This converts radiative singlets states into non-radiative triplet states. Electron withdrawing groups (for instance carbonyl or nitro compounds) remove electrons from the π band. This can cause a break in conjugation, and also present a de-excitation pathway through intersystem crossing. In addition, many nitroaromatics undergo photodegredation, causing unpredictable behaviour upon illumination. Whilst in organic-light emitting diode applications exciton trapping or dissociation may be seen as a problem, in the field of organic photovoltaics exciton dissociation is encouraged. In this thesis, the topic of extrinsic exciton trapping is not discussed – however, exciton dissociation plays an important part in much of the work presented.

2.3.3.1 Exciton dissociation

Exciton dissociation in organic semiconductors appears to have many possible causes, some of which are addressed in Chapter 6. These can usefully be divided into *intrinsic* and *extrinsic* effects, where the latter refers to dissociation at interfaces, defects or device-contacts. Intrinsic dissociation refers to on-chain effects that occur within the bulk of a homogeneous material. Many such effects have been suggested; some of the most referred to include:

- **Onsager model.** Onsager theory [70] suggests that the exciton dissociation rate is related to the initial separation of the electron and hole. This model has been widely applied, and has been shown to hold for materials such as amorphous selenium [71] as well as polymers like PPV-amine chains [72] and

PPV [73]. Both increasing the temperature or an applying an electric-field assist electron-hole separation by increasing the intra-pair distance. Köhler *et al.* showed that excitations far above the band-gap have a larger electron-hole separation in MEH-PPV, and used INDO and SCI quantum chemical calculations to model the excitonic wavefunction [74]. This is in agreement with the Onsager model, and may provide a quantum mechanical extension to this theory.

- **Hot exciton dissociation.** If excitons are created with photons of energy far above the polymer band-gap, they are called "hot excitons". The interpretation of Arkhipov *et al.* is that the excess energy above that required for generation of a ground state singlet is rapidly transferred into the thermal modes of the polymer chain, which can then provide a suitable quantity of energy to permit exciton dissociation [75, 76]. This was shown for the cases of PPV-amine and MeLPPP, by using an external electric field to provide energy to fully dissociate the on-chain excitons, after using excitation at various energies. In this case, the background or bath temperature of the system is relatively unimportant in comparison with the localised heating due to above-gap excitation.

- **Disorder-assisted dissociation.** While hot exciton dissociation has been observed and modelled extensively, there is considerable evidence for charge generation in certain systems where photoconduction starts at the band-gap. In a work by Albrech *et al.* the energetic impetus for exciton dissociation has been attributed to the disorder present in the density of states [77]. It is suggested that at early times, the excitations are at the top of the density of states, and may migrate freely; a electron-hole separation sufficient for dissociation may be achieved via this migration.

- **Mesoscopic structure.** In pure polymers with a high level of regioregularity, self-organised aggregates are known to form; of particular interest for this work

is the case of poly(3-hexylthiophene) (P3HT), which forms two-dimensional lamellae structure. Many features have been attributed to this structure, for example the appearance of intermolecular emissive states [61, 62], enhanced charge mobility [78] and rapid exciton dissociation [79].

- **Two-photon assisted dissociation.** Silva *et al.* reported efficient exciton dissociation using an intense excitation pulse, for which two-photon effects become significant [80]. Ultrafast exciton dissociation with 10% efficiency was presented, compatible with resonant sequential excitation. This term is used to refer both to two-photon absorption, and sequential excitation of a photoexcited state.

Due to the large binding energy of excitons in organic semiconductors, the photon to polaron branching ratio remains low under typical (i.e. solar) conditions. With the exception of mesoscopic-ordering-assisted or two-photon assisted separation, it remains difficult to construct high-efficiency organic photovoltaics. For this reason, extrinsic dissociation sites must be used to enhance the dissociation efficiency.

2.3.3.2 Extrinsic dissociation – bulk heterojunctions

Although the concept of bi-layer heterojunctions are common from the field of inorganic semiconductors, they are typically used to affect the electronic bands of the material at the interface. In polymeric semiconductors, however, they may form specific sites that encourage exciton dissociation [81]. The inherently short exciton diffusion distance in most polymers require the interface to lie with 5-10 nm of the exciton creation site for it to affect the exciton dynamics [52, 82]. In general, for a bi-layer system this limits the impact of heterojunction interfaces to a small volume fraction of the material. In 1992, Sariciftci *et al.* presented the first polymer-fullerene heterojunctions [83]; this was followed in 1995 by the development of the bulk (interpenetrating) heterojunction for photovoltaic applications by Halls [84] and Heeger [85]. Rapidly

the application of these techniques to photodiodes and photovoltaic devices became commonplace. A bulk heterojunction (BHJ) is the liquid-phase blending of two different (primarily organic) semiconductors. After deposition and drying of the blend, a composite is formed in which the two components are fully interdispersed. This in turn ensures that a large fraction of the bulk volume lies within a few nanometers of an interface.

The underlying principle of bulk heterojunction photovoltaics is shown in Figure 2.11. The first step, exciton generation, is relatively well understood, while the second step may be described by the exciton diffusion mechanisms stated earlier in this chapter. However, the mechanism behind charge separation at BHJ interfaces is not so well understood – it is known that the rate of dissociation depends on the energy levels of the two materials being optimised for separation of the exciton. Several experimental approaches have been made to understand this dissociation mechanism. Morteani and co-workers presented a model based upon exciplex formation at polymer heterojunctions, and used electric-field dependent photoluminescence spectroscopy to indicate that an interfacial exciplex is a general feature in type II heterojunctions [86][6]. More recently, Hwang *et al.* used ultrafast transient absorption to investigate the exciton dissociation process; a two-step process was observed, with ultrafast exciton transfer into an intermediate charge-transfer (CT) state, followed by charge transfer of the electron to the fullerene and the hole to the polymer [81]. The intermediate CT state is conceptually similar to the exciton being stretched at the interface, reducing the binding energy sufficiently to permit thermal dissociation. The inclusion of an intermediate step is also suggested by Goris *et al.*, in which an extremely sensitive absorption technique was used, and a sub-gap absorption band was attributed to the intermediate CT state [87]. Later work by Benson-Smith *et al.* observed sub-gap photoluminescence from this state, and observed the appearance of

[6]Type II heterojunctions are those where both the HOMO and LUMO levels of one component are offset in the same direction with respect to the other component, as shown in Figure 2.11.

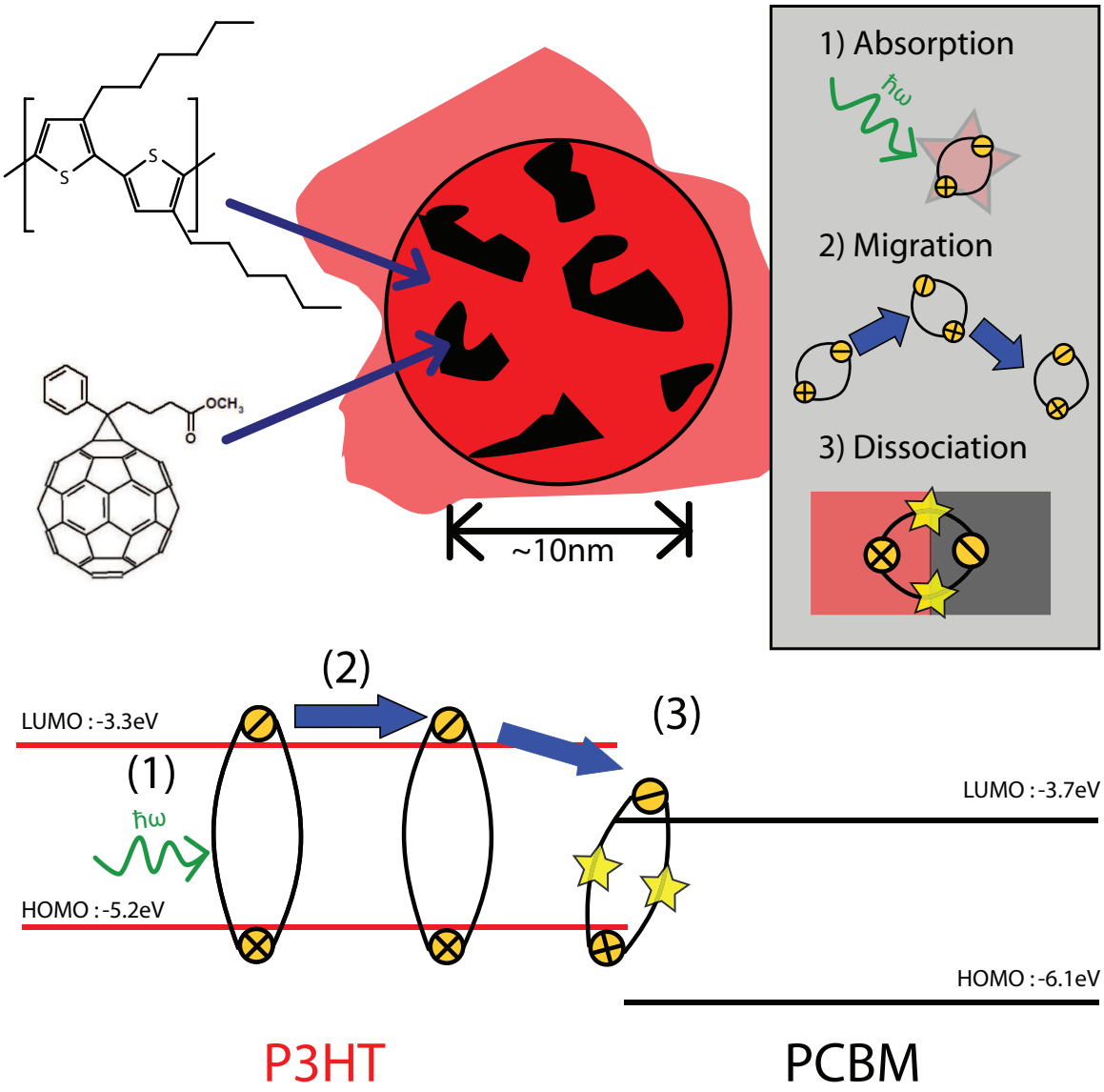

Figure 2.11: The proposed mechanism of operation for bulk heterojunction assisted exciton dissociation. Two of the most common materials are shown on the left: the polymer and hole transporter P3HT, and the electron acceptor PCBM. The primary stages in charge generation are schematically depicted on the right. Below, a band-level diagram shows the energetic landscape within which heterojunction dissociation may occur. The HOMO and LUMO levels given are taken from Reference [44].

CT states in several other polymer blends, with the sole requirement being a suitable energy level offset with respect to PCBM (Figure 2.12) [88]. In Chapter 6, further experimental evidence for such a sub-gap state will be presented.

The primary advantage of this system in terms of exciton dissociation is that it is scalable to any given thickness. However for an efficient solar cell, a continuous and high-mobility percolation pathway from the interface to the contacts is also required for both electrons and holes. As of 2007, the highest efficiency polymer BHJ solar cells are capable of 6% efficiency using a single polymer-fullerene blend [89]. In the case of very thick BHJ films, photovoltaic device performance is no longer limited by photon absorption or exciton dissociation, but by charge separation and transport to the contacts. After the exciton has dissociated, it is known that the electron and hole will follow independent paths through the two interpenetrating materials. To give the most direct percolation path to each contact and ideal morphology for separation, blend ratios of up to 50% have been used [52, 90]. This high ratio is primarily required due to phase segregation in the deposited composite, and a great deal of research has concentrated on optimising the processing conditions to maximise the photon absorption, exciton dissociation, and charge extraction [87, 91, 92]. In this thesis, we report on the most common BHJ composite for solution processable photovoltaics – regioregular poly(3-hexylthiophene) (P3HT) with [6,6]-phenyl-C_{61} butyric acid methyl ester (PCBM) – and will therefore concentrate upon these in the remainder of this section and in Chapter 6.

2.4 Polaron dynamics

The dynamical motion of polarons differs substantially from that of excitons, due primarily to the non-zero electronic charge. This eliminates both the photon mediated transfer and the Förster mechanism as described for excitons. In bulk, room-

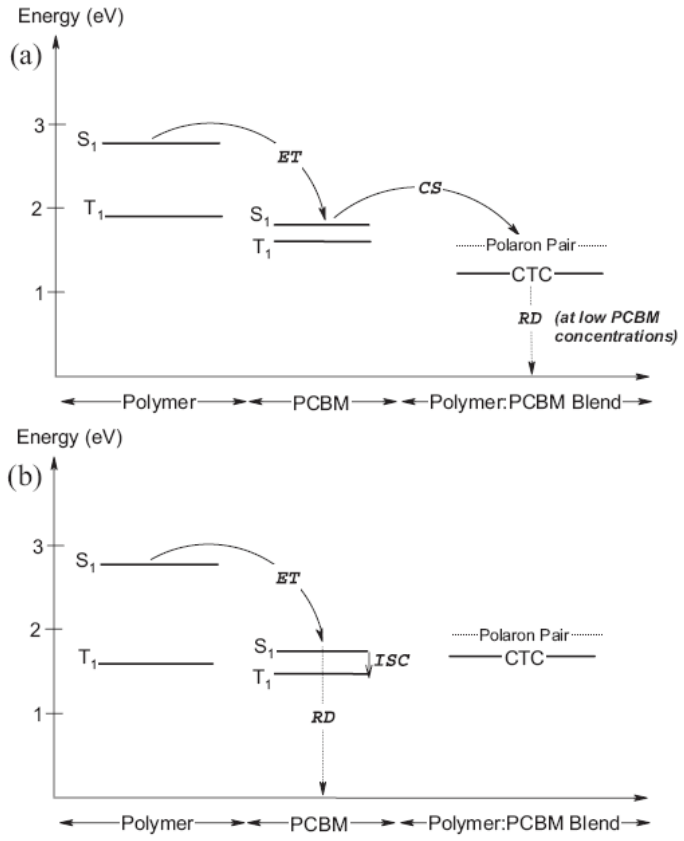

Figure 2.12: Schematic of the energy levels in a polymer-fullerene blend. a) With a suitable energy level offset, energy transfer (ET) occurs to the PCBM, before rapidly charge separating (CS) into an energetically favourable charge-transfer complex (CTC) state. b) Where charge separation is not energetically favoured, radiative decay (RD) is promoted. Taken from Reference [88].

temperature inorganic semiconductors, carrier motion can be seen as a delocalised plane wave with a large mean free path between interactions (known as 'band transport'), whereas in disordered materials with high levels of traps and defects, a model based upon thermally-activated or variable-range hopping is appropriate (known in the organic semiconductor field as 'molecular transport') [4, 36]. Grozema and Siebbeles have recently published a review on the mechanisms of charge transport in organic materials documenting a wide range of processes and resultant mobilities [93]. The carrier mobility μ (which may be a function of frequency, time after charge creation, temperature, shape of the density of states, etc.) is our primary macroscopic handle on the microscopic origin of charge dynamics. The carrier drift velocity v_d (the net movement, in addition to the random walk of carriers) may be defined using the relationship with current density j, by

$$j(t) = eNv_d(t) \tag{2.15}$$

where N is the carrier density. The carrier mobility under an applied electric field $E(t) = E_0 \cos(\omega t)$ may now be defined using the working of Grozema *et al.* in Reference [93][7], where

$$v_d(t) = \mu_1 E_0 \cos(\omega t) + \mu_2 E_0 \sin(\omega t). \tag{2.16}$$

In Equation 2.16, μ_1 and μ_2 represent the real (in-phase) and imaginary (out-of-phase) components of the carrier mobility. The microscopic origin of charge transport may now be addressed for the two cases – DC (where $\omega = 0$), leaving an entirely real, 'resistive' response, and AC (where $\omega > 0$), for which both 'resistive' and 'inductive' response is possible.

[7] This equation holds only in the local limit that the polaron extent is less than the wavelength of the incident electromagnetic field, allowing the wavevector k to be set to zero.

2.4.1 DC mobility

For a significant sub-set of organic semiconductors devices (i.e. photovoltaics, light-emitting diodes and switch-type field-effect transistors), the mobility under DC fields is of primary importance. For single-crystal conjugated molecules, band-like transport with trapping has been observed due to high levels of ordering and purity [36, 94]. In the case of rubrene, a DC mobility as high as $15\,\mathrm{cm}^2/\mathrm{Vs}$ has been observed [95]. However, for most polymeric semiconductors significantly lower mobilities are seen. A notable example is that of P3HT, which has a particularly high charge carrier mobility; values ranging from $10^{-5}\,\mathrm{cm}^2/\mathrm{Vs}$ [96] to $0.1\,\mathrm{cm}^2/\mathrm{Vs}$ [78, 97] have been reported. Sirringhaus *et al.* attributed such a large variation in mobility to the strong dependence on intermolecular ordering; in effect, the progression from variable-range hopping transport in disordered materials to a delocalised polaron (band-like) transport at high levels of local order. This explanation was corroborated by Kline *et al.*, who reported a 4 order of magnitude increase in mobility dependent upon increasing chain length [98], which was attributed to the effect of chain length upon chain packing and local structure.

The microscopic origin of this mobility is hinted at by this dependence upon local packing and regioregularity [78, 100]. However, the details of whether polarons hop primarily along the plane of the semiconductor chain [101] or perpendicular to a molecular plane (along the π-stacking direction [102]) appears to depend strongly upon the material in question. DC measurements are often inappropriate for measuring the intrinsic on-chain mobility of polymers, as the complications of electrical contacts and the inevitable mixing of intramolecular and intermolecular transport make the analysis of the microscopic behaviour difficult to perform. However, there is still interesting physics that may be accessed by performing bulk mobility measurements. In particular, the mechanism of transport has been extensively studied; where hopping-type transport is commonly observed, dispersive transport is often

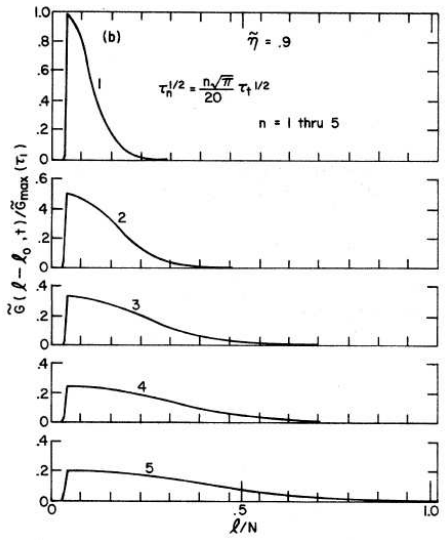

Figure 2.13: Schematic of dispersive energy transport. The charge density of an initially Gaussian-shaped packet is shown as a a function of time (top to bottom). Taken from Reference [99].

indicated [99, 103]. Dispersive transport is characterised by the lack of a 'mean' transport time – the time-dependent distribution of charges for an initially Gaussian shaped packet of charge traversing a polymer slab is shown in Figure 2.13, indicating the absence of a characteristic transport time.

A simple model that is often used to describe thermally activated polaron hopping is known as Miller-Abrahams type dynamics [104]. In this, the rate of energy transfer from site i to site j is related to the difference in energy between the states,

$$W_{ij} = W_0 f(r_{ij}) \begin{cases} 1, \, E_i > E_j \\ \exp\left(\dfrac{-\Delta E_{ij}}{kT}\right), \, E_i \ll E_j \end{cases} \tag{2.17}$$

where E_i, E_j, and ΔE_{ij} are the energy levels of the initial and final states, and the energy difference between the states, respectively. The term $f(r_{ij})$ is a function dependent upon the spatial separation of the initial and final sites, where the exact form is related to the mechanism of hopping. Following the model of Scheidler *et al.*

for phonon-assisted tunnelling, this function may be written analytically as [105]

$$f_{\mathrm{PAT}}(r_{ij}) = \exp\left(\frac{-2r_{ij}}{\alpha}\right), \tag{2.18}$$

where α is the localisation length. Alternative formulations are available; the review in Reference [93] describes some of the possible processes.

2.4.2 AC mobility

The AC mobility of a polymer is of particular interest for high-speed switching applications, but also because it can provide a handle on the intrinsic on-chain carrier mobility of a polymer [106]. Conceptually, at high frequencies carrier move less distance in each cycle, and an increasingly local probe of mobility is obtained with increasing frequency. This has been used as an explanation for the almost universally observed increasing mobility with frequency, and has permitted the extrapolation of carrier mobilities as high as $600\,\mathrm{cm}^2/\mathrm{Vs}$ for an isolated 'infinitely long' chain of PPP [106]. This is confirmed to some extent by conductivity measurements on CdSe nanoparticles, where there is a qualitative change in the mobility between the strong-confinement (particle is smaller than probe effective wavelength) and weak-confinement regime (particle is larger than probe effective wavelength) [107]. However, the precise effect of this confinement in organic semiconductors, and the frequency-dependent mobility that results is still an open question.

Measurements of the AC mobility in polymeric semiconductors are typically in the range of $10^{-2} - 10^{2}\,\mathrm{cm}^2/\mathrm{Vs}$, as determined by transient microwave conductivity ($\nu \sim 30 \times 10^{9}\,\mathrm{Hz}$)[79, 108–111] or terahertz conductivity ($\nu \sim 1 \times 10^{12}\,\mathrm{Hz}$)[112–114] measurements. Terahertz frequency measurements will be primarily addressed in this thesis. As shown in Figure 2.14, a typical terahertz-frequency conductivity signature of a photoexcited organic semiconductor is a monotonically increasing

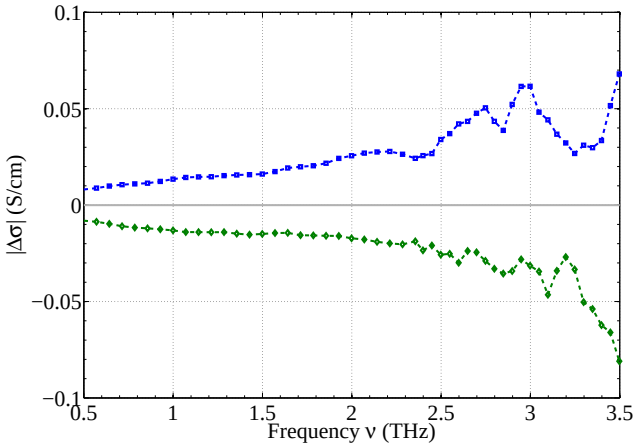

Figure 2.14: A typical terahertz frequency conductivity spectrum is shown for P3HT excited at 560 nm; the real part is shown with blue squares and line, and the imaginary component is green diamonds and line. Note that this is the photoconductivity of the excited particles only, and does not include a contribution from the equilibrium conductivity of the polymer.

real and decreasing imaginary component. Němec *et al.* assign this to the sum of a frequency-independent free carrier term, together with a frequency-dependent Debye relaxation term [115]. Grozema *et al.* presented a model based upon torsional disorder that reveals an increasing mobility with frequency, up into the terahertz regime [116]. Hendry *et al.* use a more qualitative model, suggesting that free carriers would be expected to contribute to both the real and imaginary components, whilst excitons have a terahertz-frequency polarisation response, modelled by the Clausius-Mosotti equation, and provide an imaginary component only [117]. Further discussion of conductivity modelling is given in Section 3.3.4.

2.4.3 Polaron trapping

Polaron trapping is of significant interest to device scientists, and a firm knowledge of the charge trapping mechanisms is required for optimisation of organic field effect transistor performance [6]. Organic transistors are known to degrade over a relatively short time period, which has been attributed to carrier trapping [118–121]. The

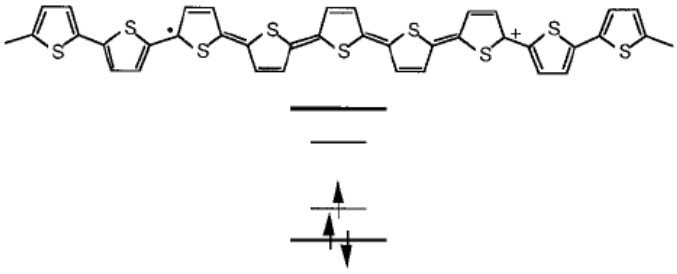

Figure 2.15: A schematic depicting the physical and energetic effect of a polaron on a polymer backbone, represented by a black circle in the upper diagram. By placing a polaron on the chain, the surrounding bonds change nature, leading to a geometrical relaxation and 'pulling' of the polaron energy level into the band-gap. Taken from Reference [6].

trapped charges may reduce the density of states. Three types of trapping will be addressed here:

Self-trapping. Due to the strong interaction between the charge and the polymer-backbone, polarons have a tendency to self-trap as shown in Figure 2.15. This means that the polymer backbone will reorganise around the charge in such a way as to minimise the energy of the system – in turn this reduces the number of lower-energy states available (through Miller-Abrahams type transfer), and reduces the mobility of the charge. To determine whether it is energetically favourable for a charge to self-localise, the energy cost of localising the wavepacket (arising from the uncertainty principle) must be weighed against the energy gain from local lattice polarisation [36].

Shallow traps. When OFET devices are operated, the reduction in device current can be attributed to two, seemingly separate effects. Shallow traps (also known as reversible traps) represent the class of traps with a small trapping energy. In this case, carriers tend to be thermally de-trapped at room temperature in a short period of time. These traps may be related to self-trapping, particularly in portions of the bulk polymer in which self-trapping is favourable [120].

Deep traps. Deep, or irreversible traps are those with a large binding energy, suggested by Salleo *et al.* to arise from disordered areas of polymer film. In order to de-trap carriers in these states, Salleo and co-workers suggested using above-band-gap radiation [120]. However more recent studies have shown that de-trapping is unlikely in this case, as the illumination simply injects 'fresh' charges due to dissociation of the photoexcited excitons [118].

In addition, trapping at interfaces, extrinsic chemical impurities [121] or through bipolarons [120] is known to occur under suitable conditions. In this thesis, there is little evidence for polaron trapping over the 1 ns timescales available. Reference [121] provides a good review of polaron trapping in state of the art OFETs.

2.5 Inorganic Semiconductors

Until this point, the electronic processes in organic semiconductors have been exclusively addressed. However, another larger class of semiconductors is inorganic in nature. A key inorganic semiconducting material is Gallium Arsenide, and the electronic dynamics in nanowires of this material are investigated in Chapter 5. Inorganic semiconductors have been experimentally and theoretically studied for over fifty years; many textbooks contain good introductions to this field such as Smith [122], Kittel [39] and Singleton [4]. These references provide a theoretical background applicable to bulk semiconducting materials.

The number of applications of nanostructured inorganic semiconductors is rapidly growing, particularly in the field of optoelectronics and nano-electronics. Quantum confinement occurs on the nanometre scale, and the behaviour of quantum objects such as zero-dimensional quantum dots, or two-dimensional quantum wells are well studied. However, non-quantum confined (or intermediate regime) nanostructured materials are less well investigated, and are becoming increasingly important as the

length scales involved in semiconductor devices reach the nanometre scale. Recently non-quantum confined nanowires have been used for field-effect transistors [123], lasers [124], single-photon sensors [125] and in dye-sensitised solar cells [126]. A good review of synthesis, microscopy and material characteristics of nanowires is given in Reference [127]. The large surface-area to volume ratio leads to many novel effects, both useful and unwanted. In this section, some of the theoretical areas specific to nanostructured inorganic semiconducting materials are presented, and the differences between inorganic and organic semiconductor electronic structure and dynamics are highlighted.

2.5.1 Band transport

As described in Section 2.4, charge transport in disordered organic semiconductors is typically described using a hopping or molecular model. In contrast, carrier transport in inorganic semiconductors (and some crystalline molecular semiconductors) is best described using band transport. In this case, a charge in the (idealised) material in a conduction-band state moves with a constant velocity under an applied electric field. The velocity and hence mobility can then be described simply using

$$m^* \frac{\mathrm{d}\mathbf{v}}{\mathrm{dt}} = -e\varepsilon, \tag{2.19}$$

where ε is the applied electric field, $\mathbf{v}$ is the charge velocity, and m^* is the effective mass [39, 122]. A schematic showing the difference between hopping transport and band transport is shown in Figure 2.16. From this description, it is clear that non-dispersive transport is expected for band transport, differing from the organic semiconductor case. In reality, crystals are not ideal, and charge can scatter (randomising their momentum) as a result of many different processes. In particular, impurity scattering, thermal scattering (electron-phonon), and boundary scattering may occur and

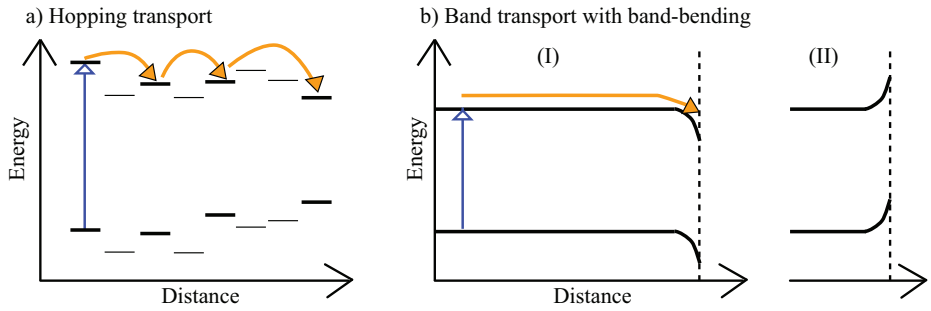

Figure 2.16: Schematic of a) hopping transport and b) band transport under a static electric field (towards positive distance), showing the influence of the energy levels upon the transport mechanism. Also shown for band transport is two possible surface effects, depicting either a (I) positive or (II) negative surface potential.

the bulk conductivity can be readily described using the Drude model [128]. Also the effect of the geometry, size and chemical bonding at the surface of the materials has a significant effect upon the electronic structure and the performance of devices based upon the semiconductor, for instance increased carrier trapping and the appearance of new quasi-particles.

2.5.1.1 Surface traps

The theory of recombination of conduction band charges at bulk traps was developed by Shockley and Read in 1957 [129]. Additionally, non-radiative trapping centres can arise at the surface of inorganic semiconductors due to the atomic arrangement of ions at the surface, in turn depending on the chemical origin of the surface atoms. The relationship between the chemical nature of the surface covalent bonds and the electronic structure is beyond the scope of this thesis; Reference [130] covers some of the issues involved. The impact of surface chemistry upon devices based on inorganic semiconductors can be related to a quantity known as the surface recombination velocity. Following the workings of Reference [122], the flow of carriers towards a surface can be written as $\frac{1}{4}v_t n$ per unit area (where v_t is the average thermal velocity and n is the carrier density per unit area). The flow away from the surface may then

be written as $\frac{1}{4}rv_t n + S$ where r is the probability that the carrier is reflected and S is the rate of emission from the surface into the bulk. At equilibrium, these must be equal, and both values of n are equal to n_0, such that

$$S = \frac{1}{4}(1-r)n_0. \tag{2.20}$$

However, when the system is perturbed from equilibrium (such that $n \neq n_0$) the surface trapping rate is given by

$$S_{\text{trap}} = \frac{1}{4}(1-r)v_t(n-n_0) \tag{2.21}$$

$$S_{\text{trap}} = s\Delta n \tag{2.22}$$

where s has the units of velocity, and is known as the surface recombination velocity. For micro or nanostructured electronics, the surface effects become increasingly important and may even result in the complete quenching of photoluminescence in favour of non-radiative trapping [131]. To reduce the surface recombination velocity a technique known as surface passivation is often used. For instance, Yablonovitch *et al.* [132] reported that a chemical treatment with inorganic sulfides provides a favourable electronic surface for Gallium Arsenide. This technique was shown to strongly extend the carrier lifetime in an inductive transient conductivity experiment, and more recently an increase in lifetime has been observed using terahertz time-domain spectroscopy [133].

2.5.1.2 Surface plasmons

The conduction-band carriers in inorganic semiconductors may be represented by a nearly-free cloud of charges, which may oscillate about their equilibrium positions with a characteristic quantised energy. This interpretation was expounded by Pines and Bohm in 1952 [134], and is known as the plasmon model. In this case, the

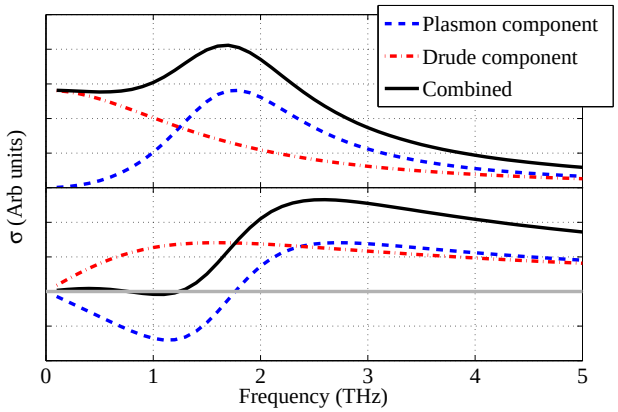

Figure 2.17: The real and imaginary components of a conductivity spectrum are shown for a material with both Drude-like and plasmonic responses (upper and lower frame, respectively). Note that the frequency of the peak response in the plasmonic case can be used to extract directly the carrier density within the material.

harmonic oscillation frequency of the bulk plasma is given by

$$\omega_p = (Ne^2/\epsilon_o m^*)^{1/2}, \tag{2.23}$$

where N is the carrier density and m^* is the carrier effective mass. In 1957, Ritchie proposed a model to explain the occurrence of characteristic plasmonic absorption at energies less than $\hbar\omega_p$, that only appeared for thin metallic films [135]. For the smallest sized metallic objects, this sub-plasmonic absorption cross-section became significant. This absorption was later termed a surface plasmon oscillation; a good review of the field is given by Pitarke [136]. In essence, while plasmons are quantised collective plasma oscillations in the bulk of the material, an interface (or surface) has the effect of reducing the plasmon energy due to the change in dielectric function [39]. One of the most striking points is that coupling into or out of surface plasmon modes is typically forbidden, however it becomes directly accessible to electromagnetic excitation when the material dimensions are significantly smaller than the wavelength corresponding to the surface plasmon frequency. The terahertz-frequency spectrum

for a material with both a Drude-like and plasmonic response is shown in Figure 2.17. This is similar to the case of the Gallium Arsenide nanowires discussed in Chapter 5.

Chapter 3

Experimental Methods

The experimental studies in Chapters 4, 5 and 6 rely on a variety of spectroscopic techniques. These can be broadly divided into steady-state and time-resolved techniques. In this chapter, a brief section will be dedicated to steady-state techniques; however, these are well established methods and often use commercially available tools. A more in-depth explanation will be devoted to the time-resolved techniques of photoluminescence up-conversion spectroscopy (PLUCS) and optical-pump terahertz-probe time-domain spectroscopy (OPTP-TDS). These are optically-gated techniques that rely on non-linear optical effects, and ultrafast laser pulses. While these two time-resolved methods used in this thesis are modern but well-established, the experimental details and data analysis can be challenging and will be fully explained within. Secondly, the important topics of non-linear optics and the pump-probe technique will be covered. The experimental layout and data analysis techniques associated with PLUCS and OPTP-TDS will be described, and finally the analysis and interpretation of the OPTP-TDS experiment will be covered.

3.1 Steady-state techniques

The mainstay of optical spectroscopy of semiconductors is in accurate absorption and luminescence measurements from the near infrared to ultraviolet ($\hbar\nu$ =0.5-5 eV, $\tilde{\nu}$ =4000-40,000 cm^{-1}, $\nu = 120 - 1200 \times 10^{12}$ Hz, λ =2500-250 nm). This energy range contains the band-gap of many commonly used inorganic semiconductors (i.e. bulk Gallium Arsenide with a band-gap of $E_g = 1.424$ eV), and the primary absorption of almost all organic semiconductors. For example, the most commonly used polymeric organic semiconductors all have absorption peaks in the visible wavelengths: F8 at E_g=3.17 eV, F8BT at E_g=2.75 eV, and MDMO-PPV at E_g=2.43 eV (all data taken from *American Dye Source*). As discussed in Section 2.2.1, the peak absorption and emission wavelengths in polymeric semiconductors are typically separated in energy by the Stokes shift, related to the confirmation relaxation of the polymer chain after photoexcitation, and simple steady-state measurements remain a powerful spectroscopic technique [61].

All of the steady-state absorption data presented in this thesis were measured using a *Perkin-Elmer* Lambda 9 UV/VIS/NIR spectrophotometer. This is a dual beam instrument, capable of detection of optical densities as high as 6. When using thin film samples, it is important to use an appropriate aperture in both the reference and sample beams to avoid artifacts that arise from spatial beam 'wander'. As the beam size and our typical sample size are similar, the 'wander' can be a significant source of error, which can directly lead on to error in the quantum efficiency of emission or charge carrier generation.

The steady-state emission spectra were measured using the same experimental arrangement as the photoluminescence up-conversion, and will be described in the next section. Using our experimental setup, a typical absorption and emission spectrum is shown in Figure 3.1.

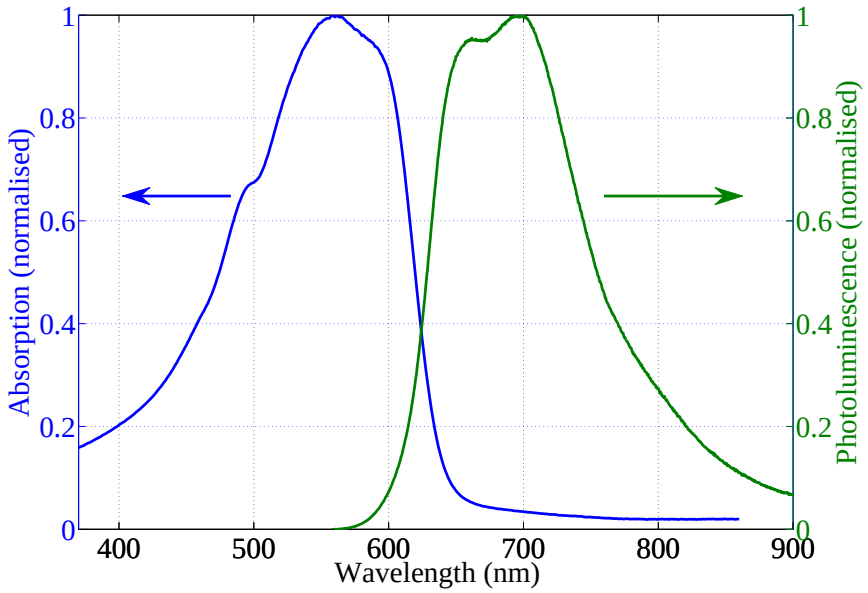

Figure 3.1: A typical, normalised steady-state absorption and photoluminescence curve (blue and green lines, respectively). The sample was P3HT embedded in a ultra-high molecular weight polyethylene matrix, and the photoluminescence curve was measured after excitation at 450 nm. The figure shows the high signal to noise ratio obtainable using steady-state experiments, with relative ease.

3.2 Time-resolved spectroscopy

The field of time-resolved spectroscopy covers any spectroscopic measurement that is made as a function of time after a perturbation to the equilibrium state of a system, typically by exciting the system with a short optical pulse (although electric excitation and systems based upon pulsed electron sources may also be used). Common electronic techniques include time-correlated single photon counting (TCSPC) and time-resolved microwave conductivity [109, 137]. In these, high speed electronics are used to measure the sample photoluminescence or conductivity as a function of time, respectively. These techniques have the advantage of using electronic delay techniques to provide time resolution, which are easy to implement. However, the fundamental limit for resolution is set by the speed of the electronics within the detection device, and the ultimate resolution is set by the clock rate of the data acqui-

sition circuit. Currently, typical transistor switching times lie in the tens to hundreds of nanoseconds regime [138], whilst specialist high-speed transistors have switching times reaching down into the hundreds of picoseconds regime [139]. This means that the ultimate resolution of electronic devices is limited to orders of magnitude longer than the femtoseconds to tens of picosecond range which are characteristic of energy dynamics in organic semiconductors[1]. To overcome this limitation, it is necessary to move from *electronically-gated* measurements to *optically-gated* techniques.

3.2.1 Optical pump-probe spectroscopy

Pump-probe spectroscopy is a class of time-resolved experiments that encompasses both PLUCS and OPTP-TDS, where both the excitation and the detection of spectroscopic properties are performed using synchronous short laser pulses, and the evolution of the system can be mapped out by changing the optical delay between these two events. This technique allows us to reach timescales limited by a) the duration of the laser pulse, b) the accuracy of the optical delay line and c) the nature of the non-linear interactions used to measure the properties, as described below. In practise, while the pulse duration sets an ultimate minimum temporal resolution of an experiment, it is the finite thickness of non-linear crystal with the associated phase-matching and dispersion effects that leads to coarsening of the temporal resolution. The method of creating the ultrashort laser pulses is described in the next section.

3.2.2 Ultrashort amplified laser pulses

The generation of ultrashort (sub-picosecond, $< 10^{-12}$ seconds) laser pulses has opened up the field of ultrafast physics. Typically the technique of mode-locking is used, and the advent of commercially available all solid-state lasers producing pulses as short as

[1] Certain specialist electronic devices such as streak cameras, or multi-channel plates also have a time resolution in the one picosecond regime.

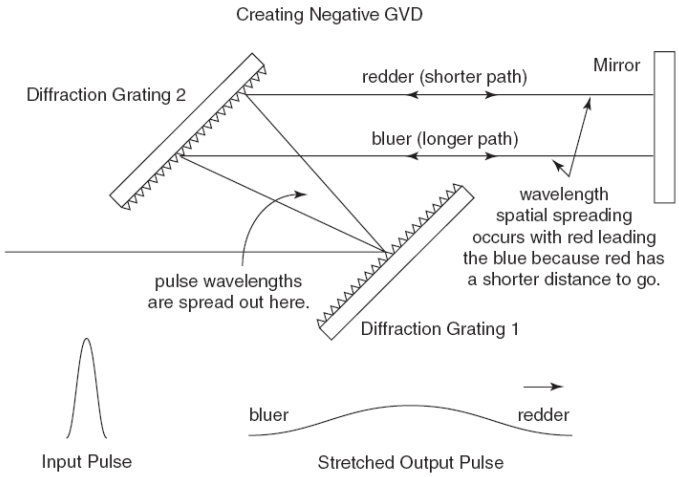

Figure 3.2: The experimental configuration of the pulse stretcher used in the Spitfire CPA regenerative amplifier. The incident 'seed' pulse is temporally stretched by the application of a linear chirp, with the shorter wavelength (bluer) section of the pulse being delayed with respect to the longer wavelength (redder) section. This is achieved with a pair of reflective diffraction gratings. Taken from Reference [142].

6 fs have led to their becoming a common sight in modern physics laboratories [140]. To take advantage of non-linear effects, both a high pulse energy and an ultrashort pulse duration are required, to reach the peak electric fields necessary. The primary limitation in the production of these pulses is that non-linear effects in a laser gain medium must be avoided, as self-focusing can lead to intensities above the damage threshold of the gain medium. To this end, chirp-pulse amplification (CPA) regenerative amplifiers are becoming increasingly used; a good description of this technique is given in Reference [141], however, a basic outline will be given here.

The amount of energy that may be extracted from a laser material is limited by non-linear effects and the damage threshold of the material. These problems increase with increasing pulse energy, or decreasing pulse duration, but may be avoided by using CPA. The optical layout of a typical CPA amplifier is shown in Figure 3.3. The basic technique is straightforward: an ultrafast pulse (< 1 ps) from a laser oscillator is taken, and a linear chirp is applied using a grating based stretcher. Figure 3.2 shows the experimental arrangement for the stretcher; the compressor is similar but reversed.

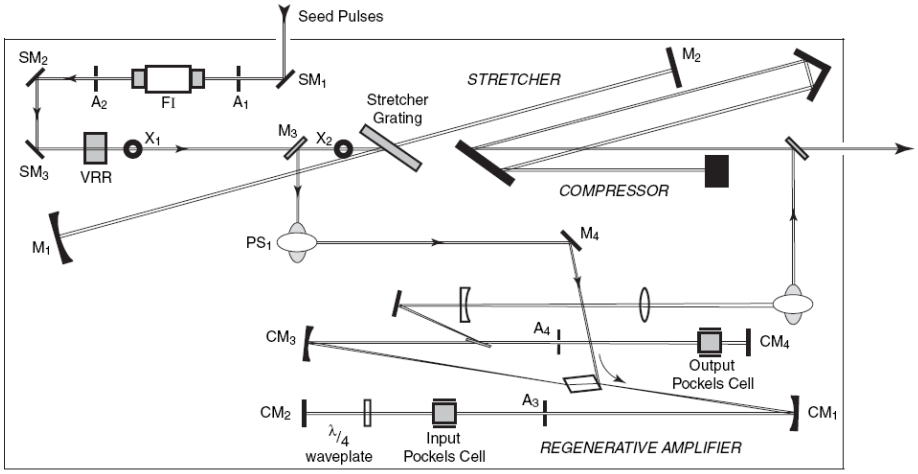

Figure 3.3: The layout of the Spitfire CPA regenerative amplifier. The 'seed' pulse is prepared in the upper part of the figure by temporal stretching and setting of the polarisation state. Secondly, the pulse is amplified in the lower section (labelled *REGENERATIVE AMPLIFIER*). The Pockels cells used to select an input pulse and to control the number of pulse round-trips before coupling the pulse out are shown. Finally, the compressor is shown just prior to the beam output, at the top right. Taken from Reference [142].

Typically, the stretched pulse may be extended up to a nanosecond in duration. This 'seed' pulse is then amplified using a regenerative amplification technique. In this, the gain medium is initially pumped using a high-energy ($\sim 7\,\mathrm{mJ}$) nanosecond Q-switched pulse before the seed is coupled into the amplifier cavity via a Pockels cell and a thin-film polariser. After a set number of round-trips of the cavity (typically $\sim$7), the pulse has built to a maximum in power and the population inversion in the gain medium is exhausted, and the amplified pulse can be coupled out of the cavity using a second Pockels cell. The compressor is then used to re-compress the pulse to its Fourier transform limit. The method significantly reduces the peak power of the pulse during amplification, so any non-linear interaction within the gain medium is avoided. The spectrum of the seed pulse and the resultant amplified pulse are shown in Figure 3.4, revealing a reduction in bandwidth upon amplification. This in turn marginally increases the pulse duration, and arises due to the amplification process.

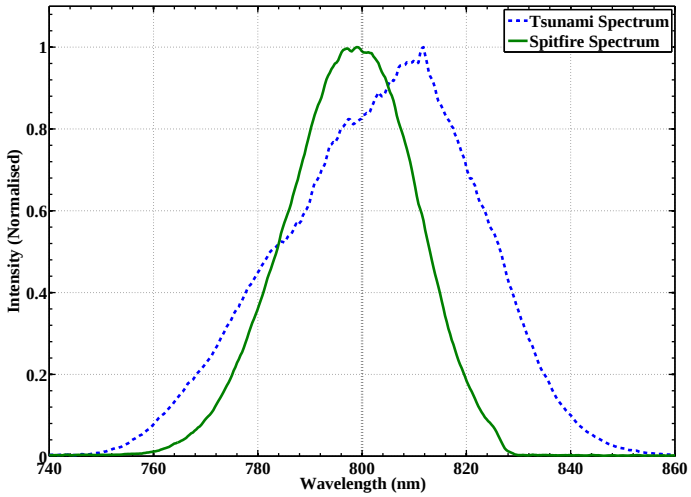

Figure 3.4: The normalised spectrum of laser emission from the Tsunami Ti:Sapphire oscillator and the Spitfire CPA regenerative amplifier are shown (blue dashed line and green solid line, respectively). The broad bandwidth of the 'seed' pulse and the spectral narrowing caused by the amplification processes can be seen.

3.2.3 Non-linear optics

Both the up-conversion technique and terahertz time-domain spectroscopy rely on second-order non-linear processes exhibited by certain crystalline materials. Non-linear optics is of particular importance for high power laser pulses, as we enter a regime in which the polarisation $\mathbf{P}$ of a crystalline material no longer varies linearly with the applied electric field, $\mathbf{E}$ [13]. In linear optics, we can write

$$\mathbf{P} = \epsilon_0 \chi \mathbf{E}, \tag{3.1}$$

where χ is the electric susceptibility. If we treat only the case where the polarisation is parallel with the electric field ($\mathbf{P} = P_x, \mathbf{E} = E_x$), we can now consider higher order terms in P such that

$$P_{\text{nonlinear}} = P_1 + P_2 + P_3 ... = \epsilon_0 \left(\chi_1 E_x + \chi_2 E_x^2 + \chi_3 E_x^3 ... \right), \tag{3.2}$$

where E is the magnitude of the electric field. The different order susceptibilities give rise to the full range of non-linear effects. The most important term for the effects used in PLUCS and OPTP-TDS is the second order non-linear susceptibility, which leads to phenomenon such as frequency mixing (and frequency doubling), optical rectification and the Pockels effect. This non-linear effect does not occur in all materials – in fact, the second order non-linear effect is only observed in non-centrosymmetric media, since inversion symmetry would imply that the polarisation P would be unchanged following an inversion transformation, and therefore $\chi_2 = 0$. In addition, the second order effect is often very small and for these reasons much care must be taken to choose a suitable crystal for a particular task. For arbitrary wavelength generation, an optical parametric amplifier is used – this relies on both the second-order and *third-order* non-linear coefficient. Good materials for third-order non-linearities are centrosymmetric (hence $\chi_2 = 0$, meaning the third-order non-linearities dominate), and must have a high damage threshold – sapphire and water are often used [143]. Reference [144] has a good general review of applied non-linear optics for ultrafast pulses; only a brief outline of the basic principles will be given here.

Considering just the second order effects (and using the simplifying assumption that the tensor χ may be expressed as a scalar χ_2 in this case), if two plane waves of the form $E_i(t) = E_0^{(i)} \cos(\omega_i t)$ are incident upon a medium, then the nonlinear polarisation will be

$$P_2(t) = \epsilon_0 \chi_2 \left(E_1 \times E_2\right) \tag{3.3}$$

$$P_2(t) = \epsilon_0 \chi_2 \left(\frac{1}{2} E_0^{(1)} E_0^{(2)} \left[\cos\left((\omega_1 + \omega_2)t\right) + cos\left((\omega_1 - \omega_2)t\right)\right]\right). \tag{3.4}$$

Equation 3.4 shows that the second-order non-linearity forms two waves with frequencies $\omega_s = \omega_1 + \omega_2$ and $\omega_d = \omega_1 - \omega_2$, where the subscripts s and d represent sum-frequency and difference-frequency generation, respectively. The resultant re-

emitted electric field is given by the second derivative of the polarisation with respect to time, and for the simple *cosine* case given here, is of the same form as Equation 3.4. The frequency of the re-emitted radiation follow from the requirement of conservation of energy. A second requirement is conservation of photon momentum, $\mathbf{k_s} = \mathbf{k_1} + \mathbf{k_2}$. This is somewhat more difficult to achieve, as the photon momentum is dependant upon the refractive index of the non-linear medium, which may be a vary as a result of optical frequency, polarisation or spatial direction of propagation: in general, $\mathbf{k_i} = \omega_i n(\omega)\widehat{u}_i$, (where $\widehat{u}_i$ represents a unit vector in the direction of propagation). Using this, we may state what is known as the "phase-matching condition", which is equivalent to a requirement upon the refractive indices of the material for each wave frequency and polarisation. Conceptually, we may imagine the non-linear process occurring at each point throughout the crystal along the z-axis – if the speed of the fundamental pulse and the non-linear polarisation induced pulse are not equal, at a point $z + \Delta z$ the new generated non-linear product will soon be out of phase with that generated at z, and will interferometrically cancel. If the speeds are equal, an efficient non-linear process is possible. Each non-linear phenomenon utilised in this thesis can now be studied; those for the PLUCS experiment are presented here.

Second-harmonic generation. As shown in Figure 3.1, organic semiconductors have wide but well defined absorption bands, typically in the visible or near-ultraviolet spectrum. For the production of useful excitation wavelengths from the Ti:Sapphire laser fundamental (770 nm-950 nm), second harmonic generation must be used. In this case, the two wavelengths shown in Equation 3.4 are equal and the directions of propagation are co-linear : $\omega_1 = \omega_2$, $\omega_s = 2\omega_1$ and $\widehat{u}_s = \widehat{u}_1 + \widehat{u}_2$. In order to achieve phase-matching throughout the crystal, it is necessary to orient the crystal so that the fundamental wave is polarised perpendicular to the crystal optic axis such that it propagates with a constant refractive index n_o, whilst the second-harmonic waves

are have polarisation components both parallel and perpendicular to the optic axis, and have a refractive index $n(\theta)$ that varies with the angle between optic axis and propagation direction (such that $n_o \leq n(\theta) \leq n_e$). Following this scheme, a direction may be found where phase matching is satisfied (i.e. $n_o(\omega) = n(2\omega, \theta)$).

Sum-frequency generation. In the up-conversion process, photons from the sample photoluminescence are 'added' (mixed) to those from the gate pulse : $\omega_1 = \omega_{\text{laser}}$, $\omega_2 = \omega_{\text{pl}}$, and $\omega_s = \omega_{\text{laser}} + \omega_{\text{pl}}$, which typically lies in the ultraviolet spectral region. Only photoluminescence photons that are temporally overlapped with the gate pulse inside the non-linear material undergo this processes, providing an all-optical method of temporal selection, known as *gating*. In addition, Equation 3.4 shows that the intensity of the up-converted light (typically on the order of hundreds of photons per second) is proportional to $E_0^{(\text{pl})}(t)$ and $E_0^{(\text{laser})}$ where t is the delay between the gate pulse and the start of the photoluminescence; as the laser intensity is fixed, the signal is then simply proportional to the photoluminescence as a function of time. The phase matching conditions mean that only a small wavelength range of photoluminescence photons are able to interact at a given crystal angle, providing a mechanism to be spectrally selective. The crystal most often used for the two photon-addition techniques is β-BaB_2O_2 – also known as BBO – due to its large value of $\chi_2 = 1.78\,\text{pmV}^{-1}$, and small absorbance down to 200 nm [145].

In these procedures, the thickness of the crystal plays an important part – the thicker the crystal, the larger the conversion efficiency, however, temporal broadening due to dispersion and tightening requirement on phase-matching condition mean a compromise must be struck, and crystals of between 0.1 mm and 2 mm are typically used.

3.3 Experimental details

In this section, the experimental setups used will be described in detail. In this thesis, three time-resolved experiments were carried out : photoluminescence up-conversion known as "PLUCS" (used in Chapters 4), amplified optical-pump terahertz-probe spectroscopy known as "Amplifier OPTP-TDS" (used in Chapters 5 and 6), and low fluence oscillator based optical-pump terahertz-probe spectroscopy, known as "Oscillator OPTP-TDS" (used in Chapter 6).

3.3.1 Photoluminescence up-conversion

Photoluminescence up-conversion spectroscopy is the name given to the class of optical spectroscopy techniques, for which the photoluminescence lifetime is measured using optical gating in a non-linear crystal. The basic principle relies on a single laser pulse being split into two; the first is used to excite the sample, and the second is used to gate the resultant photoluminescence. An optical delay line between these two pulses provides the time resolution, and the combination of the phase-matching conditions in the crystal and a spectrometer provide spectral discrimination. The large initial laser pulse energy coupled with the extremely small up-converted photon number mean care must be taken to filter out the laser and fundamental photoluminescence, to provide a reasonable signal to noise ratio. Figure 3.5 shows the "PLUCS" system. A *Spectra-Physics* Millenia VIs frequency-doubled Nd:YAG laser is used to pump a Tsunami Ti:Sapphire laser with 4 W of light at 532 nm. The Tsunami oscillator provides pulses of $\sim$ 75 fs duration, with a tunable centre wavelength in the range 695 nm-1060 nm and with approximately 11 nJ of energy per pulse (at 800 nm). The pulse initially passes through a periscope to set a correct beam height of 6" (152.4 mm). A combination of a half-wave plate (HWP1) and a polarising cube beam splitter (BS1) allows the output power to be divided between

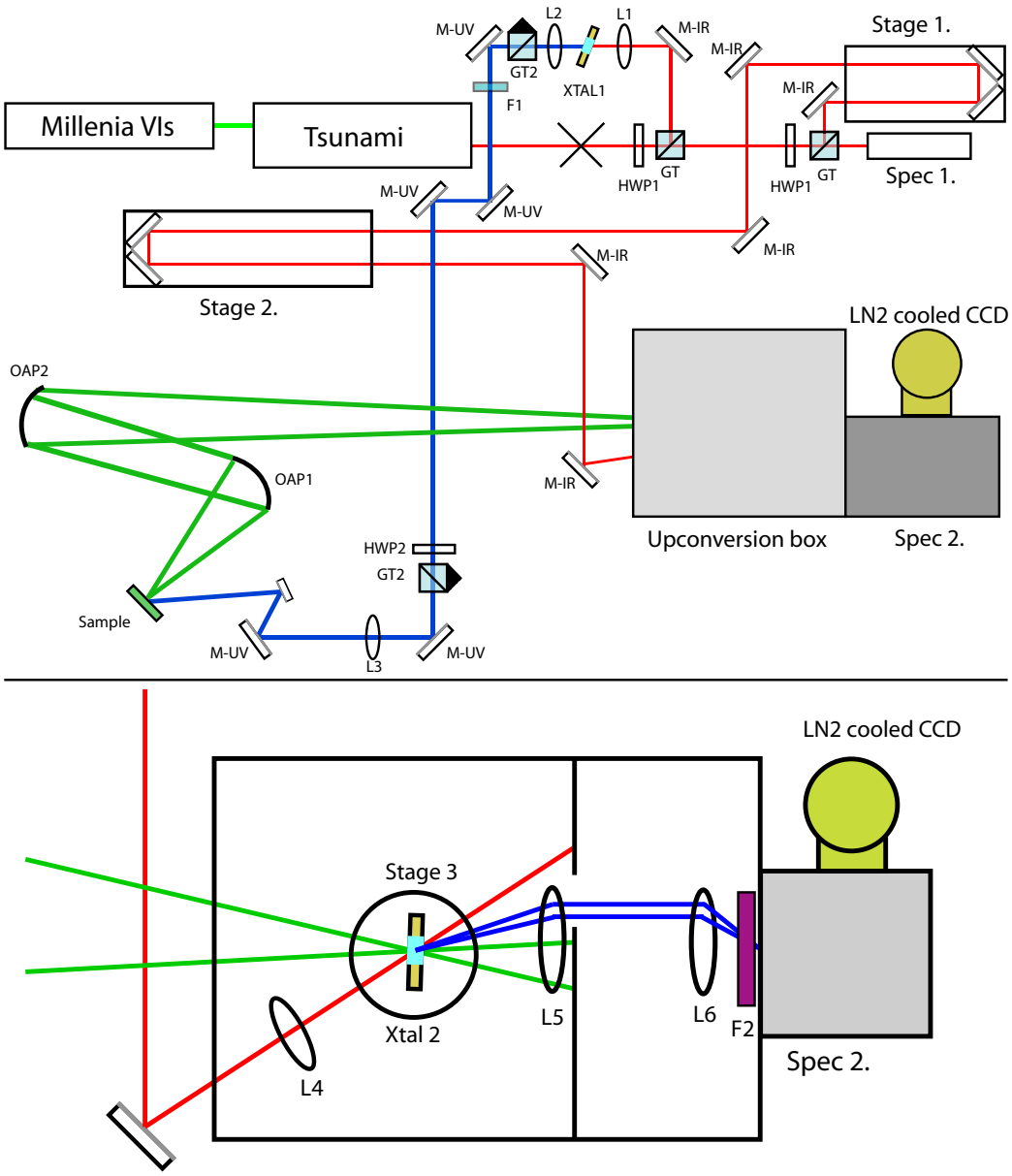

Figure 3.5: The experimental set-up for time-resolved and steady-state photoluminescence spectroscopy – the 'PLUCS' system – is shown. The upper panel depicts the optical paths on the bench, while the lower panel is a close-up view of the up-conversion crystal box. The purpose of the components is given in the text.

Part	Description
Millenia VIs	Spectra-Physics, Frequency-doubled Nd:YAG 4 W
Tsunami	Spectra-Physics Ti:Sapphire laser oscillator Pulse duration : 75 fs Centre wavelength : 695 nm-1060 nm Typical pulse energy : 11 nJ/pulse Repetition rate: 80 MHz
M-IR	Vis-IR mirrors, Thor Labs part 5103
M-UV	Vis-UV mirrors, Thor Labs part 5108
HWP1	Newport polymeric half-wave plate (IR)
HWP2	Newport polymeric half-wave plate (UV)
BS1, BS2	Cube beam-splitter
GT1	B-Halle Glan Thompson polarising prism and beam dump
Stage 2	Newport ICS200PP 200 mm stage
Stage 3	Newport UE4 1PP rotation stage
Motion Controller (not shown)	Newport ESP300
L1	Uncoated Comar lens 50DQ16
L2	Uncoated Comar lens 40PS25
L3	Comar lens 250PU25
L4	Comar lens 125DQ25
L5,L6	Comar lens 100PU50
F1	Schott filter: blue-pass BG39
F2	Schott filter: UV-pass UG1 or UG11
OAP1	Off-axis parabolic mirror, 30° off-axis
OAP2	Off-axis parabolic mirror, 30° off-axis
Xtal1	0.5 mm × 5 mm × 5 mm BBO $\phi = 35°$ $\theta = 0°$
Xtal2	0.3 mm × 5 mm × 5 mm BBO $\phi = 35°$ $\theta = 0°$
Spec1	Ocean Optics USB2000
Spec2	Jobin Yvon TRIAX 190 Triple-axis Gratings : 1) 1200 lines/mm 2) 300 lines/mm)
CCD	Jobin Yvon Symphony 1024x256-OPEN-3LS CCD
Vacuum Pump (not shown)	Pfeiffer TSH071

Table 3.1: Parts list for the PLUCS system.

two paths, known as the 'excitation' path and the 'gate' path. Following the gate path, the beam passes through another half-wave plate (HWP1) and polarising cube beamsplitter (BS2) combination, to rotate the pulse polarisation back to its original state. A small amount of light passes straight through the cube, which is fed into an *Ocean Optics* USB2000 mini-spectrometer which can be used as a laser diagnostic. The majority of the beam traverses a fixed delay stage 1, and down to a computer controlled variable delay stage 2 (Newport ICS200PP with 200 mm of travel=1.3 ns of delay). From here, it is directed into the up-conversion box.

The second pulse (excitation pulse) is focused through lens L1 onto a second-harmonic generating BBO crystal Xtal1, mounted in a manual rotation and translation stage for accurate alignment and ease of phase matching. The frequency doubled component is collimated using a second lens (L2), and then directed through a Glan Thompson polarising prism with attached beam dump. As the frequency doubled component is generated with the opposite polarisation with respect to the incident light, this has the effect of removing the fundamental beam. Any remaining fundamental beam is removed by a transmissive filter, F1. The beam is then directed through another half-wave plate (HWP2) and Glan Thompson pair (GT1), which allow the polarisation state and transmitted power of the pulse to be set accurately before being focused via L3 onto the sample. Thin film samples are held inside a purpose built vacuum chamber, which can be evacuated to a pressure of 10^{-7} mbar. The photoluminescence is collected and collimated using an off-axis parabolic mirror (OAP1). Parabolic mirrors are used for two reasons; firstly, using reflective focusing optics as opposed to refractive optics avoids temporal dispersion of the emitted photoluminescence, and secondly parabolic mirrors are used to eliminate all spherical and chromatic aberration. A second parabolic mirror is used to focus the photoluminescence onto the up-conversion crystal inside the box.

The core of the up-conversion system is shown at the bottom of Figure 3.5. The

gate beam and the photoluminescence are directed onto a BBO crystal at a semi-angle of 6°, known as the "mixing angle". The crystal Xtal2 is mounted in a mechanical rotation stage, to enable the phase-matching conditions to be satisfied for a given wavelength. The up-converted light is collected by lens L5, and directed through an aperture to remove the gate and photoluminescence light. Lens L6 refocuses the up-converted photons onto the entrance slit of the spectrometer, through a Schott UG11 or UG1 UV band-pass filter used to spectrally clean the signal. The filter chosen depended upon the up-conversion wavelength, which was in turn set by the gate and photoluminescence wavelengths. The aperture and spectral filter are essential to permit the weak up-converted signal to be detected. After the monochromator, the photons were detected using a liquid Nitrogen cooled CCD with integration times of around one second.

3.3.1.1 Steady-state photoluminescence

To measure the steady-state photoluminescence of a sample (as shown in Figure 3.1), the experiment must be adapted. The gate beam is blocked, and the up-conversion crystal (Xtal2) is replaced by a further Glan Thompson polarising prism. This allows the polarisation state of the photoluminescence to be measured. The aperture and filter F2 must be removed or changed and the location of the final lens (L6) may need to be moved to optimise the signal. Because of the much larger signal in the steady state mode, care must be taken not to overload the CCD.

3.3.1.2 PLUCS calibration

To obtain reliable results, it is essential that the up-conversion system is calibrated. The two components that require calibration are the crystal angle at Xtal2 and the spectral response of the system as a whole. In both cases, a white-light source is placed at the sample position, and used to substitute the sample photoluminescence

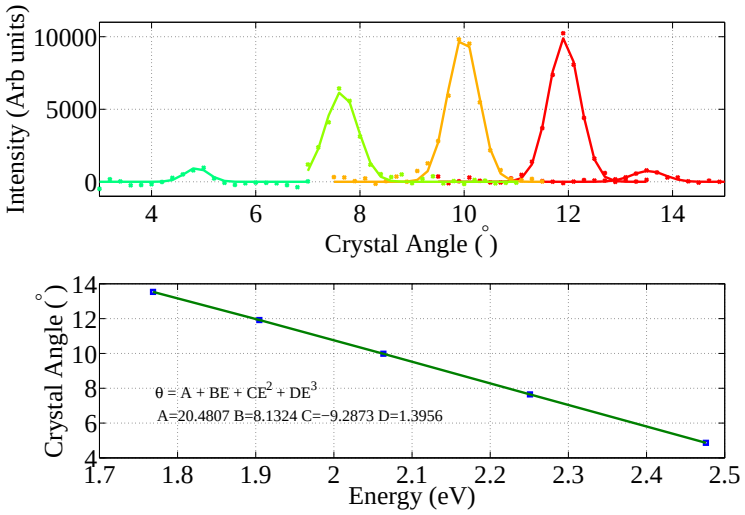

Figure 3.6: The data used to calibrate the crystal phase matching angle (at 900 nm). The upper pane shows the signal versus crystal angle for photoluminescence wavelengths of 500, 550, 600, 650 and 700 nm. The lower figure shows the peak signal angle against photoluminescence wavelength, and a polynomial fit to the data points.

with emission of a known spectrum; it is essential to use a filter (GG400 Schott) after the lamp, to remove any UV components of the white-light that may lie in the same wavelength range as the weak up-converted signal. To calibrate the crystal angle, the monochromator is set to a specific wavelength λ_u. The 'gate' wavelength is fixed at λ_g, so a single photoluminescence wavelength $\lambda_{\mathrm{pl}} = [1/\lambda_u - 1/\lambda_g]^{-1}$ is measured. The crystal angle is then swept to obtain a maximum signal, indicating good phase-matching. Figure 3.6 shows the results of this procedure for a 'gate' wavelength of 900 nm. The polynomial fit to the peak signal angle against photoluminescence energy is used by the software to set the crystal angle automatically. As can be seen, the up-converted signal intensity varies dramatically with photoluminescence wavelength. This indicates the importance of determining the spectral response of the system. The spectral calibration relies on both this fit, and the accurate knowledge of the spectrum of the white light source used. Using a calibrated tungsten filament lamp, a full spectrum is taken in steps, by upconverting each wavelength and setting the

crystal angle and spectrometer correctly. By comparing the intensity of the spectrum observed $I_{\mathrm{ob}}(\lambda)$ with the known emission spectrum of the lamp $I_{\mathrm{lamp}}(\lambda)$, the response of the system at each wavelength can be calculated as $R = I_{\mathrm{ob}}(\lambda)/I_{\mathrm{lamp}}(\lambda)$.

3.3.2 Optical-pump terahertz-probe spectroscopy

The principle behind OPTP-TDS is typical of pump-probe experiments – simply, an excitation pulse is focused onto a sample and after a variable delay, the excitation state of the system is probed using a single cycle of terahertz radiation ($\lambda = 250\,\mu$m, $\hbar\nu = 4.2\,$meV, $\tilde{\nu} \approx 30\,\mathrm{cm}^{-1}$, $\nu = 1 \times 10^{12}\,$Hz). This single cycle can be measured in the time-domain, using the technique of *electro-optic sampling* (as described at the end of this section). This provides the full complex spectrum of the terahertz probe, in contrast to typical optical experiments where only the intensity is retrieved. Before the experimental details are presented, the concepts behind time-domain spectroscopy must be briefly described.

3.3.2.1 Time-domain spectroscopy

In conventional optical spectroscopy, the intensity of electromagnetic radiation is measured, as a function of frequency. This is given by the Poynting vector, defined as $\mathbf{S} = \mathbf{E} \times \mathbf{H}$, where $\mathbf{E}$ is the electric field vector and $\mathbf{H}$ is the magnetic field vector. Given the ratio between the frequencies involved in optical/infrared spectroscopy ($10^{15}\,$Hz) and the highest possible speed of electronic measurement ($\sim 10^{9}\,$Hz), the time-averaged Poynting vector is typically measured. For a plane wave propagating along the $\hat{z}$ axis of the form $\mathbf{E}(t, z) = E_0 e^{i(kz-\omega t)}$, the time averaged intensity is proportional to $|E_0|^2$. A full treatment is given in several basic electromagnetism texts, such as Lorrain [146] or Jackson [147]. This would mean that traditional spectroscopy (reliant upon on a measurement of the intensity as a function of frequency) is incapable of measuring the complex refractive index of a material, due to the loss of phase

information. This problem may be avoided due to the analyticity of the refractive index under certain conditions; the useful technique of Kramers-Kronig analysis stems from the non-local relationship between the electric displacement vector **D** and the electric field **E** [147]. This analysis allows the full complex dielectric function of a material to be retrieved from intensity-based measurements. However, either the real or the imaginary part of the refractive index must be known over a large spectral range, which is not always practicable. Time-domain spectroscopy allows the measurement of the electric field as a function of time, and therefore the simple extraction of the complex refractive index without recourse to Kramers-Kronig analysis. Terahertz time-domain spectroscopy is such a technique, in which the linear electro-optic effect is used to measure the probe electric field directly, as a function of time. In this case, both the phase and amplitude information are available for a given pulse, providing (in theory) the full complex refractive index of a material over the spectral range of the probe. The analysis required to interpret the time-domain signal is presented in a later section.

3.3.2.2 Experimental layout

The Amplifier OPTP-TDS system used is shown in Figure 3.7. This setup was used for the data taken in Chapters 5 and 6. The general system will be described here, while specific relevant details will be provided in the individual chapters. An ultrafast laser pulse from the Spitfire Amplifier is split into two at a beam-splitter BS1, with 50% being used to pump a TOPAS optical parametric amplifier. The second half passes a fixed delay stage (Stage1) to compensate for the path length inside the TOPAS. At BS2, 0.2% of the pulse is split off to be used as the 'gate' pulse. The remainder of the pulse traverses a mechanically controlled delay stage (Stage3), and is directed onto an optical chopper, with a frequency f_1 set and phase locked to half the repetition rate of the laser (500 Hz). This means that one out of every two pulses

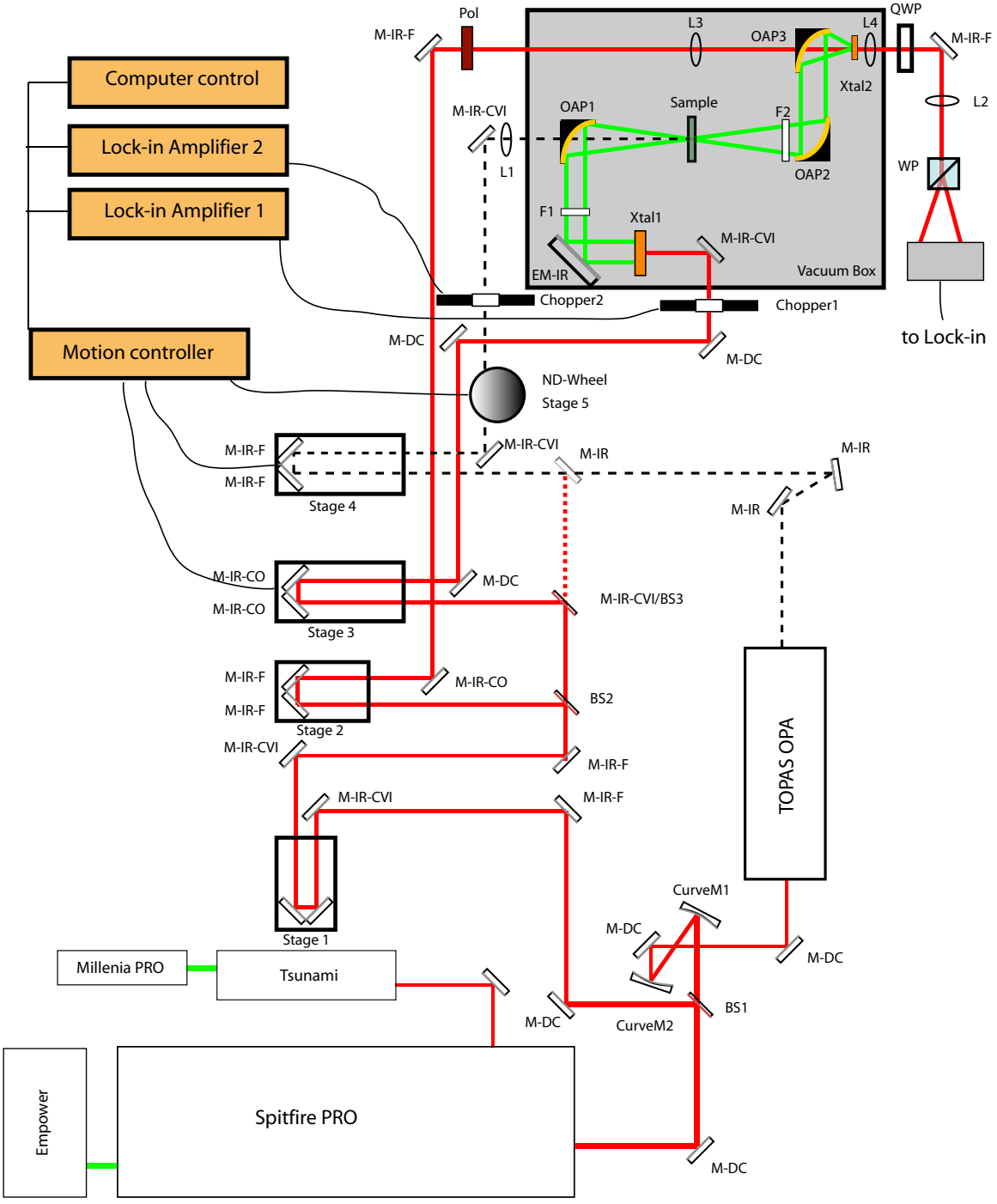

Figure 3.7: The experimental set-up for optical-pump terahertz-probe spectroscopy using the amplifier system. The parts labelled are described in Table 3.2 and 3.3, and the beam-path is described in the text. Note that the entire terahertz beam path is inside the vacuum box at the top right of the figure.

Part	Description
Millenia PRO	Spectra-Physics frequency-doubled Nd:YAG 3.8 W CW
Tsunami	Spectra-Physics Ti:Sapphire Oscillator Pulse duration : 35 fs Centre wavelength : 800 nm Pulse energy : 12 nJ Repetition rate : 80 MHz
Empower	Spectra-Physics Q-Switched Nd:YAG CW power : 7 W Repetition rate : 1 kHz
Spitfire	Spectra-Physics regenerative Ti:Sapphire Amplifier Pulse duration : 50 fs Centre wavelength : 805 nm Pulse energy : 1 mJ Repetition rate : 1 kHz
TOPAS	Light-conversion Optical Parametric Amplifier Output wavelength : 240 nm - 20,000 nm (Requires changing crystal set)
Lock-in Amplifiers	Stanford Research Systems SR830
Motion-Controller	Newport XPS

Table 3.2: Equipment list for the OPTP setup.

Part	Description
M-DC	Mirror : Single stack dichroic, Altechna (Lt.)
M-IR-F	Mirror : Femtosource OA22
M-IR-CVI	Mirror : CVI PS-PM-1037-C
M-IR-CO	Mirror : Comar 25MX06
M-IR-NF	Mirror : New Focus 5103
EM-IR	Elliptical Mirror : Comar 40MD00
BS1	Dielectric 50% beam-splitter
BS2	Femtolasers OA043 0.2% beam-splitter
BS3	Femtolasers OA135 50% beam-splitter
Stage1, Stage2	Manual translation stage
Stage3	Newport M-ILS200PP stepper
Stage4	Newport M-ILS200CCHA DC motor
Stage5	Newport PR50CC rotation stage
Chopper1+2	Signal Recovery 650/651
ND-wheel	Thor labs NDC100C-2 variable ND filter wheel
L1	Comar 160PS25 lens
L2	Comar 125DQ25 lens
L3	Lens, f=100 mm
L4	Comar 60PI25 lens
OAP1,2	JanosTech off-axis parabolic, 90°, f=154 mm
OAP3	JanosTech off-axis parabolic, 90°, f=72 mm
Xtal1	IngCrys 2 mm×25 mm ϕ, ZnTe <110>
Xtal2	IngCrys 1 mm×5 mm×5 mm, ZnTe <110>
Pol	Newport Polarcore polariser
QWP	Newport polymeric quarter-wave plate
WP	Wollaston prism
F1	Cellulose Nitrate IR filter, 1 μm pore size
F2	Teflon Visible filter, 13 mm thick

Table 3.3: Optics list for the OPTP setup.

are allowed to pass, and are guided onto the Zinc Telluride optical rectification crystal (Xtal1). The choice of chopping rate is important for obtaining a good signal to noise ratio. A frequency of half the Amplifier repetition rate is the highest frequency that preserves two pulses in every on-off cycle.

During the on-cycle, a strong single cycle of terahertz radiation is produced in the ZnTe crystal, and emerges co-linearly with the incident infrared pulse. A thin sheet of Cellulose Nitrate (F1) is used to scatter the remaining optical pulse, but is transparent at terahertz frequencies. The terahertz pulse is focused using a gold-plated off-axis parabolic mirror (OAP1) onto the sample, before being collimated using a second parabolic mirror (OAP2). A third parabolic mirror (OAP3) is used to focus the terahertz pulse onto a second Zinc Telluride crystal (Xtal2), where the terahertz electric field is sampled using electro-optic sampling and the gate pulse. Before arriving at the detection crystal, the gate pulse is directed through a polarising filter; electro-optic sampling relies on encoding the electric field of the terahertz pulse onto the polarisation state of the gate, and an initially clean polarisation state is required for a good signal to noise ratio. A lens (L3) is used to focus the gate pulse through a small hole in the centre of the final parabolic mirror (OAP3), forming a spot of approximately 3 mm diameter at the detection crystal.

The optical pump wavelength emerging from the TOPAS optical parametric amplifier may be set[2] in the range 240 nm - 20000 nm. For wavelengths shorter than 450 nm, silver mirrors are no longer useful, and the mirrors in the rest of the path must be changed to those of a UV-enhanced aluminium type. After emerging from the TOPAS, two mirrors (M-IR) are used to ensure no spatial or angular walk-off has occurred within the TOPAS system. The second mechanical stage (Stage4) is used as the pump delay stage. The beam passes through a reflective ND0-ND2 variable neutral density filter in a computer controlled rotation stage. Using this, the power

[2] A crystal set must be changed to reach wavelengths longer than 2000 nm.

may be scanned, or a constant power can be achieved over a varying wavelength range. The second optical chopper (Chopper2) is set to f_2 – a frequency significantly below that of Chopper1 – and care is taken to avoid multiples or integer factors of f_1. A lens (L1) is used to focus the beam onto a hole in the centre of OAP1, and the pump is directed onto the sample position. Care must be taken to ensure a good spatial overlap between the optical pump and the terahertz probe pulses due to the near-diffraction limited spot size of the terahertz probe. Spectral artifacts may arise if this is not the case, as the lower-frequency components of the terahertz probe have a larger spot size than the high-frequency components [148]. The pump-beam is typically around 2 mm in diameter. The whole terahertz beam path is enclosed in a vacuum box, and for a typical experiment the internal pressure will be less than 1×10^{-3} mbar; Water vapour has many terahertz frequency absorption lines which degrade the signal to noise ratio, and oxygen must be removed from samples prone to photo-oxidation or other photodegredation routes. The effect of water vapour can be seen in Figure 3.8, both delaying and attenuating the terahertz signal. The "ringing" after the main pulse is indicative of terahertz spectral absorption.

The optical delay between the optical pump and terahertz probe allows the evolution of the photoexcitation to be probed as a function of time t', over a delay of up to 1250 ps after excitation. The terahertz pulse is sampled by varying the delay between the gate pulse and the terahertz generating optical pulse, denoted by t, and the optical delay scheme is depicted in Figure 3.9. In the arrangement shown in Figure 3.7, the terahertz delay is independent of the pump delay, meaning the instantaneous terahertz conductivity of a sample is measurable without the transformations often required in the literature [149].

The two primary modes of operation of a optical-pump terahertz-probe experiment are referred to as *fixed-gate* and *fixed-pump* mode. For the fixed-gate mode, the photo-induced change in peak terahertz transmission is measured as a function of pump-

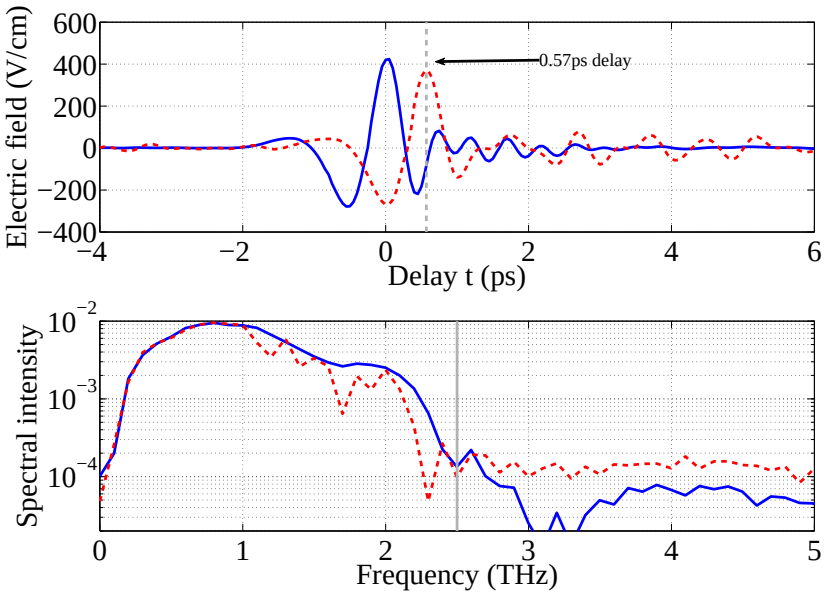

Figure 3.8: A typical terahertz probe trace taken in vacuum (blue solid line) and air (red dashed line) is shown in the top panel, in units of electric field strength. The absolute values of the Fourier Transform of the time-domain data are given in the lower panel; the absorption bands due to water vapour are visible between 1 and 2 THz. The increased refractive index is indicated by the 0.57 ps phase delay in the upper pane. The noise floor is marked by a vertical line at 2.5 THz, limited by phase-matching in the thick ZnTe emitter. Note the two orders of magnitude between the signal max and the noise floor, giving a dynamic range of 100.

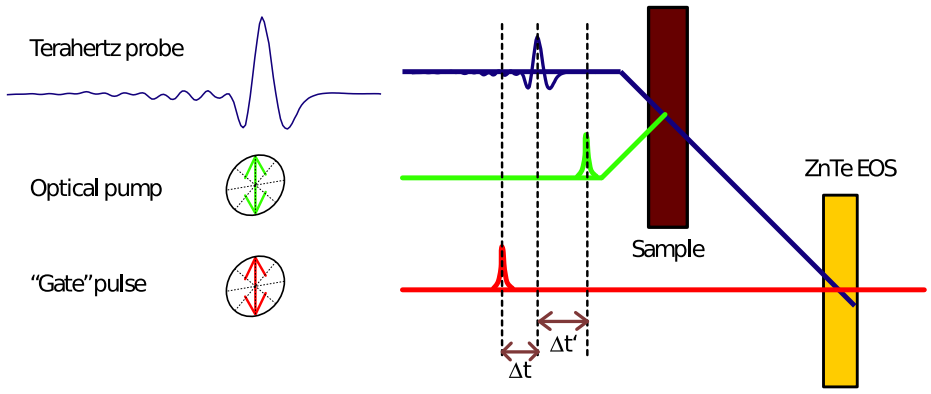

Figure 3.9: A schematic showing the delay scheme in a typical OPTP-TDS experiment. In the experiment described in Figure 3.7, the Gate pulse is fixed, and the terahertz and optical pump pulses are delayed from this by Δt and $\Delta t + \Delta t'$ respectively. By fixing $\Delta t = 0$ and varying $\Delta t'$,a *fixed-gate* experiment is conducted. Alternatively, fixing $\Delta t' = \tau$ and scanning Δt provides the *fixed-pump* configuration.

probe delay. The resulting curves are measures of the frequency-averaged transient conductivity as a function of time after excitation and may yield information on free carrier lifetimes and the evolution of the charge mobility. Additional information can be extracted through operating the experiment in fixed-pump mode – here, the photo-induced change in terahertz time-domain electric field is measured at a fixed pump-delay. From this measurement, the real and imaginary parts of the photoconductivity spectrum across the terahertz range can be determined for a set time after excitation of the sample. A combination of the two modes can be powerful in resolving the full time-resolved electronic dynamics of a sample. Having commented upon the linear optical aspects of the OPTP-TDS experiment, it is useful to briefly explore some of the less common techniques used – primarily, optical rectification, electro-optic sampling, and double lock-in detection.

Optical rectification. To produce terahertz frequency radiation, one powerful method is optical rectification [150]. In a similar manner to second harmonic generation, a single high power ultrafast pulse is incident upon a non-linear crystal, however in this case the difference frequency signal is required [151]. A Gaussian pulse with

duration τ and centre frequency ω_c will have a electric-field

$$E(t) = e^{-t^2/\sqrt{2\ln 2}\tau^2} \cos(\omega_c t). \tag{3.5}$$

If this propagates through a material with a non-zero χ_2, a polarisation equal to

$$P_2 = e^{-2t^2/\sqrt{2\ln 2}\tau^2} \cos^2(\omega_c t) = e^{-2t^2/\sqrt{2\ln 2}\tau^2} \left[\frac{1+\cos(2\omega_c t)}{2}\right], \tag{3.6}$$

is produced, where the first term is the DC or *rectification* term, and the second term is the second harmonic of the fundamental frequency ω_c. The emitted electric field is proportional to the second derivative of the polarisation, $E_{\mathrm{THz}} \propto P''$, leading to an emitted pulse that resembles that shown in Figure 3.8. The second harmonic is typically not seen, because it would require a different phase matching condition. An appropriate choice of non-linear crystal allows this pulse to be phase-matched with the generating optical pulse, and a resultant high terahertz generation efficiency, with the upper frequency limited by the phase-matching conditions, and ultimately the duration of the incident pulse[3].

Electro-optic effect. We turn to electro-optic detection and the Pockels effect in order to detect the terahertz radiation [144, 152, 153]. This case is slightly different from the non-linear effects set out previously, and uses the interaction of an ultrashort laser pulse 'gate' with the terahertz pulse to encode the terahertz electric field onto the polarisation state of the gate as shown in Figure 3.10. Because the ultrafast pulse has a duration on the order of 50 fs while the terahertz fields used in this study have a period of around 1 ps, the terahertz field appears quasi-static on the timescale of the gate pulse. For terahertz applications, Zinc Telluride or Gallium Phosphide of a $< 110 >$ cut are most frequently used [154].

[3] In other words : *"the spectral bandwidth of the radiation should be the same as that of the optical pulse if the dispersion effect can be ignored"* – from Reference [150].

Figure 3.10 schematically depicts the electro-optic sampling process used in our system; the basic concept follows that of Valdmantis *et al.* [155]. The terahertz electric field is first encoded onto the polarisation state of the gate, secondly a quarter-wave plate (QWP) is used to afford a $\pi/4$ bias to the probe beam, which allows the system to be operated in the linear regime. The Wollaston prism (WP) is used to separate the elliptical probe into horizontal and vertical components, and a pair of biased p-i-n photodiodes are used to detect the relative intensity of the two components. In normal operation, the differential output from the biased photodiodes is set to zero without the terahertz pulse present by rotating the quarter-wave plate. This means that the change in polarisation is related directly the voltage detected across the photodiodes V and the maximum voltage swing V_{max} by $\Delta\phi = V/V_{\mathrm{max}}$. In this regime, the electric-field of the terahertz pulse at the crystal can be directly calculated, as the phase-retardation induced in the electro-optic crystal is given by

$$\Delta\phi = \frac{2\pi}{\lambda_{\mathrm{gate}}} d n_{\mathrm{gate}}^3 r_{41} E_{\mathrm{THz}}, \tag{3.7}$$

where λ_{gate} and n_{gate} are the wavelength of the gate and refractive index at the gate wavelength respectively, d is the crystal thickness and r_{41} is the electro-optic coefficient of the crystal. A complete treatment requires calibration of the frequency-response of each crystal used, however, this is less important for pump-probe spectroscopy where only the relative change in terahertz field is of interest. Techniques for calibration are given in Chapter 2 of Reference [156] and in Reference [157].

Double lock-in detection. A pair of lock-in amplifiers are used for signal recovery in OPTP-TDS. The first is referenced to Chopper1 at 500 Hz (half the amplifier repetition rate), while the second is referenced to the pump Chopper2 at a lower rate (typically 42 Hz). The output from the first lock-in is proportional to the terahertz signal E_{THz}, via Equation 3.7. The output from the second lock-in is proportional to

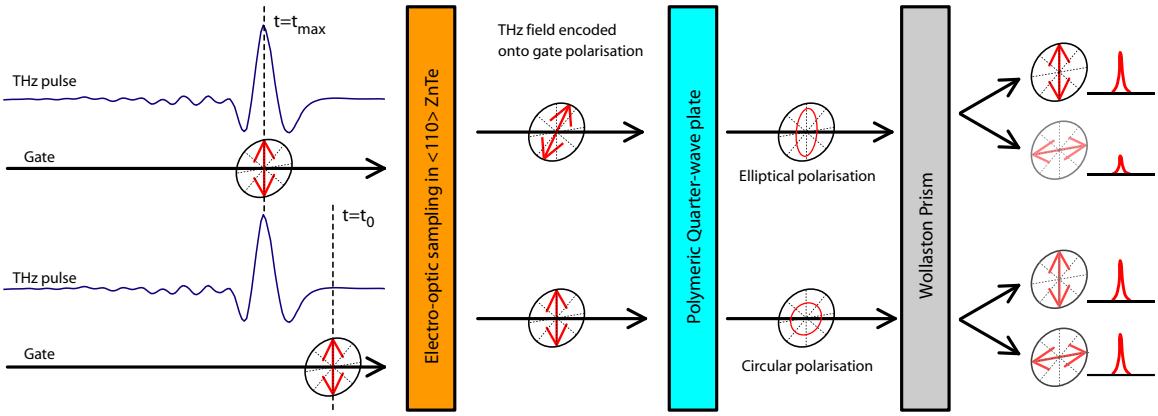

Figure 3.10: A schematic showing the electro-optic sampling procedure used in the experiment. Initially, the delay between the terahertz pulse and the gate is set, and the temporally overlapped electric field of the terahertz is encoded onto the polarisation state of the gate. The quarter-wave plate balances the two linear polarisation components, before the Wollaston prism is used to separate the components. The relative intensity of each state is given at the right, and provides the differential signal that can be detected using photodiodes. The depolarisation of the 'gate' pulse is exaggerated, typically rotations smaller than 10% are expected.

the pump-induced change in terahertz transmission, $\Delta E = E_{\text{on}} - E_{\text{off}}$. The interplay between the time-constant of each lock-in (τ_1 and τ_2), the chopper frequencies (f_1 and f_2) and the delay between acquiring each point t_{settle} is important, and must fulfil the requirements:

$$\begin{aligned} \tau_1 &\gg 1/f_1 \\ f_2 &\ll 1/\tau_1 \\ \tau_2 &\gg 1/f_2 \\ t_{\text{settle}} &\gg \tau_2 \end{aligned}$$

If the above conditions are satisfied, the signal is a true representation of the pump-induced change in transmission. The interpretation of the raw data E_{THz} and ΔE as a function of t and t' is addressed in the next section.

3.3.3 Extracting the complex conductivity of a sample

This section introduces the method of obtaining the complex conductivity of a photoexcited sample from the experimental data. After the time-domain electric field and photo-induced change in electric field have been obtained, it is useful to move into the frequency domain, as this is where spectroscopic information of interest lies. For a time domain electric field in vacuum of the form $\mathbf{E}(t) = E_0 e^{-i\omega t}$, the frequency-domain counterpart is given by

$$\tilde{\mathbf{E}}_{\mathrm{v}}(\omega) = \tilde{E}_0(\omega) e^{i\omega d/c}, \tag{3.8}$$

where c is the speed of light, d is the distance travelled and $\tilde{E}_0(\omega)$ is the spectral amplitude of the field.

3.3.3.1 Equilibrium refractive index

When a sample is placed in the terahertz beam, the complex refractive index $\tilde{n}$ alters the detected field. It has the effect of introducing reflections at each interface (which may give rise to the Fabry-Perot effect), as well as adding phase delay and attenuating the pulse, each of which may have a frequency dependence. A typical geometry is shown in Figure 3.11, where the path before and after the sample are taken to be vacuum ($\tilde{n}_v = 1$). For this arrangement, the detected pulse may be described by

$$\tilde{\mathbf{E}}_{\mathrm{s}}(\omega) = t_{\mathrm{vs}} t_{\mathrm{sv}} F P_{\mathrm{vsv}}(\omega) E_o(\omega) e^{i(\omega d/c)\tilde{n}}, \tag{3.9}$$

where the subscripts v and s refer to the vacuum and sample respectively, and t_{ij} is the Fresnel transmission coefficient at the interface of regions i and j, defined by

$$t_{\mathrm{ij}} = \frac{4\tilde{n}_{\mathrm{i}}\tilde{n}_{\mathrm{j}}}{(\tilde{n}_{\mathrm{i}} + \tilde{n}_{\mathrm{j}})^2}. \tag{3.10}$$

The term FP relates to the Fabry-Perot effect, as shown in Figure 3.11, and has the effect of creating 'echoes' of the pulse in the time domain, and an interference type effect in the frequency domain. The Fabry-Perot effect may be neglected in certain situations; when the film is thick ($> 1\,\mathrm{mm}$) the echoes may be removed by temporal windowing of the pulse, and where it is very thin ($< 10\mu\mathrm{m}$) the reflections lie so closely overlapped in time, the effect is eliminated [158]. A comparison of Equations 3.8 and 3.9 shows that the complex refractive index may be obtained by dividing the two quantities. The complex transmission coefficient of a sample may be defined as

$$\tilde{T}(\omega) = \frac{\tilde{\mathbf{E}}_{\mathrm{s}}(\omega)}{\tilde{\mathbf{E}}_{\mathrm{v}}(\omega)} = t_{\mathrm{vs}} t_{\mathrm{sv}} F P_{\mathrm{vsv}}(\omega) e^{i(\omega d/c)(\tilde{n}-1)}. \tag{3.11}$$

Unfortunately, the presence of the complex refractive index in the Fresnel transmission components, the Fabry-Perot term and the exponential mean that in general, Equation 3.11 cannot be solved in an analytical form. Numerical procedures for obtaining it have be been outlined by Duvillaret [159]. In the situation that the Fabry-Perot term is neglected (as suggested above), then by assuming the Fresnel transmission terms are independent of frequency ($t_{\mathrm{vs}}(\omega) = t_{\mathrm{vs}}(\omega = 0)$) an analytic solution for $\tilde{n}$ as a function of $\tilde{T}(\omega)$ may be obtained.

3.3.3.2 Complex conductivity

For OPTP-TDS, the conductivity of the photoexcited sample is required, and the treatment differs from the equilibrium case. The three measured frequency domain electric fields are $\tilde{E}_{\mathrm{v}}(\omega)$,$\tilde{E}_{\mathrm{s}}(\omega)$ and $\tilde{E}^{*}_{\mathrm{s}}(\omega)$, where the final is that measured for the photoexcited material and $\Delta\tilde{E}(\omega) = \tilde{E}^{*}_{\mathrm{s}} - \tilde{E}_{\mathrm{s}}$. To obtain the photoconductivity of the sample, the relationship between the complex refractive index and the conductivity must be explored. Starting from Maxwell's Equations and a definition of conductivity as $\mathbf{J} = \sigma\mathbf{E}$, the electromagnetic equation describing the arrangement shown in

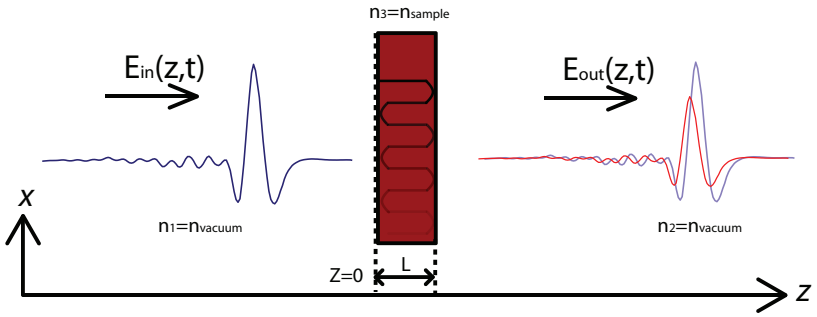

Figure 3.11: The geometry and definitions used for calculating the complex conductivity. The pulse moves along the z axis, with $z = 0$ defined at the sample surface. The pulse shown in blue represents the vacuum or reference signal, while the red pulse represents the signal in the presence of the sample. For simplicity, all media except the sample are taken to be vacuum. Note the reflections inside the sample which give rise to the Fabry-Perot effect.

Figure 3.11 is given by

$$c^2\nabla^2\mathbf{E} = \epsilon_0\sigma\frac{d\mathbf{E}}{dt} + \epsilon_r\frac{d^2\mathbf{E}}{dt^2} + \frac{\nabla\rho}{\epsilon_0\epsilon_r}. \tag{3.12}$$

In an insulating sample, or one where the charge density ρ does not vary with spatial position z, the final term can be set to zero, as $\nabla\rho = 0$. In this case, using the time-domain plane field *ansatz* of the form $\mathbf{E}(t,z) = E_0e^{i(kz-\omega t)}$, the wavevector k becomes

$$k^2 = \frac{i\epsilon_0\sigma\omega}{c^2} + \frac{\epsilon_r\omega^2}{c^2}. \tag{3.13}$$

Using the dispersion relationship given by $k/\omega = \tilde{n}/c$, and the definition $\tilde{n} = \sqrt{\epsilon_r}$, the complex refractive index may be finally related to the conductivity by

$$\tilde{n}^2 = \epsilon_\infty + \frac{i\epsilon_0\sigma}{\omega} \tag{3.14}$$

where ϵ_∞ is the high-frequency dielectric constant of the material.

3.3.3.3 Non-equilibrium conductivity in thin films

In the OPTP-TDS case, the complex conductivity $\sigma(\omega, t)$ becomes a function of time after photoexcitation. A combination of the treatments in Section 3.3.3.1 and 3.3.3.2 are required; in doing this, the method of Lui [160] will be followed. For the geometry in Figure 3.11 and the case of an optically thin film with a small photo-induced change in terahertz transmission ($\Delta E < 10^{-3}E$) – satisfied for almost all measurements upon organic semiconductors – the following relationship is found:

$$\Delta\sigma(\omega) = \frac{(n_1 + n_2)}{LZ_0}\left(\frac{1}{1 + \frac{\Delta E(\omega)}{E(\omega)}} - 1\right), \tag{3.15}$$

where Z_0 is the impedance of free space. In this thesis, it should be noted that both $\Delta T/T$ and $\Delta E/E$ will be used to represent the photoinduced change in terahertz transmitted field. A rigorous study of the relationship between photoconductivity and differential terahertz transmission has recently been reported by Kuzel *et al.*[161], which found the same equation for the specific case of a very thin film and very small $\Delta E/E$. This includes the films studied in Chapter 6, due to the large penetration depth at the wavelengths used. It must be noted that at early times, and particularly where the photoconductivity changes significantly within the terahertz pulse duration a more careful analysis must be used as reported in References [158, 161, 162].

Equation 3.15 is valid for both *fixed-gate* and *fixed-pump* modes, and was used for the study presented in Chapter 6[4]. A typical reference semiconductor is semi-insulating Gallium Arsenide (SI-GaAs), chosen for high carrier mobility ($\mu = 9400\,\mathrm{cm}^2/\mathrm{Vs}$ at 300K) and a band-gap conveniently close to the fundamental output of the Spitfire laser ($E_g = 1.424\,\mathrm{eV}$, and $E_\lambda = 1.55\,\mathrm{eV}$, respectively) [163]. Figure 3.12 shows the results of a *fixed-gate* experiment using a bulk SI-GaAs sample. The sensitivity of the experiment (and particularly the double lock-in signal recovery technique) is demon-

[4]For the nanowire study in Chapter 5, an alternative equation was used, as shown and discussed in Appendix A.

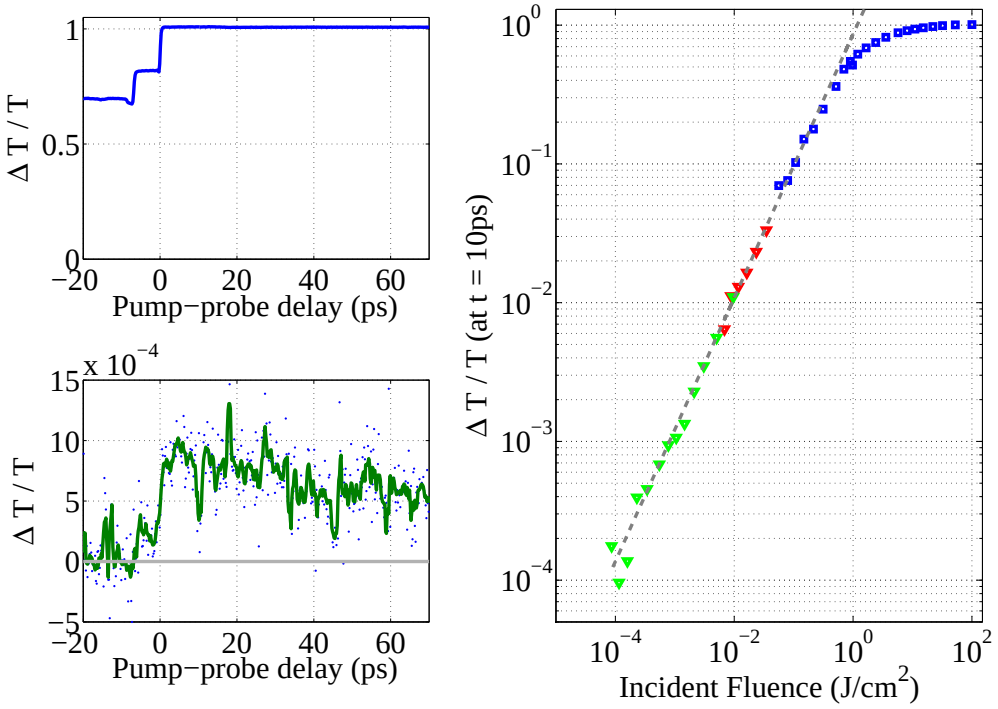

Figure 3.12: An example of an OPTP-TDS experiment on SI-GaAs taken using the system described in Section 3.3.2. Figures a) and b) show the results of a *fixed-gate* scan at a) high ($100\,\mathrm{J/cm^2}$) and b) low ($780\,\mu\mathrm{J/cm^2}$) pump fluence. The non-zero signal at negative time is from a small pre-pulse at -96 ps – however, due to trap saturation at higher fluence it appears relatively large. Figure c) shows the peak $\Delta T/T$ over a pump fluence varying by 6 orders of magnitude. The colours are representative of the fluence range, whilst squares and triangles represent single lock-in and double lock-in measurements, respectively. The dashed line is a guide to the eye representing a sub-linear power-law curve where $\Delta T/T \propto F^{0.95}$.

strated with conductivity detected over four orders of magnitude, with optical-pump fluence varied by six orders of magnitude. Whilst the interpretation of *fixed-gate* experiments as shown in Figure 3.12 are fairly intuitive, the analysis and interpretation of the *fixed-pump* mode can be complicated by the presence of quasi-particles other than free carriers, and will be discussed below.

3.3.4 Interpretation of the photoconductivity

One of the fundamental strengths of OPTP-TDS is that the energy range of the terahertz probe is significantly below the band-gap of typical semiconductors, meaning it can act as a true probe of the photoexcited state of the system. Many quasi-particles do, however, exhibit terahertz frequency absorption, either through a Drude-type absorption (i.e. free-charge carriers), or quantised absorption bands (i.e. excitons, plasmons, polarons, polaritons, charge density waves [164]). The most common will be described here, and the specific case of localised surface plasmons is discussed in more detail in Chapter 5.

Free charge carriers. The Drude model starts from the idea of a gas of electrons – known as a plasma – which are free to move within a sample. No collisions exist apart from scattering by ionic cores, the carriers are treated as non-interacting, and scattering events randomise the momentum of a charge carrier at a rate equal to τ^{-1} where τ is known as the scattering time [4]. Even with these stringent approximations, this model has been frequently and successfully used to describe the terahertz conductivity of inorganic and molecular semiconductors [94, 107, 149]. By solving the differential equation for a damped forced oscillator, the conductivity is given by

$$\sigma(\omega) = \frac{Ne^2\tau}{m^*\left(1 - i\omega\tau\right)}, \tag{3.16}$$

where N is the carrier density, m^* is the carrier effective mass, and e is the fundamental electric charge. The tell-tale signs of a Drude-like response are a positive maximum in the real part of the conductivity at $\omega = 0$, and a minimum in the imaginary part at $\omega = \tau^{-1}$ [13].

Plasmons and surface plasmons. In a Drude-type treatment, the carrier cloud is treated as a free plasma with damping due to the ionic cores. The carriers are

able to oscillate around their equilibrium position, and the harmonic oscillation frequency of the bulk plasma is given by $\omega_p = (Ne^2/\epsilon_0 m^*)^{1/2}$ (known as the plasma frequency). Quantised plasma oscillations are known as plasmons, and plasmonic absorption can be observed directly in doped semiconductors using Raman scattering or using terahertz spectroscopy [165]. In addition, surface collective oscillations have been observed in thin metallic films, known as surface plasmons [136]. In general, coupling electromagnetic radiation into or out of surface plasmons is forbidden, however, in the case that the radiation possesses a significantly longer wavelength than the structure or by use of evanescent wave coupling in a prism arrangement, direct observation is possible [166]. As the frequency and hence energy of the plasmonic absorption is directly related to the carrier density (and sample geometry in the case of surface plasmons), observation of a plasmonic feature can allow accurate determination of the carrier density in a sample.

Semi-free charge carriers. The Drude model does not model the electronic properties of nanoscale materials – or organic semiconductors –accurately. For this reason, a variety of models have been proposed. In particular, several adaptations of the Drude model have been reported with varying levels of popularity, such as those described by Smith [167, 168], the Cole-Davidson [169] or Cole-Cole model [170]. Each model adds free parameters to the basic Drude model, and care must be taken to fully account for any quasiparticle absorption bands before using these models [158]. This topic will be briefly addressed in Chapter 5.

Excitons. As described in the previous chapter, excitons are Coulombically bound electron-hole pairs, and are the primary photogenerated species in pristine conjugated polymers. In inorganic semiconductors, the binding tends to be weak leading to relatively large electron-hole separations. In this case, it is common to model the energy states of the free exciton as a hydrogenic system, permitting the use of the

Bohr model. In the Bohr model, the excitonic energy levels n are defined as

$$E(n) = -\frac{\mu}{m_0}\frac{1}{\epsilon_r^2}\frac{R_H}{n^2} \tag{3.17}$$

where R_H is the Rydberg constant, ϵ_r is the dielectric constant of the bulk material, μ is the reduced ("centre of mass") mass of the pair and m_0 is the electronic mass. Terahertz frequency exciton absorption has been noted in inorganic semiconductors [171–174] but has not been directly observed in polymeric semiconductors. As stated in Chapter 2, excitons in polymeric semiconductors are strongly coupled to the polymer backbone. In this case, Equation 3.17 is no longer valid, as the exciton is tightly bound, leading to a higher exciton binding energy far above the range of the presented terahertz experiment. However, the low frequency tail of the exciton absorption has been identified as contributing to the photoexcited terahertz spectrum of organic semiconductors, appearing as an imaginary conductivity component. This is often modelled using the Clausius-Mosotti relation, resulting in an excitonic conductivity given by $\sigma_{\text{ex}}(\omega) = -\epsilon_0\omega\Delta\epsilon$. The terahertz frequency absorption spectrum of excitons is discussed further in Chapter 6.

Chapter 4

Energy dynamics in Polymer-intercalated SnS_2 nanocomposites

4.1 Background : White-light emitting OLEDs

In this chapter, experimental results of photoluminescence from polymer blends are presented, and the influence of the dimensionality upon energy transfer is discussed. In Chapter 1, the huge potential for incorporating organic semiconductors into traditional optoelectronic applications was introduced. In particular, the field of OLEDs is well developed, and high efficiency organic light-emitting diodes have been demonstrated in the literature [8, 9]. One of the advantages of organic semiconductors over inorganics is the wide tunability of the band-gap through simple changes in the chemical structure. This has led to a rapid expansion in the applications of full-colour light-emitting displays incorporating organic materials and fuelled work towards stable white-light-emitting diodes for solid-state lighting [175]. One promising approach has been the blending of various conjugated polymers, each with a different emission

wavelength [176, 177]. A disadvantage of this method is that ultrafast energy transfer from the high-energy to the low-energy band-gap component of the blend rapidly quenches the photoluminescence from the blue end of the spectrum. This strong interaction between the components makes such materials extremely sensitive to doping levels and film morphology, both of which may in turn be influenced by processing conditions and change over time. An alternative approach suggested by Aharon *et al.* [11, 178] is based on the confinement of the polymer blend in the interlayer galleries of an inorganic semiconducting material that is largely transparent over the visible spectrum. The formation of quasi-two-dimensional polymer monolayers within this nanocomposite should inhibit energy transfer between the polymer blend components allowing stable tuning of the apparent emission colour though changes in the blend composition, in a process depicted in Figure 4.1. The dimensionality of these systems plays an important role here, with one-dimensional transfer of excitations along the chain typically being much slower than that within a three-dimensional polymeric solid [45, 179–181]. Using this approach, stable white-light emission has recently been demonstrated for a nanocomposite containing a blend of three polymers emitting in the blue, green and red regions of the visible spectrum [11]. The inorganic interlayers may have the additional functions of aiding charge carrier injection [11] and protecting the polymer against degradation through encapsulation. In addition, the nanocomposites are produced using supramolecular self-assembly of the components in solution. This technique coupled with the following results confirm one of the strongest advantages of organic semiconductors – that of solution processability, whist retaining morphological control of the final material on the nanoscale.

In this chapter, a study of how the energy transfer dynamics in a conjugated polymer solid are altered when moving from a three-dimensional (3D) film to a quasi-two-dimensional (2D) monolayer are studied. This is achieved by intercalation of optoelectronically active polymers into a SnS_2 matrix. Through measuring the de-

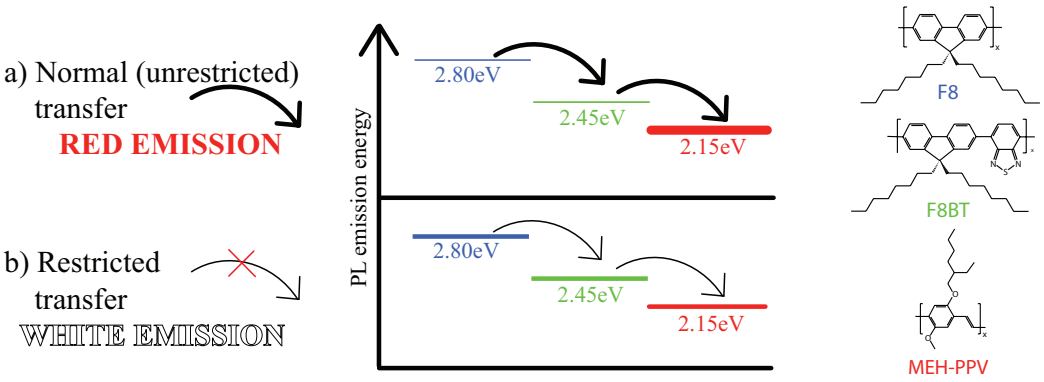

Figure 4.1: The schematic diagram illustrates energy transfer from an initially excited large band-gap (blue emitting) polymer known as the donor, to smaller band-gap (green and red emitting) polymers known as the acceptor. This can be an extremely fast process; without sufficient care, the smallest band-gap polymer can act as an effective photoluminescence quenching site for the larger band-gap polymers. By restricting the energy transfer between polymer chains, emission from all three chromophores can be realised, generating quasi-white light. On the right, the chemical structure of the three polymers in the blend are given.

cay of the blue-light-emitting polymer component (the "donor") both in the presence and the absence of the green- and red-light-emitting polymers (the "acceptor") the excitation transfer rate from the donor to the acceptor is experimentally assessed. Comparison of this data with a simple model that extends Förster's theory [59] for resonant dipole-dipole electronic coupling to systems of different dimensionality indicates that polymer-intercalation into an inorganic matrix indeed results in excitation transfer characteristic for a truly two-dimensional polymeric solid.

4.2 Experimental details

Polymer blend monolayer (2D) samples were fabricated by intercalation of polymer into SnS_2 as described in Reference [11][1]. This procedure is based on the exfoliation-adsorption technique shown in Figure 4.2, in which an inorganic host material (SnS_2 in this case) is delaminated in solution into single sheets that then restack in the presence

[1]The samples were prepared and supplied by Dr. E. Aharon and Prof. G. Frey of the Technion-Israel Institute of Technology, Israel.

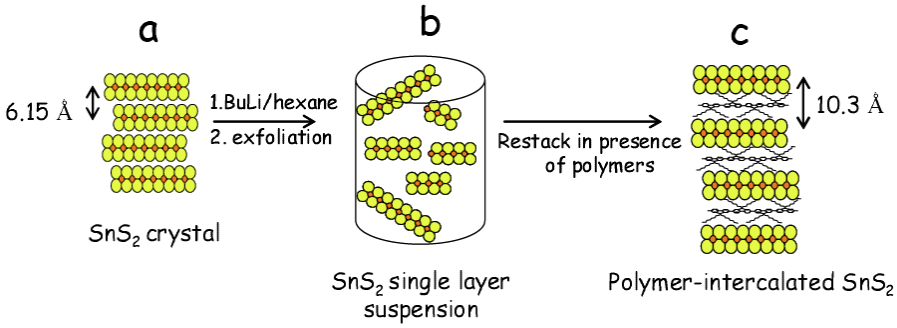

Figure 4.2: The schematic diagram illustrates the processes of exfoliation-intercalation, and the type of layered composite formed when the polymer blend is intercalated between layers of inorganic SnS_2 crystal. Taken from the Supporting Information to Reference [11].

of the conjugated polymer. After polymer incorporation, the mixture was repeatedly washed in organic solvents to remove excess polymer not enclosed in the inorganic matrix. The resulting material was re-dispersed in xylene and deposited on silica substrates through drop-casting. Wide-angle X-ray diffraction measurements on these nanocomposites showed a peak corresponding to the 0.58 nm c-axis spacing of SnS_2 crystals and an additional peak at a 2θ corresponding to 1.04 nm indicating a crystal interlayer expansion of 0.46 nm through incorporation of the polymer [11]. This expansion is of similar magnitude to that reported for related polymer-intercalated materials [182]. It is caused by the tendency of conjugated polymers to adopt a planar conformation in layered compounds [11] indicating that a single monolayer of polymer forms between SnS_2 layers. Three types of nanocomposites were prepared: one incorporated a blend of blue-light-emitting F8[2], green-light-emitting F8BT and red-light-emitting MEH-PPV at a weight ratio of 30:60:10, respectively. Figure 4.1 shows the chemical structures of the polymers used. A reference composite incorporated only F8 to allow the examination of the donor luminescence in the absence of the acceptors and another composite incorporated only MEH-PPV to allow the examination of the acceptor luminescence in the absence of the donor. In addition, 100 nm-thick (3D) polymer films were prepared by spin-casting either the F8:F8BT:MEH-PPV blend

[2]F8 is often referred to as 'PFO' in the literature.

or just F8 from solution in xylene onto silica substrates. The molecular weights of the polymers used were 74000 g/mol and 16000 g/mol for F8 and F8BT (both purchased from *American Dye Source*) and 50000 g/mol for MEH-PPV (purchased from *Aldrich*.)

To investigate the energy-transfer dynamics in these materials, time-resolved photoluminescence up-conversion spectroscopy (PLUCS) was used, as described in Section 3.3.1. The excitation energy was set to either 2.88 eV to excite MEH-PPV, or 3.1 eV to excite F8 preferentially. The excitation beam was focused onto a spot size of 200 μm at powers below 1 mW (< 0.4 mJ/pulse/m^{-2}) adjusted to ensure that no sample degradation occurred during the measurement. All experiments were carried out with the sample held under vacuum ($< 10^{-4}$ mbar) and were fully reproducible. The temporal resolution of the system was approximately 300 fs as determined from the measured width of the excitation pulse. In this geometry the system detects the photoluminescence with polarisation parallel to the gate beam, and the excitation beam was chosen to have a polarisation parallel to this. The time-integrated PL spectra were measured using an Edinburgh instruments *FLS920* spectrometer[3].

4.3 Results from time-resolved photoluminescence spectroscopy

Figure 4.3 shows the time-integrated photoluminescence spectra of F8 and the blend for (a) the 3D thin film, and (b) the 2D monolayers included in the nanocomposites. For all spectra shown, the samples were excited at an energy of 3.1 eV, creating excitons mainly on the F8 donor. The F8 thin film and the corresponding nanocomposite show an emission peak at 2.82 eV and a progression at 2.67 eV, mediated by

[3]The time-integrated spectra were kindly measured by Dr. C. Dosche and Professor A. Köhler of the University of Potsdam, Germany.

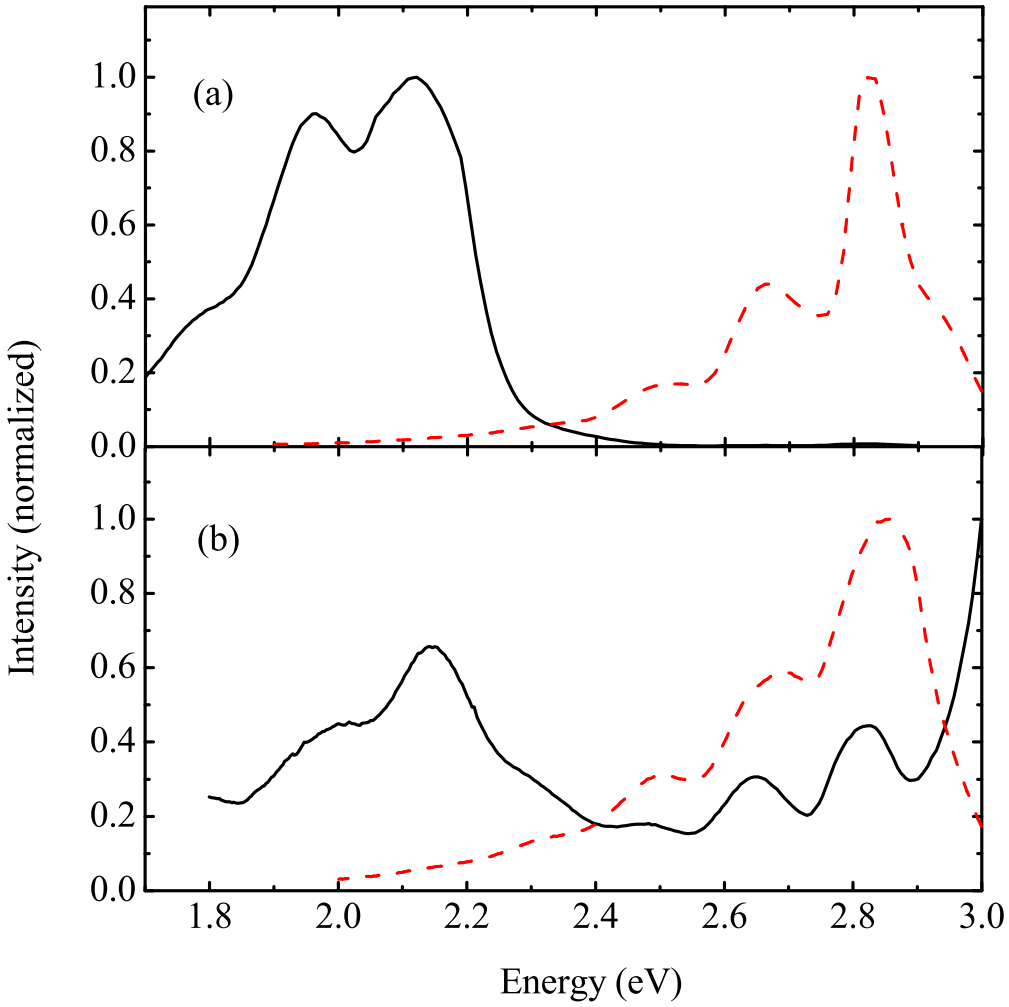

Figure 4.3: Time-integrated photoluminescence spectra for neat F8 (dashed line, red) and for the F8:F8BT:MEH-PPV blend (solid line, black) for the case of (a) thin-film (3D) samples and (b) SnS_2 nanocomposites intercalated with 2D polymer monolayers.

C-C stretch vibrations. However, with addition of the F8BT:MEH-PPV acceptor the thin-film luminescence becomes dominated by MEH-PPV, whose emission peaks may be observed at 2.15 eV, 1.96 eV and 1.8 eV, due to vibronic coupling. The almost complete quenching of both F8 and F8BT luminescence in the blend film indicates an efficient energy transfer to the polymer with lowest band-gap. The nanocomposite incorporating the blend, on the other hand, shows contributions to the emission from all three polymers suggesting that the energy transfer efficiency in the 2D layers of the nanocomposites is significantly reduced. As a result, the emission from the nanocomposite seems white to the eye, in contrast to the red appearance of the emission from the thin film.

In order to obtain information about the rate (and therefore mechanism) of exciton migration from donor to acceptor, time-resolved photoluminescence measurements were carried out to determine the exciton population on F8 and MEH-PPV. Figure 4.4 shows the decay of the F8 (donor) emission (at 2.67 eV) for neat F8 and for F8:F8BT:MEH-PPV blends, both for a thin film (a) and a SnS_2 nanocomposite (b) sample. The decay of the PL from the F8 donor in both the thin film and the nanocomposite becomes more rapid with addition of the F8BT:MEH-PPV acceptor, confirming that energy transfer occurs from donor to acceptor. The relative change in this decay rate is considerably more rapid in the thin film samples than the nanocomposite, suggesting that the nature of the transfer mechanism is strongly modified when moving from a 3D film to a 2D monolayer. For comparison, Figure 4.5 displays the time-resolved photoluminescence from MEH-PPV (at 2.16 eV) both for neat MEH-PPV intercalated in SnS_2 and for the F8:F8BT:MEH-PPV blend intercalated in SnS_2. The neat MEH-PPV incorporated in SnS_2 nanocomposite was directly excited at 2.81 eV and the PL decay is representative of the exciton lifetime on MEH-PPV in the composite. For the F8:F8BT:MEH-PPV blend intercalated in SnS_2, excitation at 3.1 eV predominantly created excitons on F8. Here, a delayed

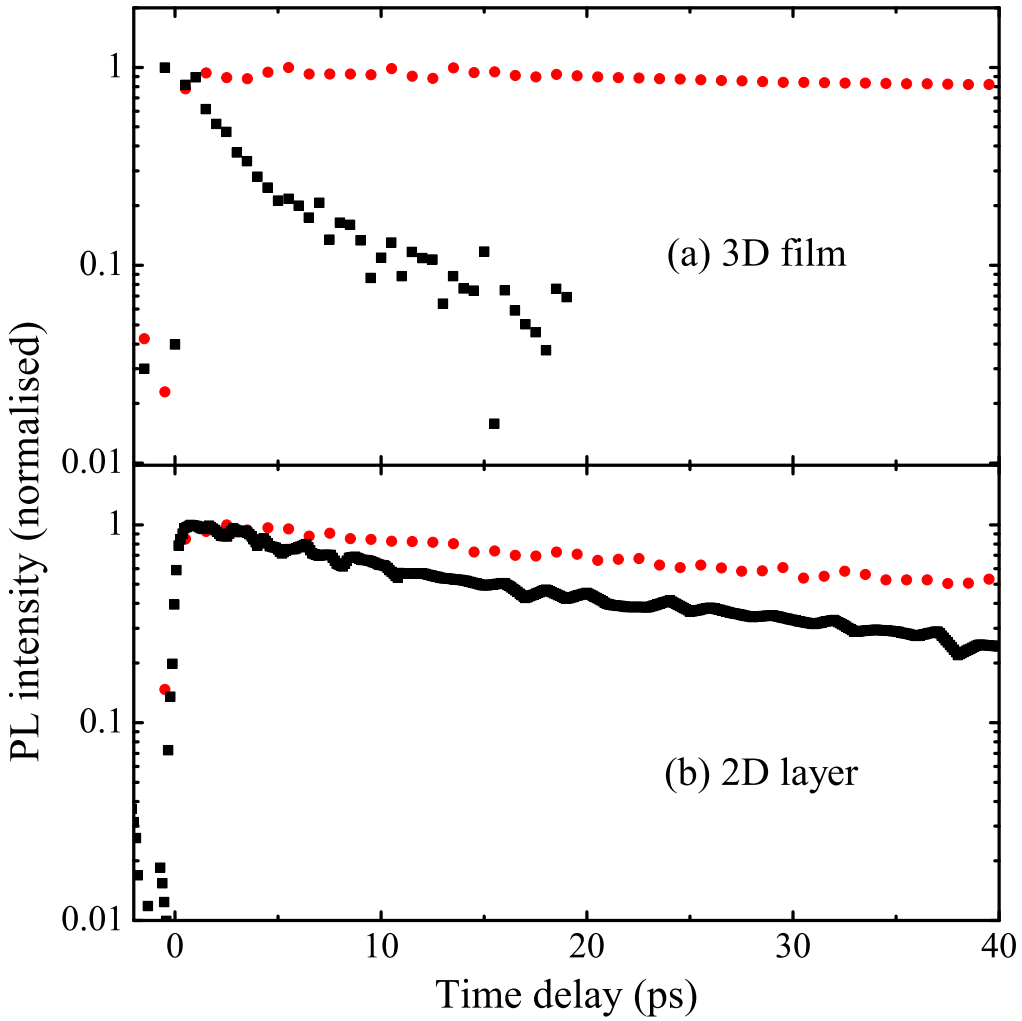

Figure 4.4: Time-resolved photoluminescence decay measured at 2.67 eV. Both the PL from neat F8 (circles, red) and the PL from F8 in the polymer blend (squares, black) are shown for (a) a 3D thin film and (b) 2D layers incorporated a SnS_2 nanocomposite. The decay of the F8 emission can be seen to accelerate slightly upon intercalation as F8 also couples weakly to the SnS_2 matrix, which features an absorption onset in the UV region [11].

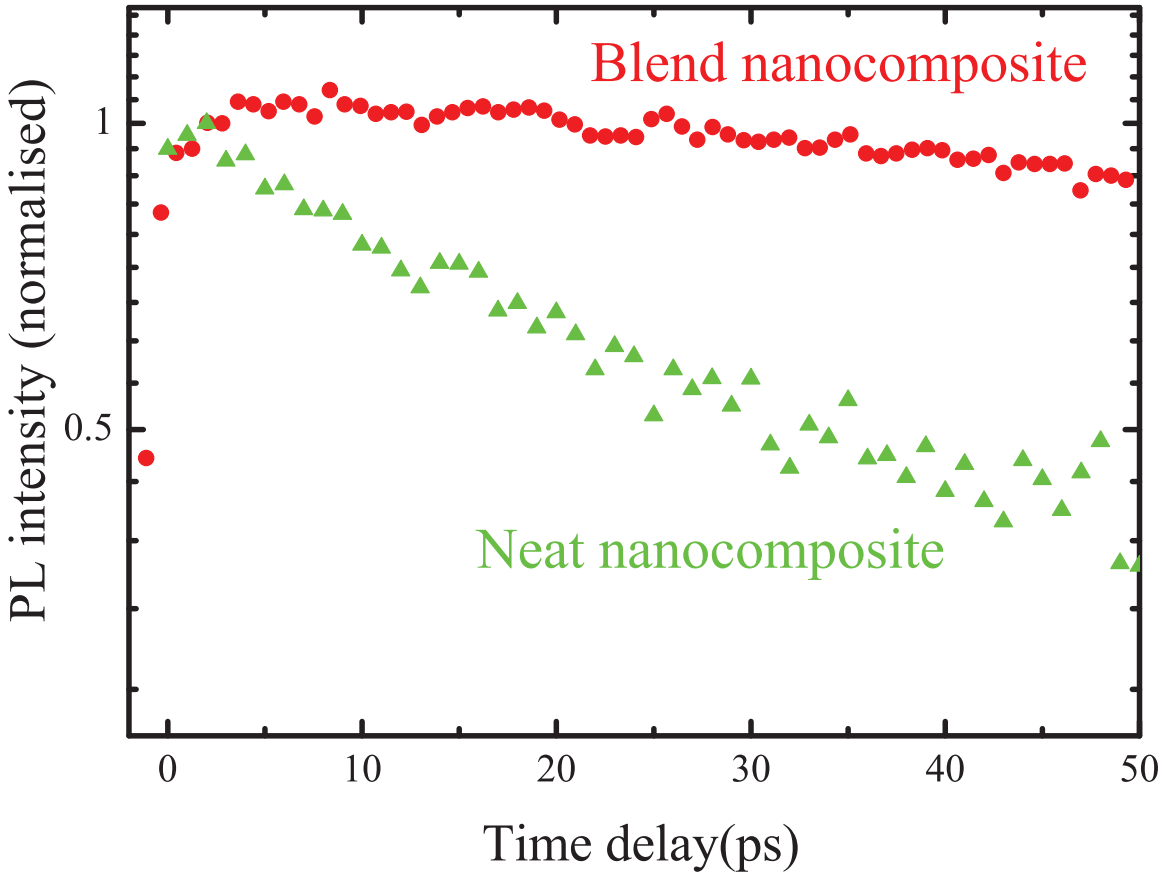

Figure 4.5: Time-resolved photoluminescence decay measured at 2.16eV. Both the PL from neat MEH-PPV intercalated into SnS_2 nanocomposite (triangles, green) and the PL from MEH-PPV in the polymer blend in SnS_2 nanocomposite (circles, red) are shown. An excitation energy of 3.1 eV was used for the polymer-blend-SnS_2, whilst an excitation energy of 2.8 eV was used for the neat MEH-PPV-SnS_2 composite.

rise in the MEH-PPV emission can be observed with an increase in the apparent PL lifetime, in accordance with energy transfer from the donor. However, the dynamics of the MEH-PPV emission in the blend are complex, with the exciton density on the polymer being fed not only by excitation transfer from F8 and F8BT, but also through direct excitation by the laser pulse that is difficult to quantify accurately. For the remainder of this chapter I will therefore focus on the somewhat more tractable analysis of the donor emission from the materials.

4.4 Discussion of dimensionality-dependent energy transfer

Theoretical discussion of energy transfer in π-conjugated donor-acceptor systems generally relies on electric dipole coupling between the emitting transition moment of the donor and the absorptive transition moment of the acceptor [183]. The simplest approximation here is based on interactions between point dipoles, and has been repeatedly applied to conjugated polymeric systems [184–188]. For this case, and as introduced in Section 2.3.2.1, the rate of transfer k was calculated by Förster[59] to be inversely proportional to the sixth power of the acceptor-donor separation r,

$$k(r) = \frac{1}{\tau}\left(\frac{R_0}{r}\right)^6 \tag{4.1}$$

where τ is the excitation lifetime for the donor in the absence of the acceptor, and R_0 is the Förster radius characteristic for the system. However, for an ensemble of randomly distributed chromophores, a range of acceptor-donor distances will be present in the material, requiring an ensemble average to be determined that will also depend on the dimensionality of the system. To analyse the temporal evolution of the excitation within this approximation, the procedure outlined by Baumann and Fayer [185] is followed and applied to the case of a single type of donor. Firstly, by considering only the de-excitation path for the donor that results from energy transfer, the probability of an excitation remaining on the donor molecule is defined as

$$E(t, r) = e^{-k(r)t}. \tag{4.2}$$

Re-transfer of excitation from acceptor to donor chromophore can be ruled out as a result of the negligible spectral overlap of donor absorption with acceptor photoluminescence for these materials. In addition, the relatively small overlap between the

donor absorption and its own emission that is typical of conjugated materials with torsional degrees of freedom [189, 190] allows exciton migration within the donor to be neglected at the high acceptor concentration employed here. This permits the simplification of the full treatment by Baumann [185] and Blumen [191] as outlined in the following. Assuming a random ordering of donors and acceptors, the configurational average of the probability of finding an initially excited donor still excited at time t is

$$G(t) = \prod_{i=1}^{N}(1-p) + pE(t, r_i), \tag{4.3}$$

where p is the probability that a site contains an acceptor and the product extends over N molecular sites. By expanding the logarithm of Equation 4.3, the following is obtained:

$$\ln G(t) = -\sum_{h=1}^{\infty}\frac{p^h}{h}\sum_{i=1}^{N}\left[1 - E(t, r_i)\right]^h . \tag{4.4}$$

The summation over individual sites may then be replaced with an integration over all space, if a continuous spatial distribution is assumed:

$$\ln G(t) = -\rho\phi(p, \Delta)\int_0^{\infty}\left(1 - e^{-k(r)t}\right)u(r)dr\ . \tag{4.5}$$

Here, ρ is a number density of acceptors, $\phi(p, \Delta)$ is a scaling factor related to the proportion of acceptors p and the number of spatial dimensions of the material Δ, and $u(r)dr$ is the probability of finding an acceptor molecule within the distance $[r, r+dr]$ from the donor, multiplied with the dimension-specific volume element. At this point, the effect of dimensionality of the system enters, with the two-dimensional and three-dimensional random acceptor distributions given given through $u_{2d}(r) = 2\pi r$ and $u_{3d}(r) = 4\pi r^2$, respectively. By using as substitutions

$$\mu = \frac{t}{\tau}R_0^6 \quad \text{and} \quad y = \frac{\mu}{r^6} \tag{4.6}$$

$G(t)$ may be simplified for the two- and three-dimensional case as

$$\ln G_{2D}(t) = -2\pi\rho\phi(p,\Delta)\mu^{1/3}\int_0^\infty (1-e^{-y})y^{-4/3}dy \tag{4.7}$$

$$\ln G_{3D}(t) = -4\pi\rho\phi(p,\Delta)\mu^{1/2}\int_0^\infty (1-e^{-y})y^{-3/2}dy\,. \tag{4.8}$$

The integral is independent of t and reduces to a gamma function [192]. The time-dependence of the excitation transfer from the donor, $G(t)$, is solely determined by μ, which in turn is influenced by the number of spatial dimensions. The expected time-dependent PL decay of the donor as a result of energy transfer may be expressed as

$$G(t) = G_0 e^{-(t/t_0)^\alpha}, \tag{4.9}$$

where the t_0 is a system specific time constant related to R_0, ϕ, the acceptor concentration, and the donor's excited state lifetime. The dependence of t_0 on ϕ and therefore the dimensionality complicates the analysis, and prohibits a meaningful value of R_0 from being obtained. The exponent α depends on the number of dimensions in which energy transfer can occur through $\alpha = \Delta/6$, so $\alpha = 1/3$ and $\alpha = 1/2$ should be expected for a two-dimensional and a three-dimensional system, respectively[4].

The experimental data displayed in Figure 4.4 is influenced by de-excitation of the donor through all available mechanisms, while Equation 4.9 is based on energy transfer as the only pathway. To extract information on just the energy transfer rate from the data, the decay of exciton population f in the materials containing only the donor polymer is considered to be described by the following rate equation:

$$\frac{d}{dt}f = -\left(\frac{1}{\tau} + r(t)\right) f(t), \tag{4.10}$$

where τ is the natural exciton lifetime and $r(t)$ is a time-dependent decay rate associ-

[4]For one-dimensional transfer, $\alpha \approx 0.17$ would be expected, significantly outside the range of errors on the measured values of α.

ated with processes such as exciton diffusion to non-radiative traps within the donor system. In the presence of the F8BT:MEH-PPV acceptor, the exciton population on the F8 donor g experiences additional losses,

$$\frac{d}{dt}g = -\left(\frac{1}{\tau} + r(t)\right) g(t) - K(t)g(t), \tag{4.11}$$

where $K(t)$ represents the time-dependent energy transfer rate from donor to acceptor ensemble. It can be shown [187] that within the point-dipole model described above, the ratio $I(t) = f(t)/g(t)$ is directly related to $K(t)$, and follows the time-dependence of $G(t)$ given in Equation 4.9.

Figure 4.6 displays the experimental data for $I(t)$ obtained by division of the F8 emission from the blend by that from the materials containing F8 as the only polymer, both for the case of the 3D polymer film and the 2D monolayer. Superimposed on the data are the best fits based on stretched exponentials [193] as given by Equation 4.9 with α, G_0 and t_0 as free parameters. For monolayers enclosed in the SnS_2 nanocomposites a value of $\alpha = 0.31 \pm 0.04$, while the thin film yields $\alpha = 0.47 \pm 0.07$, close to the values of 0.33 and 0.5 to be expected for the case of two-dimensional and three-dimensional transfer, respectively.

The excellent agreement between this simple model and the experimental data seems surprising at first, given the complexity of the system. First, one might raise the question of whether electronic coupling *between* adjacent polymer monolayers in the nanocomposites also has to be considered. X-ray diffraction from the composites [11] points to the existence of extended SnS_2 crystalline domains, indicating that only a fraction of the adjacent crystal sheets incorporate polymer upon restacking in solution. As a result, the polymer monolayers are sufficiently isolated in the crystal to be considered as non-interacting two-dimensional systems. Another possible complication is that phase segregation between the components of the polymer blend might

lead to a non-random local distribution both in the solid film and the nanocomposites. However, photoluminescence microscopy experiments with 200 nm resolution have indicated uniform distribution of all components [11]. In addition, no residual donor luminescence is observed at long times after excitation, or in the time-integrated spectra, pointing towards a complete transfer of excitation and therefore the absence of large homogeneous donor domains. The two indicators taken together suggest that phase segregation, if present, may only exist over distances that are comparable with the energy transfer range. Whilst the analysis presented above is strictly valid for a two component system and this sample has three, the effect of having two acceptors for the F8 donor to transfer energy to only alters the effective lifetime t_0 in equation 4.9 and thus has no effect on the extracted dimensionality.

Finally, the validity of the point-dipole approximation used in this derivation needs to be examined with care. Quantum chemical calculations predict that an initially created exciton on a conjugated polymer chain is delocalised over a few repeat units [45, 179]. Subsequent lattice relaxation over a typical nuclear vibration period will lead to a localisation of the exciton with a resulting wavefunction extent of the order of one nanometre. Energy transfer over similar length scales is then expected to deviate from calculations using the simple point-dipole approximation. To overcome these limitations, alternative models have been based on line-dipole [194] or distributed monopole [45, 179] approaches. The latter predicts an increase of transfer rate between two conjugated oligomers in head-to-tail geometry and a decrease for a cofacial arrangement in comparison with the simpler point-dipole approximation. The two counteracting effects make it hard to assess qualitatively the overall effect on a solid comprising an ensemble of conjugated oligomers, while a quantitative picture would require demanding computational simulations on generated random morphologies that take proper account of the physical space occupied by the donor and acceptor molecules. For the systems investigated here, deviations from the point-dipole ap-

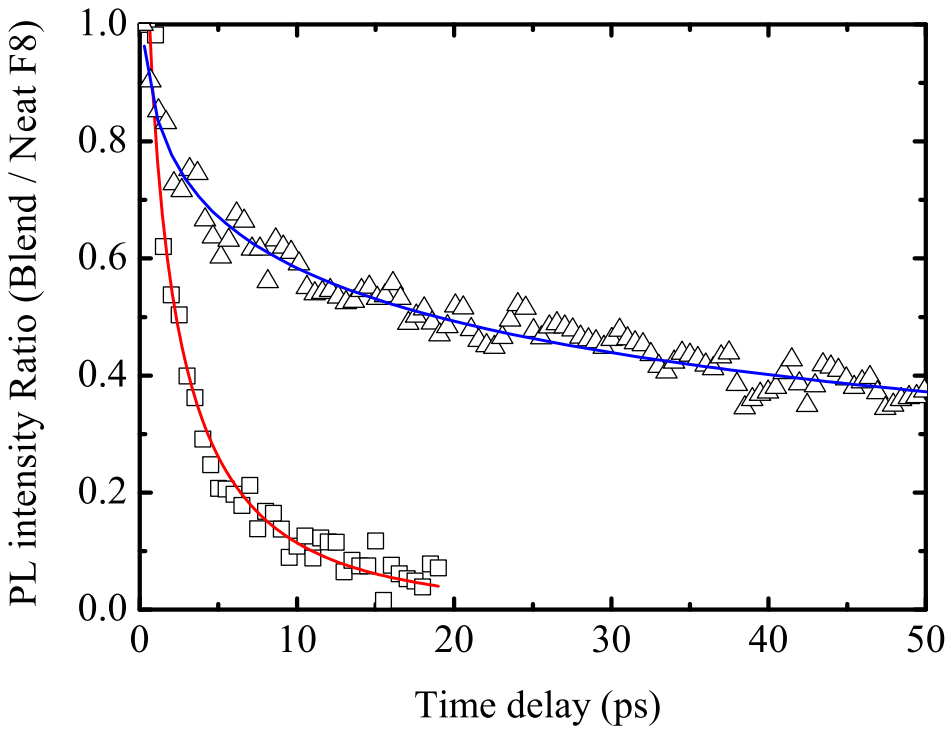

Figure 4.6: Excitation transfer transients, defined as the ratio between the photoluminescence intensity of F8 without acceptor and that with acceptor, shown both for a 3D solid film (squares) and 2D monolayers incorporated in SnS_2 composites (triangles). The solid lines are numerical fits to the data using the model described in the text.

proximation are most likely to be observed for the 3D solid films, for which chains may pack cofacially at distances as short as 3 - 8 $\AA$ [195]. For the SnS_2 nanocomposites the arrangement of a 2D polymer monolayer inhibits such co-facial arrangements leading to a significant increase in the smallest distances over which excitation transfer may occur. As a result, the point-dipole approximation is expected to hold for the case of a 2D polymer monolayer incorporated in this type of nanocomposite.

4.5 Summary

In this chapter, the dependence of dimensionality on the energy transfer in conjugated polymer blends has been examined. For the three-dimensional blend film, excitation

transfer from the donor is almost completed within the first few picoseconds. Intercalation of quasi-two-dimensional polymer monolayers into an inorganic matrix results in slower excitation transfer, which occurs over the timescale of a few tens of picoseconds. For both systems, the transfer dynamics can be described by a stretched exponential with a dimensionality-dependent exponent. A simple model was outlined that is based on excitation transfer through electronic coupling between transition moments considered to be point-dipoles, and takes account of the system dimensionality. Comparison with the experimental data indicates that within these approximations, energy transfer occurs in three dimensions for the solid film, but only in two dimensions when the polymer is incorporated as a monolayer in the SnS_2 nanocomposites, as schematically shown in Figure 4.7. The resulting decrease of the overall rate at which energy is transferred to the lowest-energy component means that emission is clearly observed from all components of the polymer blend incorporated in the nanocomposites. Achieving this task through a reduction in system dimensionality is preferable to strong dilution of the material (e.g. with inert, randomly distributed nanoparticles) since the former method should maintain a sufficient percolation path for charges and excitons within the conjugated material. White electroluminescence has recently been demonstrated for devices based on these nanocomposites [11], making such polymer intercalation in an inorganic matrix a promising approach towards achieving stable colour-tuning of light emitters.

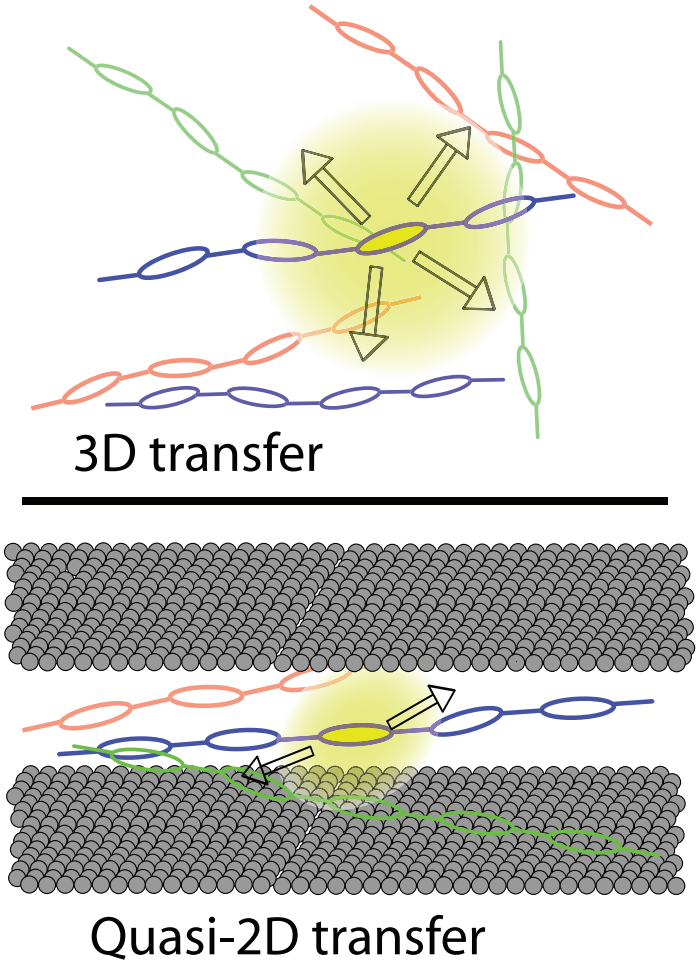

Figure 4.7: The proposed difference between three dimensional and quasi-two dimensional energy transfer is shown schematically, depicting the confinement of the polymer strands within the galleries of the SnS_2 matrix.

Chapter 5

Transient terahertz photoconductivity of Gallium Arsenide nanowires

In this chapter, the ultrafast carrier dynamics in nanostructured inorganic semiconductors are reported. Whilst in the previous chapter, the nanoscale structure was provided by self-assembly in solution, to obtain high purity inorganic nanostructures it is often preferable to use a growth technique such as metal-organic chemical vapour deposition (MOCVD). Gallium Arsenide nanowires provide an excellent model system for assessing the change in electronic dynamics upon moving from bulk to nanostructured material. In particular, the effect of a dramatic increase in surface area-to-volume ratio represents a step towards the situation required for bulk heterojunction based optoelectronics (see Section 2.3.3.2). The dominant carrier trapping mechanism was shown to be surface recombination; surface passivation of the nanowires was carried out to change the surface trap density, and a qualitative agreement between experiment and theory is shown. In order to investigate the ultrafast electronic dynamics, the technique of optical-pump terahertz-probe spectroscopy is used, as

described in Section 3.3.2.

5.1 Background

An understanding of the dynamics of charge carriers in semiconductor nanostructures is critical to the use of these materials in electronic and opto-electronic devices. In particular, semiconductor nanowires show promise as single photon detectors [125, 196], electrically-driven lasers [124], nanoscale transistors [197] and in dye-sensitised solar cells [126]. In this chapter, the conductivity of photoexcited GaAs nanowires on sub-picosecond to nanosecond timescales using terahertz spectroscopy is presented. Specifically, the transient photoconductivity of GaAs nanowires is studied using the time-resolved terahertz method introduced in Section 3.3.2. To summarise the fundamental experimental procedure of using THz-TDS to analyse carrier dynamics in semiconductors, excited species may be photoinjected into the sample using a pulse from a femtosecond laser, and the complex conductivity can be tracked using a delayed single-cycle pulse of terahertz radiation [198]. The broad bandwidth of terahertz pulses allows the characterisation of the complex conductivity of a sample across a frequency range comparable to typical plasma frequencies and momentum scattering rates in inorganic semiconductors. Recent studies of nanomaterials using THz-TDS have examined silicon micro- and nano-crystals [165, 199, 200], InP and CdSe nanoparticles [107, 167] and nanostructured ZnO [201]. The most beneficial aspect of the THz-TDS approach is that it is non-contact and therefore avoids artifacts that may arise in purely electrical measurements from difficulties in making Ohmic contacts to a nano-sized material. THz-TDS also has a range of advantages over other ultrafast techniques: for example, time-resolved photoluminescence measurements of carrier lifetimes in GaAs nanowires are hindered by a large defect density that reduces the photoluminescence efficiency [131].

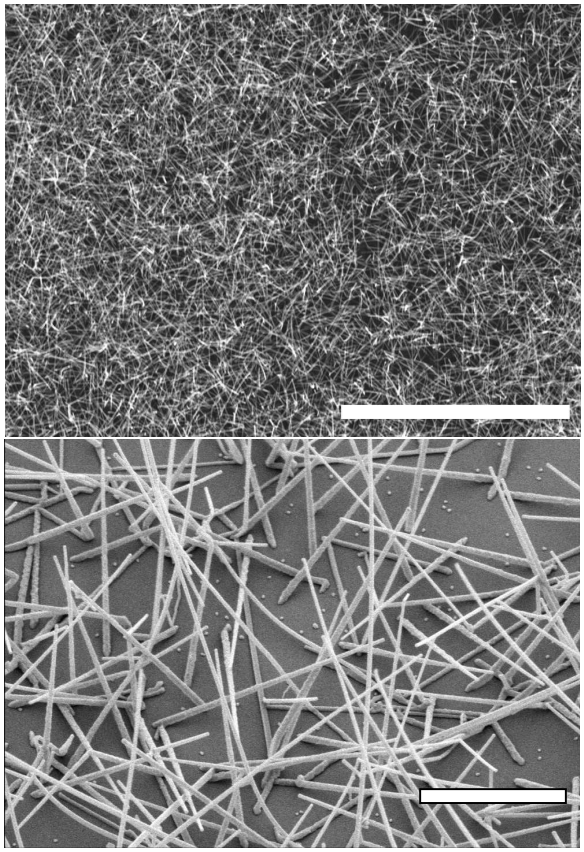

Figure 5.1: Scanning electron micrographs of GaAs nanowires on a quartz substrate. The scale bar (white) represents a) 30 μm and b) 2 μm; the images were taken at 90° and 45° to the surface respectively. The random orientation of the nanowires is caused by the lack of symmetry of the substrate.

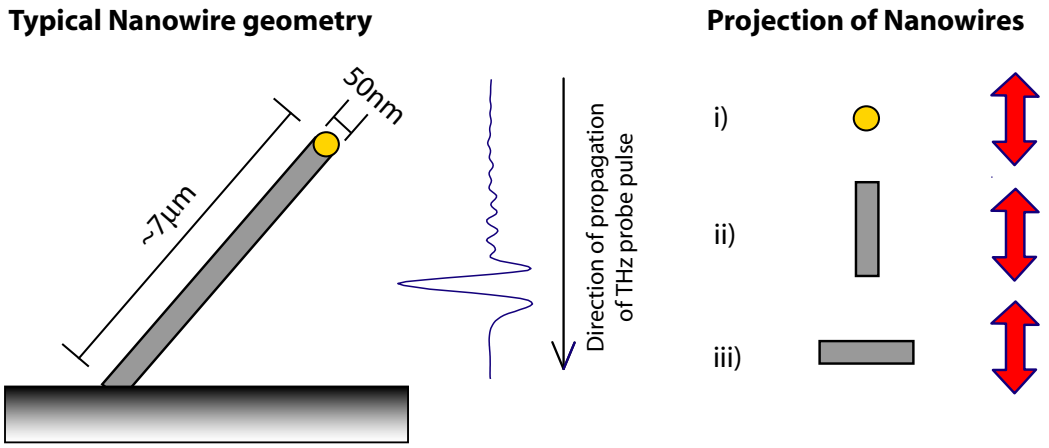

Figure 5.2: This schematic shows the typical geometry of a GaAs nanowires grown on a quartz substrate. The right hand side indicates the three orthogonal orientations of the nanowires with respect to the polarisation of the terahertz electric field T. The geometrical factor f in the surface plasmon frequency is given by i) $f = 1/3$ ii) $f = 0$ for T parallel to the axis of the nanowire, and iii) $f = 1/2$.

5.2 Sample characteristics

In this chapter the experimental samples are GaAs nanowires grown from a gold colloid seed on a z-cut quartz substrate [202][1]. The scanning electron micrograph (SEM) image of the sample (Figure 5.1) shows an isotropic array of nanowires with gold nanoparticles visible on the tips. An average areal density of ~ 3 nanowires μm^{-2}, wire length of $5-10\,\mu$m and areal fill fraction of $10\pm2\%$ was determined from multiple SEM images, with wire diameters of 50-100 nm. A typical nanowire is shown in the schematic in Figure 5.2. The dynamics of photoexcited electrons was measured by time-resolved THz-TDS, using a setup described in an earlier chapter (Section 3.3.2). Figure 5.3 shows the pump-induced change in the peak of the terahertz electric field pulse transmitted through the sample ($\Delta T/T$) as a function of time t after excitation. Over the first 5 ps, at an excitation-pulse fluence of $1.3\,\text{mJcm}^{-2}$ (squares), the nanowires exhibit a non-exponential decay in conductivity, which is proportional to the $\Delta T/T$. In comparison, bulk GaAs has a mono-exponential carrier lifetime of

[1]The samples and micrograph images in this experiment were prepared by Dr. M Gao and Prof. C Jagadish at the Australian National University, Australia.

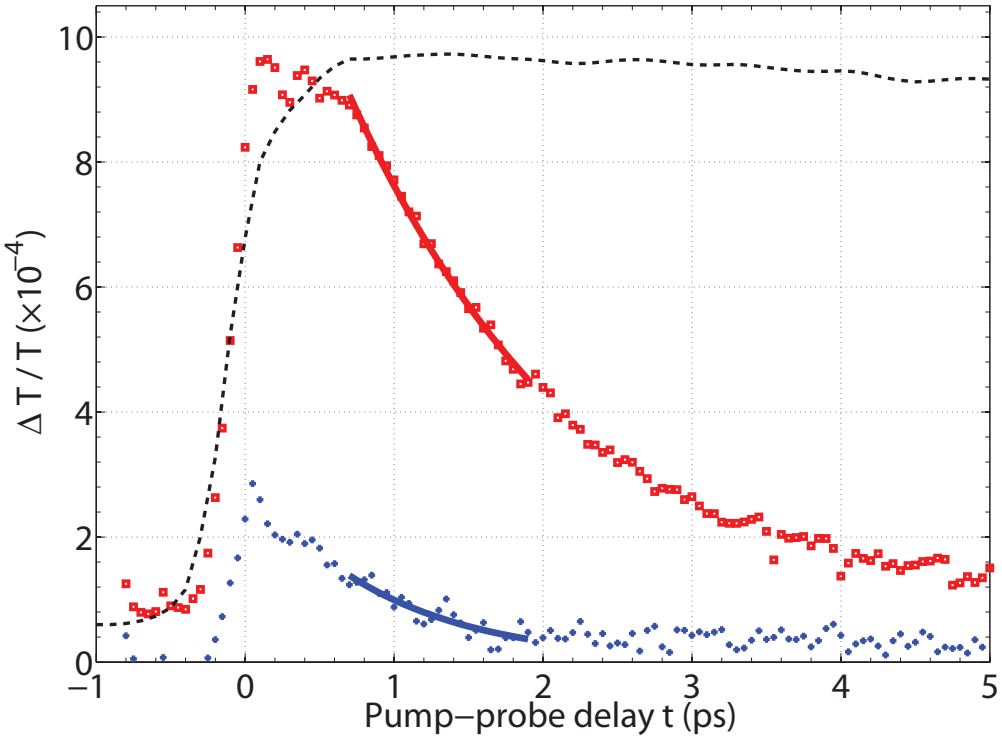

Figure 5.3: Pump-induced change in peak transmitted terahertz electric field ($\Delta T/T$) for different pump-probe delays t, for GaAs nanowires excited at 800 nm with an incident pump fluence of 44 μJcm^{-2} (red crosses) and 1.3 mJcm^{-2} (blue squares). Solid lines indicate exponential fits, used to extract conductivity decay times shown in Figure 5.8g). The dashed black line is for bulk GaAs at 1.3 mJcm^{-2} but reduced in scale by a factor of 75. A weak laser pre-pulse is responsible for the non-zero $\Delta T/T$ at $t < 0$.

$\sim$3.5 ns at the same pump fluence, as Figure 5.4 indicates. The substantially shorter conductivity dynamic for GaAs nanowires is a consequence of carrier trapping at surface defects, and underlines their potential for use in ultra-fast nano-scale opto-electronic devices. The shape of the decay in $\Delta T/T$ alters with the pump fluence, tending to a faster, mono-exponential conductivity decay at lower pump fluence, as illustrated for 44 μJcm^{-2} in Figure 5.3 (circles). This effect results from surface trap saturation, as discussed in more detail below.

By fixing the pump-probe delay t and recording the change in terahertz transmis-

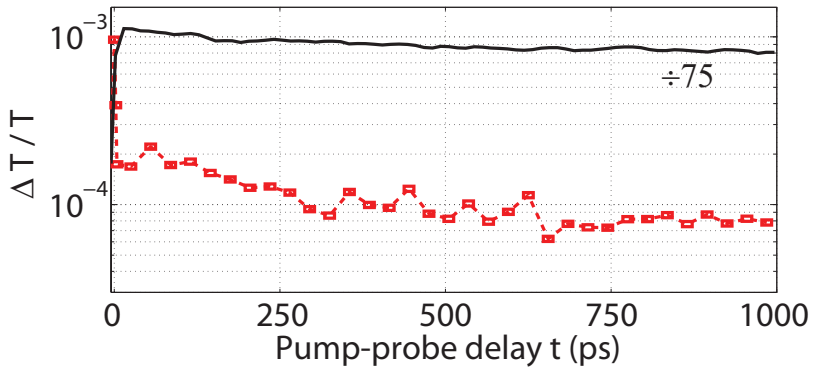

Figure 5.4: $\Delta T/T$ up to $t = 1\,\text{ns}$ for the nanowires (squares) and bulk GaAs (black line, $\div 75$) at the higher ($1.3\,\text{mJcm}^{-2}$) pump fluence. In both cases $\Delta T/T$ exhibits a slow exponential decay with $\tau > 1\,\text{ns}$ at long delay times.

sion, the frequency-dependence of the photoinduced conductivity $\Delta\sigma(\omega, t)$ of GaAs nanowires was determined, providing a time-resolved monitor of quasiparticle dynamics in the material. An expression derived from standard thin-film optics was used to obtain $\Delta\sigma(\omega, t)$ from $\Delta T(\omega, t)/T(\omega, t)$, as explained in Appendix A. Figure 5.5 shows the extracted complex conductivity, at several early pump delay times after the photoinjection of carriers. Here, the real part of $\Delta\sigma(\omega, t)$ may be thought of as the resistive response of the nanowires, with the imaginary part being associated with an additional capacitive or inductive response. During the first 200 fs after excitation the real part of the conductivity is positive and has no discernible frequency dependence (Figure 5.5a). This indicates the presence of photogenerated free carriers with a large scattering rate. However, over the next 300 fs a peak appears in the real part of the conductivity (Figure 5.5a), accompanied by a corresponding zero crossing in the imaginary part (Figure 5.5b). The frequency of this feature decreases with delay time t, and it is therefore attributed to a carrier-density dependent mode such as a localised surface plasmon (LSP) [203], rather than an excitonic transition [171, 204]. At later times $t > 2\,\text{ps}$, this resonance has shifted below the frequency resolution of the system, returning to a free-carrier type response at the longest delay accessible using the current experimental setup (1 ns – not shown).

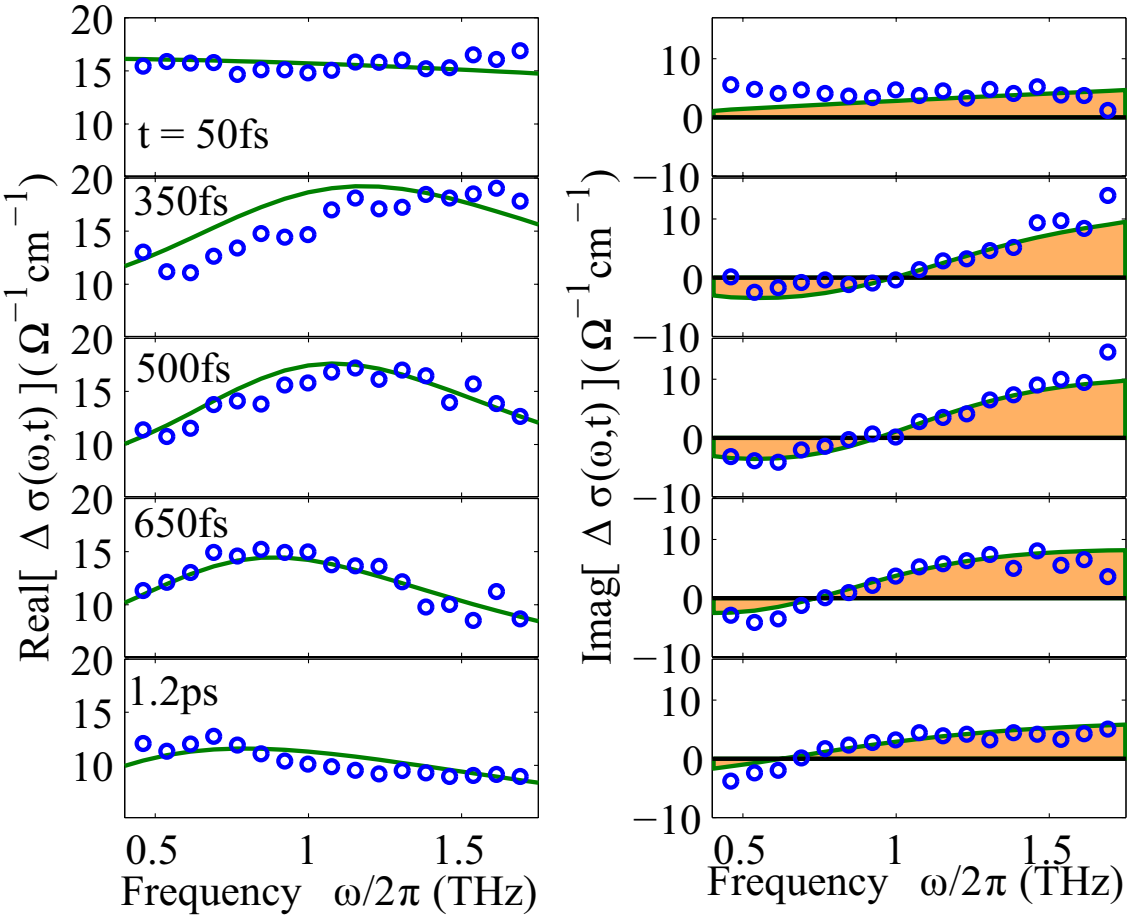

Figure 5.5: Time-resolved conductivity of photoexcited electrons, and the carrier density and scattering rate extracted from the plasmon model described in the text. The a) real and b) imaginary components of the conductivity are given at a series of pump-probe delay times, for an incident pump pulse fluence of 1.3 mJcm^{-2}. The circles are the raw data and the lines are fits including both plasmon and plasma responses. The parameters extracted from these fits are shown in Figure 5.6.

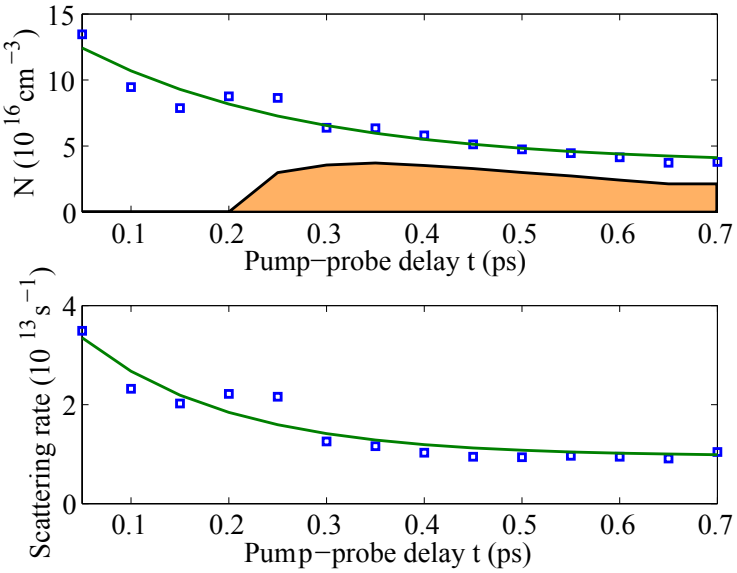

Figure 5.6: Figure a) gives the total carrier density $N_{\text{plasmon}} + N_{\text{plasma}}$ (squares), with an exponential fit (green line) with time constant 270 fs drawn as a guide to the eye. The filled area is the carrier density N_{plasmon} contributing to the plasmonic response. Figure b) shows the scattering rate (squares), with an exponential decay (solid line) with time constant 178 fs.

5.3 Discussion

Numerous models of features in $\Delta\sigma(\omega, t)$ have been proposed, including: localised surface plasmon (LSP) modes [165], transitions between excitonic states [171] and the Drude-Smith model, which introduces a further parameter c_n related to incomplete randomisation of carrier momentum upon scattering [168]. While the Drude-Smith model can produce comparable shapes of the frequency-dependent conductivity to the surface plasmon model (when $c_1 \sim -1$, $c_{n>1} = 0$), it would require a time-varying backscattering parameter to model the data, which has no obvious physical origin. By utilising the surface plasmon approach to model the conductivity, a sound physical basis for the observed conductivity is provided. Terahertz radiation can couple into the (normally forbidden) plasmon mode due to the narrow width (50 nm) of the nanowires, and the interaction between the modes on adjacent sides of the same nanowire [203]. The emergence of collective modes such as LSPs is expected

to occur for nanoparticles, where the carrier dynamics are dominated by surface effects [165, 205].

LSP modes are coherent oscillations of the electron-hole plasma, modified from the bulk plasma frequency by the interaction with the plasma/dielectric surface interface. The relationship between the carrier density N and the plasmon frequency ω_{pl} is given by $\omega_{\mathrm{pl}}^2 = (fNe^2)/\epsilon_0\epsilon_\infty m^*$. Here, m^* is the effective electron mass, ϵ_∞ the high-frequency dielectric response of the nanowires, and f is a factor dependent upon the surface geometry and the surrounding dielectric medium [136]. For a terahertz electric field T polarised perpendicular to the axis of a cylindrical nanowire in vacuum, $f = 1/2$ or $f = 1/3$ (see the schematic in Figure 5.2), while for T parallel to the nanowire's axis, $f = 0$, and the only conductivity response is due to the bulk plasma mode. The complex conductivity of a free-electron plasma with a plasmon resonance is given within the Drude framework by [165]

$$\sigma(\omega) = \frac{iNe^2\omega}{m^*\left(\omega^2 - \omega_{\mathrm{pl}}^2 + i\omega\gamma\right)}, \tag{5.1}$$

where ω_{pl} is the plasmon frequency (determined by the relationship given above) and γ is the momentum scattering rate. For an ensemble of nanowires oriented at random angles a contribution to the photoinduced conductivity will be dominated by two different modes: a plasmon at ω_{pl} and the bulk plasma at $\omega_{\mathrm{pl}} = 0$. In order to model the measured $\Delta\sigma(\omega, t)$ these two contributions to the conductivity of the form given in Equation 5.1, one with a carrier density N_{bulk} and $f = 0$ for the bulk mode and another with carrier density N_{plasmon} and $f = 1/2$ (as the $f = 1/3$ mode presents negligible surface area) are added together. The scattering rate γ is assumed to be the same for both modes. Excellent fits to the measured data are obtained over the full range of pump-probe delays t, as indicated by the solid lines in Figure 5.5. The carrier densities and scattering rates extracted are shown as a function of pump-probe delay in Figure 5.6a) and b) respectively. While the carrier density in the bulk-like

mode is observed to form rapidly, that in the plasmon mode has only built up after 300 fs. In bulk GaAs, the free-electron plasma response develops over a timescale comparable with the inverse of the plasma frequency [206]. The plasmon frequency is lower than that of the plasma, consistent with the observed longer formation time for the nanowires. In Figure 5.6b) the scattering rate can be seen to decrease initially with t, before remaining roughly constant at $10^{13}\,\mathrm{s}^{-1}$ for $t > 400\,\mathrm{fs}$. From the extracted scattering rates it is possible to determine the charge carrier mobility μ in the long-time limit within the Drude model ($\mu = em^{*-1}\gamma^{-1}$) to be $2600\,\mathrm{cm^2V^{-1}s^{-1}}$. Remarkably, this value is only a factor of three lower than typical electron mobilities in bulk GaAs at room temperature($\sim$8000 $\mathrm{cm^2V^{-1}s^{-1}}$) [163], high-lighting the prospect of implementation of these structures in fast nanoscale electronics and optoelectronics.

5.3.1 Pump fluence dependence of conductivity

The observed drop in the carrier density with time is indicative of the ultrafast trapping or decay of the surface carrier population. An experiment using a fixed pump-probe delay ($t = 550\,\mathrm{fs}$) and a range of incident pump fluences F was carried out to allow comparison between plasmon frequencies ω_{pl} deduced from experiment with those anticipated assuming linearity between the pump fluence and photoexcited carrier density. The plasma frequencies extracted from fits to the conductivity spectra (Figure 5.8a-e) using the previously discussed model are plotted in Figure 5.8f) as a function of pump fluence. While the plasmon frequency increases with pump fluence, it does not scale according to $\omega_{\mathrm{pl}} \propto \sqrt{F} \propto \sqrt{N}$. This suggests that the photoexcited carrier density in the first 550 fs is non-linear with respect to fluence. Such behaviour may be expected, due to either band-filling or ultrafast trapping and trap-state filling within the first 550 fs and the subsequent effect upon carrier numbers that are able to take part in the collective surface mode.

Since surface trapping strongly affects the carrier lifetime, it is essential to obtain

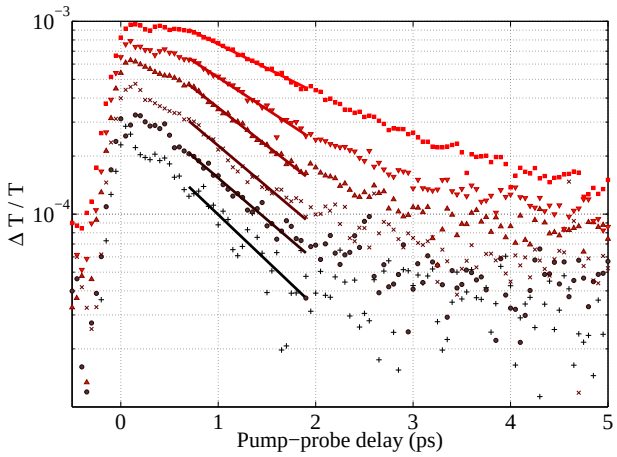

Figure 5.7: The pump-induced change in terahertz transmission is shown for a range of incident pump fluences (from a low of 0.05 mJcm^{-2} to a high of 1.1 mJcm^{-2}). A single mono-exponential fit is shown (solid lines) between 0.8 and 1.8 ps, providing a good fit over this time range.

an estimate of the surface trap density in order to calculate the carrier density at which saturation has an effect. To investigate this behaviour, mono-exponential curves were fitted to a range of pump-probe scans over the time window $t = 0.8 - 1.8$ ps (see Figure 5.7) with the resulting decay times shown in Figure 5.8g). A clear dependence of the carrier relaxation time on pump fluence can be seen, with a doubling in the trapping time τ when the incident pump fluence is increased 30-fold. As the mobility remains constant over the examined time interval, this change is primarily due to saturation of the surface traps by the large photoinduced carrier population, leading to a reduction in available trap states with increasing pump fluence. For a more quantitative analysis, these data were fitted with the numerical solution of a rate equation for carrier trapping [200] that included a finite number of available traps and yielded a trap density of $N_{\text{traps}} = 2 \times 10^{17}\,\text{cm}^{-3}$ and a trapping cross-section of $6 \times 10^{-14}\,\text{cm}^2$ (solid line in Figure 5.8g). The extracted trap density is comparable to the initial photoinjected carrier density, explaining the distinct change in carrier lifetime with pump-fluence as the carrier density passes this mark.

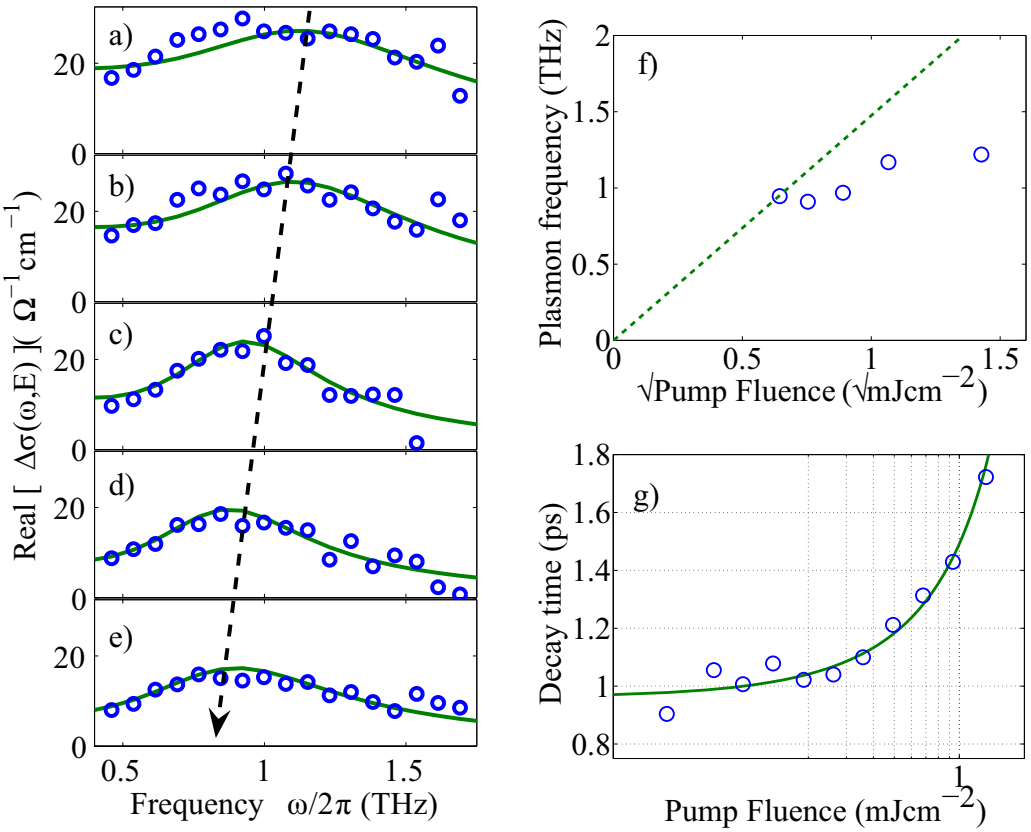

Figure 5.8: Pump-fluence dependence of terahertz conductivity at a pump-probe delay t=550 fs. Real part of photoinduced conductivity after excitation with various pump energies: a) 2 mJcm^{-2}, b) 1.1 mJcm^{-2}, c) 0.79 mJcm^{-2}, d) 0.57 mJcm^{-2} and e) 0.42 mJcm^{-2}, where points are raw data, and solid lines are from the model described in the text. Figure f) shows the extracted plasmon frequency ω_{pl} as a function of pump fluence F (circles) in comparison with a prediction from $\omega_{\mathrm{pl}} \propto \sqrt{F} \propto \sqrt{N}$. Figure g) gives the lifetime of the conductivity as a function of incident pump fluence extracted from exponential fits to a series of pump-probe delay scans. The rate equation model described in the text (solid line) accurately reproduces the fluence-dependence of the carrier lifetime.

5.4 Surface Passivation

The surface trap states in inorganic semiconductors are well studied, and the behaviour of devices based upon GaAs has been improved by chemical treatments that remove the surface layer and passivate the interface, such as bipolar transistors [207] and photoconductive antennas [133]. Passivation is understood to prevent surface atoms forming defect states within the band gap, which in turn reduces the surface recombination rate; an in depth investigation of the mechanism behind the electronic effect of surface passivation is beyond the scope of this work – an interested reader can find more information in good reviews of this area [130, 208]. Assuming the carrier velocity and trap scattering cross-section remain unchanged, surface passivation can be understood to change only the surface trap density and surface recombination velocity. Terahertz measurements of carrier lifetime in bulk GaAs have shown as large as a 17% reduction in surface trap density by etching and passivation with Ammonium Sulfate [133], however, to date there have been no similar measurements for nanostructured GaAs. In this section, the effect of surface passivation upon the physical structure, and the carrier lifetime (and hence trap density) of the nanowires are investigated.

5.4.1 Etch and passivation protocol

The purpose of etching before the passivation step is to remove the surface oxide layer. Ammonium Sulfate ($(NH_4)_2S$) is also weakly acidic, and will etch the surface layers of GaAs, albeit at a slow rate. Three samples were prepared from nanowires grown during a single run – a reference unpassivated sample, nanowires passivated in a 2 vol% aqueous solution of Ammonium Sulfate (for 10 minutes), and a sample etched in a 4 vol% solution of Hydrochloric Acid (HCl) in distilled water (for ∼2 seconds) before the passivation step. After passivation or etching, the sample was

washed immediately in distilled water before being dried in a steady nitrogen gas flow. The optical-pump terahertz-probe spectroscopy of the samples were measured under vacuum, however, the samples were stored in air between measurements to investigate the effect of de-passivation.

High-resolution SEM images of the three samples are shown in Figure 5.9[2]. Little difference can be seen between the reference and passivated samples, however, a large change in sample morphology occurs during the etching process. Even at the low etchant concentration and exposure times given above, it appears that etching removes the nanowires from the surface of the sample. As will be shown, this has little effect upon the terahertz photoconductivity of the sample, indicating that the nanowires remain on the substrate but now lie in the plane of the substrate (as can be seen faintly in Figure 5.9c). This may have the effect of leading to a stronger interaction with the terahertz probe, due to the elimination of the "type i" nanowires depicted in Figure 5.2. For this reason, the carrier lifetime rather than the peak photoconductivity value is used as an indication of trap density for the remainder of this section. More research is currently being undertaken to optimise the etching and passivation protocol.

5.4.2 Carrier lifetime

The time-resolved photoconductivity of the reference and the passivated sample are shown in Figure 5.10. The effect of passivation has been reported to lead to both a large increase in peak photoconductivity and an extension in carrier lifetime [133], and both effects are observed in this system. However, here the effects appear small, with only a marginal increase in lifetime or peak signal observed. This may well be a result of bypassing the etching step, and a large proportion of the surface is likely to remain oxidised. To allow comparison to the data shown in Figure 5.8g), a

[2]The SEM images were prepared by Dr. M Gao of the Australian National University, Canberra.

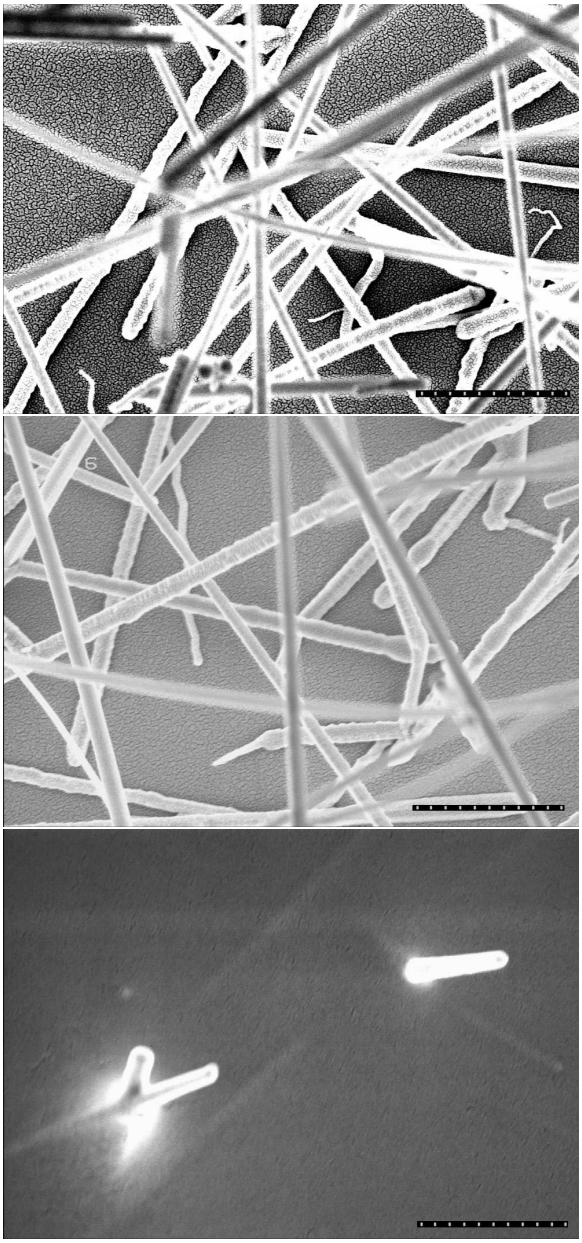

Figure 5.9: A series of high-resolution SEM images of the a) reference nanowires before treatment, b) passivated nanowires, before etching and c) etched and passivated nanowires. The scale bar represents 1 μm, and the micrographs were taken at 45° to the sample normal. Many fewer nanowires are visible after etching than in the unetched cases. However, several faint nanowire shapes are visible in the background showing it is possible that the nanowires were weakened by the etching process leading to mechanical instability, and may remain on the quartz substrate.

pump-fluence dependence experiment was carried out over a large range. Figure 5.11 shows the extracted mono-exponential decay constant as measured between 1.6 and 6 ps after photoexcitation. The dashed lines are a fit to a simplification of the model for carrier lifetime shown in Reference [200] and used earlier, where

$$\tau_{\mathrm{trap}} = \frac{\tau_{\mathrm{trap0}}}{1 - N/N_{\mathrm{trap}}}. \tag{5.2}$$

Here, τ_{trap0} is the carrier lifetime at negligible photoinjected carrier density, such that the traps act independently of fluence, N is the photoexcitation density and N_{trap} is the trap density. This equation is valid in the carrier density regime *below* trap saturation – since the lifetime in bulk GaAs is of the order of 3 ns and the maximum carrier lifetime seen here is 12 ps, this restriction is satisfied. While this is a rather crude model (it does not take variation in the surface recombination velocity into account, which is known to change upon passivation), it does qualitatively reproduce the carrier lifetime in Figure 5.11, providing values of N_{trap} of between 8×10^{18} and $11 \times 10^{18}\,\mathrm{cm}^{-3}$. These values are significantly larger than those seen in the earlier experiments; this may be accounted for by the use of a more simple model, or variation between sample growth runs or in storage conditions. Regardless, a trend towards lower surface trap density is observed upon surface passivation, and a 28% increase in carrier lifetime is seen in the etched and passivation case.

5.4.3 Stability of surface passivation

Sulphur passivation of GaAs is known to be partially unstable in oxygen, as previously noted in References [133] and [132]. In order to test the effect of de-passivation in the nanowires sample, an additional sample was prepared by passivating (without the etching step). The carrier lifetime was measured (at fixed incident fluence of $56\,\mathrm{mJcm}^{-2}$) over several days. The sample was stored in air between measurements, to

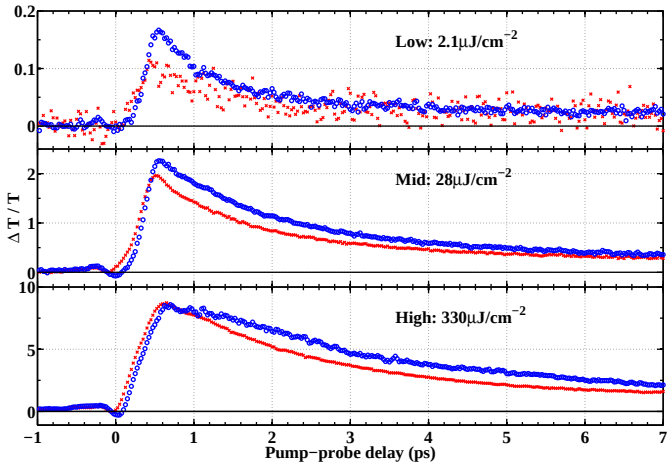

Figure 5.10: The time-resolved photoconductivity of pre- and post-treatment nanowires is shown (red crosses and blue circles, respectively) for three different photoexcitation fluences. The passivated sample has a consistently higher peak conductivity, and slower carrier decay for all fluences shown.

allow oxidation and de-passivation. Figure 5.12 shows the results of this experiment; an initial rise in carrier lifetime is seen due to the passivation process (as expected), followed by a return towards the unpassivated value over the next 17 days. The de-passivation timescale is similar to that previously seen in the literature.

5.5 Summary

In summary, the work reported in this chapter involves measuring the transient terahertz conductivity of GaAs nanowires on sub-picosecond to nanosecond timescales using a non-contact optical probe based on time-domain spectroscopy. The observed conductivity dynamics differ strongly from those for bulk GaAs, displaying ultra-short ($\sim$1 ps) lifetimes that depend critically on the trap density at the nanowire surface. These results open the possibility for implementation of these nanowires in ultra-fast switching devices, whose properties can be optimised through a multitude of mechanisms such as overcoating the nanowires with a higher band-gap material [131, 209]

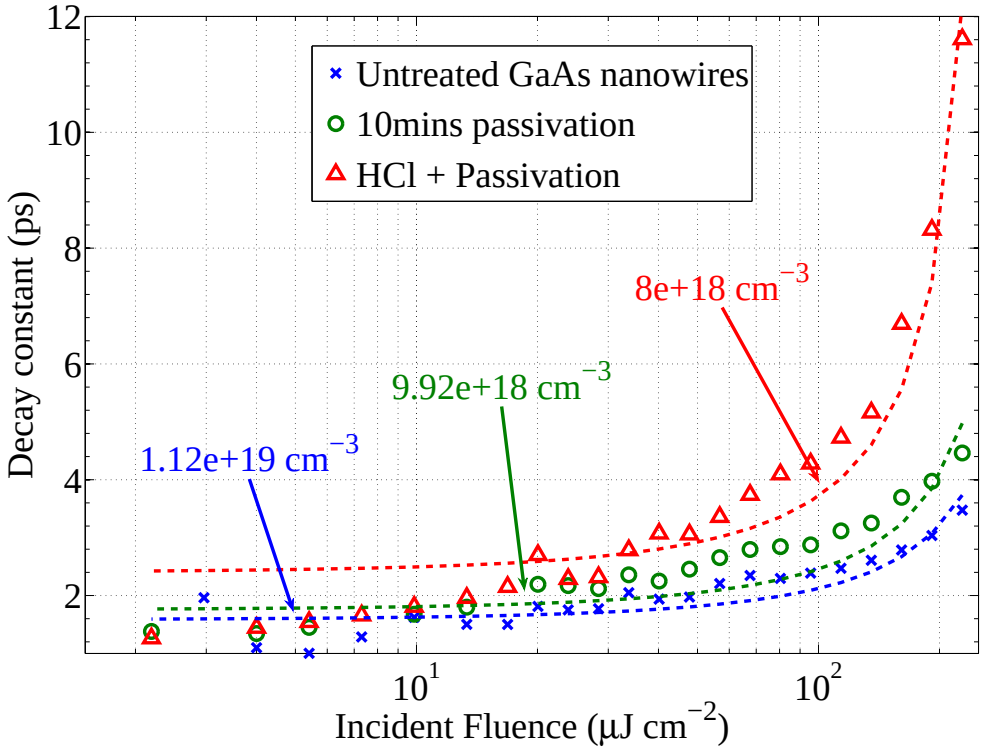

Figure 5.11: A monoexponential decay constant was fitted to the time-resolved photoinduced conductivity measurements for all three samples. The solid lines are a fit as described in the text, and the labels give the calculated surface trap density for the three samples.

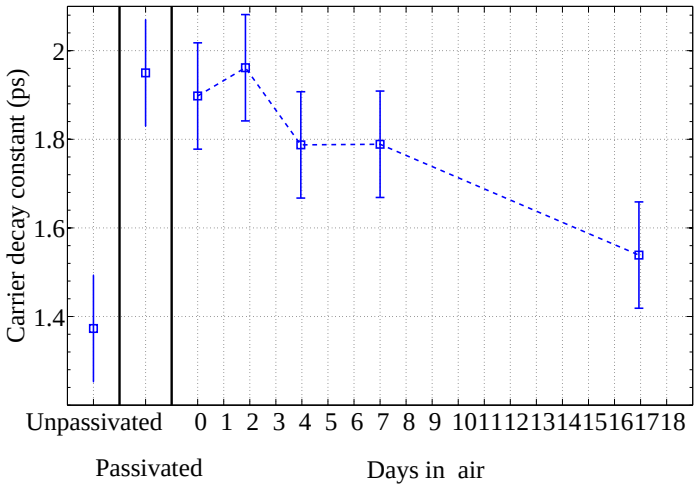

Figure 5.12: The monoexponential decay constant is shown for a second sample, before and after treatment and after several hours stored in air. A slow return toward the unpassivated state is seen, however, after 168 hours the carrier lifetime remains around 10% longer than in the unpassivated case. The error bars represented the uncertainty in the value of the carrier decay constant.

or chemical passivation of surface defects [133]. A preliminary study of the effects of surface passivation was carried out, and whilst a qualitative decrease in surface trap density was noted for passivated samples, optimisation of the passivation protocol is required before a in-depth study is possible. The electron mobility for the nanowires at room temperature was extracted from the data by modelling of the plasmon resonance that forms within the first 300 fs after excitation. The resulting value of 2600 $\mathrm{cm^2V^{-1}s^{-1}}$ is only a factor of three lower than that typical for bulk GaAs, demonstrating that high-quality epitaxial growth can generate nanowires with excellent electronic properties.

Chapter 6

Sub-gap optical-pump terahertz-probe studies of Polymer:Fullerene blends

In this chapter, the time-resolved photoconductivity of polymer-fullerene bulk heterojunctions is investigated. As stated in Section 2.3.3.2, photovoltaic cells incorporating a large-area heterojunction formed between an organic polymer and an electron acceptor have shown solar to electric power conversion efficiencies of up to 4–6%, and represent a promising technology for future power generation [89, 92]. It is known that the interface not only provides an energetically favourable exciton dissociation site, but also allows excitation states to exist that do not occur in either bulk component [88]. Some of the highest photovoltaic charge generation efficiencies measured have been produced by blending organic semiconductors such as P3HT [poly(3-hexylthiophene)] or a PPV [poly(phenylenevinylene)] derivative with PCBM (a methanofullerene), and this chapter investigates the terahertz-frequency photoconductivity in these systems. By measuring the photoconductivity for both above- and below-gap excitation, a surprisingly high charge generation efficiency is noted for sub-gap excitation [210].

The advantages of the non-contact terahertz measurements are again noted, allowing simple measurements to be made of nanoscale properties.

6.1 Background: Organic photovoltaics

Polymer-fullerene blends have attracted considerable interest because they are very easy to process from solution, making roll-to-roll production of flexible photovoltaics a possibility [83–85, 91, 100, 211]. The primary characteristics required of high efficiency photovoltaics include: an absorption spectrum that provides a good overlap with the solar spectrum, and a balance between DC voltage and harvesting light, fast electron transfer from charge donor to acceptor, a high photon to charge carrier branching efficiency, and high carrier mobility. It is well known that many factors influence the efficiency of these devices, for example, chain arrangement in the solid [212], polymer regio-regularity [100], the ratio of polymer to charge acceptor [112], and post-process thermal annealing [78, 91]. Therefore, for the optimisation of photovoltaic device efficiencies a detailed knowledge of the mechanisms of charge generation and subsequent motion through the material is essential.

A number of studies have attempted to identify the microscopic origin and cause of charge generation and charge carrier mobility in organic semiconductors [106, 110, 111, 113, 117, 157, 213–219]. Relatively large carrier mobilities have been proposed, however, there has been disagreement in the literature caused partly by differences between the experimental methods used to investigate carrier dynamics. Measurements carried out on photovoltaic devices, whilst revealing the real-world behaviour of the materials, suffer from difficulties in interpretation arising from the presence of an interface between the electrodes and the polymer [220]. Non-contact measurements, including transient absorption [215, 219], photoluminescence up-conversion [86, 214, 221], time-resolved microwave-conductivity [106, 110, 111,

213, 218] and terahertz time-domain-spectroscopy [112–115, 117, 157, 216, 217] have also been used to great effect. A range of values for high-frequency electron and hole mobility from $10^{-5}\,\mathrm{cm^2V^{-1}s^{-1}}$ to over $600\,\mathrm{cm^2V^{-1}s^{-1}}$ have been proposed for a variety of conjugated polymers; such a large degree of variation suggests that results are very sensitive to both experimental technique and the models used in the analysis [96, 106].

In this chapter, two time-resolved optical-pump terahertz-probe (OPTP) spectrometers have been used to observe the fluence and wavelength dependence of charge generation and carrier mobility in neat and PCBM-blended organic polymer films, as described in Section 3.3.2. Using this approach the complex photoconductivity of two state-of-the-art organic photovoltaic materials was measured, thin films of either P3HT or poly[2-methoxy-5-(3,7-dimethyloctyloxy)-1,4-phenylenevinylene] (MDMO-PPV) blended with PCBM. This study examines the dependence of the photoinduced conductivity on time after excitation, frequency of the driving terahertz radiation, and excitation fluence and wavelength. In later sections, attention is paid to the implications of these results for photogeneration efficiencies, carrier mobilities and lifetimes and find qualitatively similar results for both polymers investigated.

The OPTP measurements of organic semiconductors reported to date have employed pulsed laser amplifier systems, resulting in high excitation fluences of up to $6\,\mathrm{mJ\,cm^{-2}}$. This approach produces carrier densities in the region of $10^{21}\,\mathrm{cm^{-3}}$, however, second-order effects such as bimolecular excitonic or charge annihilation have been shown to occur at carrier densities as low as $10^{16}\,\mathrm{cm^{-3}}$ [111]. In addition, this process inevitably leads to excitation fluences that are many orders of magnitude above those typically encountered under natural conditions such as sunlight. Conclusions drawn from such experiments may therefore have limited applicability to material performance in a typical device structure. This has been circumvented by utilising a low-fluence, high-repetition rate system, which allows observation of the photoin-

duced conductivity changes for excitation fluences as low as $24\,\mathrm{nJ\,cm^{-2}}$ with a good signal-to-noise ratio. In combination with the results derived from an amplifier-based OPTP system, this allows an examination of the photoinduced terahertz conductivity for excitation fluences ranging over more than four orders of magnitude.

A further difficulty encountered with OPTP measurements has been the use of polymer films that are thick in comparison with the absorption depth at optical pump wavelengths, to maximise the absorbed photon fluence and the resulting signal-to-noise ratio [112, 216]. However, this practise leads to an exponential distribution of carriers in the direction of terahertz propagation, which complicates the data analysis and extraction of the photoconductivity [117, 162]. In the experimental study reported here, I have taken a different approach by exciting with photons of low energy, i.e. significantly below the peak of the $\pi - \pi^*$ transition of both polymers. Under these conditions a uniformly distributed density of photoexcitations is created, whose spectral and temporal OPTP response is remarkably similar to that of charges generated using excitation near the absorption peak. The observation of a low-energy feature in absorption and photoluminescence measurements has recently led to the suggestion that such low-energy photons may create a weakly bound polaron pair formed between the highest occupied molecular orbital (HOMO) of the polymer and the lowest unoccupied molecular orbital (LUMO) of the PCBM [87]. The measurements presented here reveal a surprisingly high photoconductivity upon excitation of this low-energy feature, suggesting that the polaron pair may offer an efficient direct route to photoexcitation of charges in the polymer blends, in agreement with recent conclusions by Benson-Smith *et al.* [88].

6.2 Sample preparation

P3HT (M_w=28000 g/mol, >95% regio-regularity), MDMO-PPV (M_w=718000 g/mol) and PCBM were purchased from *American Dye Source* and used without further purification. The chemical structures of all components can be found at the top of Figure 6.1. Each material was separately dissolved in dichlorobenzene at a concentration of 15 gl^{-1} and polymer-fullerene blends were derived by mixing the relevant solutions at a 1:1 ratio by volume. To produce films, the solutions were spun-cast or drop-cast onto z-cut quartz substrates for optical density measurements or terahertz measurements, respectively. Thick (d ~10 μm) drop-cast samples were required for the terahertz measurements to ensure sufficiently high photoinduced conductivity for the case when the absorption coefficent and the photon to charge branching ratio was small (e.g. for the neat unblended samples). All samples were dried and annealed at 100 °C for 3 hours. Materials were handled and samples were prepared in an inert (N_2) atmosphere. Thin-film transmission measurements were performed using a spectrophotometer (Perkin-Elmer Lambda 9), and the film thickness was measured using a step-profilometer (Veeko DekTak 7).

Optical-pump terahertz-probe measurements were taken using two different terahertz spectrometers. The high-fluence spectrometer used a regenerative amplifier (800 nm centre wavelength, 1kHz repetition rate, 50 fs pulse duration, 1 mJ pulse energy). The terahertz probe was generated through optical rectification in a 2mm-thick ZnTe crystal, and detected using electro-optic sampling in a 1mm-thick ZnTe crystal. Photoexcitation of the sample was carried out either using up to 500 μJ/pulse of the 800 nm fundamental, or the output from a *TOPAS* optical parametric amplifier, providing around 30 μJ/pulse at 560 nm. To measure the low-fluence photoconductivity, a Ti:Sapphire laser oscillator (800 nm centre wavelength, 80 MHz repetition rate, 100 fs pulse duration, 12 nJ pulse energy) was used both to photoexcite the sample and to generate and measure the terahertz probe. The terahertz probe was

System	λ (nm)	**Rep. Rate** Hz (period)	**Power** min/max (W/cm^2)	**Energy/pulse** min/max (μJ/cm^2)
Amplifier	800	1000Hz (1 ms)	0.065/0.425	65/425
	560	1000Hz (1 ms)	0.075	210
Oscillator	800	80MHz (12.5 ns)	1.9/51.2	0.024/0.642

Table 6.1: A summary of the OPTP spectrometer systems used in this study. In particular, note the short inter-pulse period with the oscillator system. The sharp increase in incident power using the oscillator system arose from a tighter focus of both pump and probe beams made possible by a four focusing mirror arrangement, as opposed to the three mirror arrangement in the amplifier system (see Section 3.3.2 for more details).

generated in a biased photoconductive switch, and measured using electro-optic sampling in a 2mm-thick ZnTe crystal – full details of this set-up are provided in Reference [133]. All measurements were made under vacuum ($< 10^{-3}$ mbar) to minimise photo-oxidisation; no sample degradation was seen during these experiments. A summary of the photoexcitation sources used is given in Table 6.1.

To recap upon Section 3.3.2, in an optical-pump terahertz-probe experiment the photoinduced change in the transmitted terahertz electric field amplitude, $\Delta T/T$, is measured also as a function of pump-probe delay. The following relatively simple calculation derived from thin-film optics allows reconstruction of the photoinduced change in sample conductivity $\Delta\sigma$ from this change in transmission $\Delta T/T$, only requiring knowledge of the excited sample thickness d and the substrate refractive index n:[160]

$$\Delta\sigma = \frac{1+n}{Z_0 d}\left(\frac{1}{1+\Delta T/T} - 1\right), \tag{6.1}$$

where Z_0 is the impedance of free space. For excitation at 800 nm, a uniform distribution along the sample depth is created and d represents the film thickness. For excitation at 560 nm, a uniformly excited block, as thick as the penetration depth d, was assumed to exist upon an unexcited P3HT substrate of refractive index n=3.23 in the THz region [222, 223]. For ease of examination, the experimental results shown throughout this chapter were converted from the measured $\Delta T/T$ to pho-

toinduced conductivity units. Both of the principal modes of operation of a optical-pump terahertz-probe experiment were employed for the measurements; in the following these are referred to as *fixed-gate* and *fixed-pump* mode. For the fixed-gate mode, the photoinduced change in peak terahertz transmission, which is related to the frequency-averaged photoinduced conductivity of the sample, is measured as a function of pump-probe delay. The resulting data are measures of the transient conductivity as a function of time after excitation and may yield information on free carrier lifetimes and the evolution of the charge mobility. Additional information can be extracted through operating the experiment in fixed-pump mode – here, the photoinduced change in terahertz time-domain electric field is measured at a fixed pump-delay. From this measurement, the real and imaginary parts of the photoconductivity spectrum across the terahertz range can be determined for a set time after excitation of the sample.

Figure 6.1 shows the thin-film absorbance spectra for neat and PCBM-blended P3HT and MDMO-PPV. For both polymers, the addition of PCBM introduces a characteristic absorption at 340 nm. In the present chapter, I will distinguish between photoexcitation with energy above and below the polymer absorption on-set as *above-gap* and *below-gap*, respectively. Knowledge of the absorption depth coupled with the incident optical-pump fluence and sample thickness permits calculation of the initial photoexcitation density. However, at the low-energy tail of the displayed spectra the measured non-zero absorbance is most likely dominated by the effect of scattering from the film, rather than electronic transitions in the material. Recent results using this technique have demonstrated the existence of a sub-gap absorption feature near 800 nm for P3HT:PCBM blends [87]. In order to obtain a correct measure of the photoinduced excitation density for the study presented here, the thin-film absorbance measurements shown in Figure 6.1 were used for above-gap excitation, while for below-gap excitation the absorbance was derived from the Photothermal

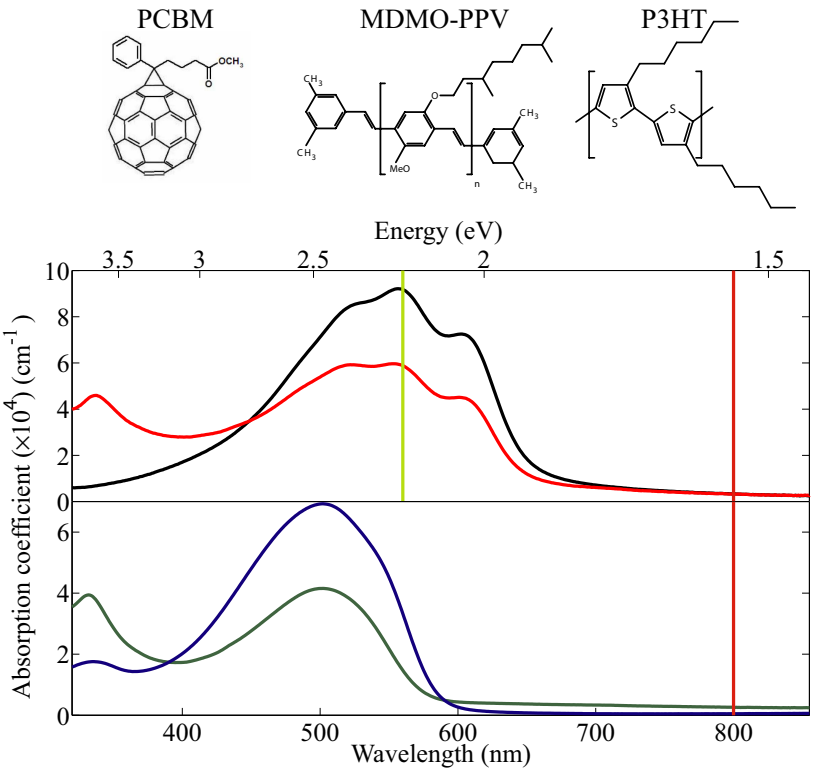

Figure 6.1: Absorption spectra for thin films of a) neat P3HT (black line) and the P3HT:PCBM blend (red line) and b) MDMO-PPV (blue line) and the MDMO-PPV:PCBM blend (green line). Vertical lines mark the centre wavelengths of the excitation used in the experiments – 560 nm and 800 nm. The chemical structures of the materials used are displayed at the top of the figure.

Deflection spectroscopy measurements of Reference [87]. The reported absorption coefficient at 800 nm was 10 cm^{-1} for P3HT, 200 cm^{-1} for P3HT:PCBM, 2 cm^{-1} for MDMO-PPV and 180 cm^{-1} for MDMO:PCBM [87].

6.3 Experimental Results

Figure 6.2 shows the time-resolved conductivity of both P3HT and P3HT:PCBM blends after photoexcitation at 800 nm, extracted using the fixed-gate method. These curves were obtained by using the high-fluence, low repetition rate system. Both samples show a sharp rise in photoinduced conductivity immediately after excitation,

starting from a value near zero. These curves demonstrate that for both samples, the lifetime of photoexcitations in the material is significantly shorter than the inter-pulse separation (1 ms), and that at these photon fluences photoconductivity arises within the temporal resolution of the system (∼300 fs).

The initial amplitude of the photoinduced conductivity is surprisingly similar for both materials given that one might expect the presence of the electron acceptor PCBM to enhance the generation of charges in the polymer considerably. Comparable observations have been made by other groups using high excitation fluences but exciting nearer the peak of the polymer absorption spectrum. Ai *et al.* [112] found initial photoinduced THz-conductivities that were within an order of magnitude for a range of P3HT:PCBM films with PCBM content varying between 0 and 80% by weight, while Hendry *et al.* [162] observed the initial photoconductivity of a PPV derivative blended with 50% PCBM to be approximately six times larger than that for the neat film. More recently Cunningham *et al.* [113] observed very little change in peak photoconductivity upon the addition of PCBM. However, it is the subsequent evolution of the photoconductivity that reveals the difference between the neat polymer and the bulk heterojunction blend. As shown in Figure 6.3, in P3HT the conductivity decreases rapidly over the first few picoseconds, and subsequently decays according to the power law $\Delta\sigma \propto t^{-\beta}$ with $\beta = 0.31 \pm 0.03$. This kind of power law decay is a signature of the dispersive transport of charges in disordered media [99], as discussed further in Section 2.4. In contrast, the conductivity dynamic in the P3HT:PCBM blend is significantly slower, with a lifetime substantially longer than the ~ 1 ns range in the current experiment.

The photoinduced conductivity for the P3HT:PCBM film under photoexcitation at the $\pi - \pi^*$ absorption peak (560 nm) is shown in the inset to Figure 6.2. The dynamics are qualitatively identical to those seen when 800 nm excitation is used, suggesting that the same species is photoexcited under both excitation conditions.

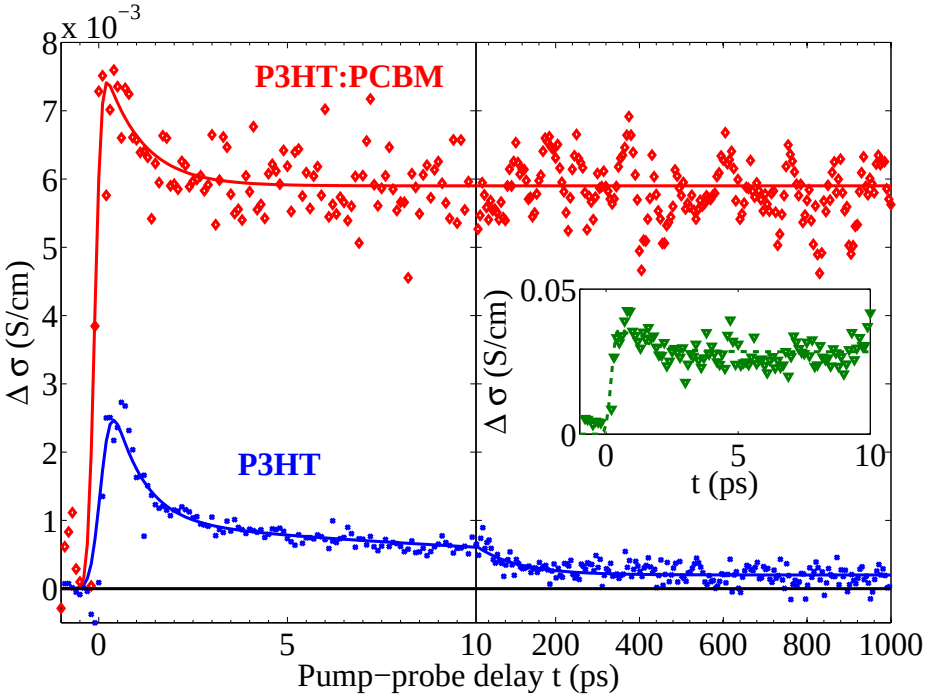

Figure 6.2: Photoinduced change in conductivity for thin films of neat P3HT (blue circles) and P3HT:PCBM (red diamonds) as a function of time after excitation with an 800 nm optical pulse at a fluence of 425 μJ cm^{-2}. The inset shows the photoinduced change in conductivity of the blend after excitation with an 560 nm optical pulse at a fluence of 210 μJ cm^{-2}. Lines shown are a guide to the eye.

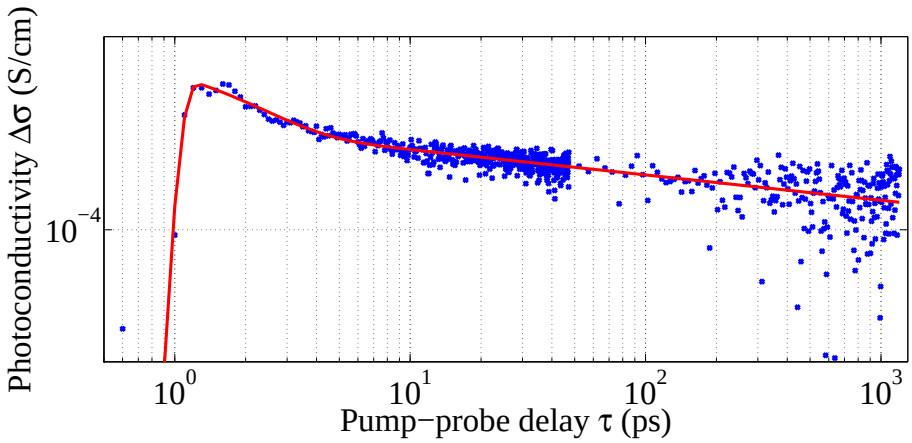

Figure 6.3: Photoinduced change in conductivity for thin films of neat P3HT (as in Figure 6.2) shown on a double logarithmic scale. The line is a fit using a model based upon the sum of a single exponential and a dispersive ($t^{-\beta}$) component.

To garner further information about the photoexcited species created in both case, a fixed-pump measurement was taken at 1.2 ns delay after excitation, at which time the system has entered a quasi-equilibrium state. Figure 6.4a shows the terahertz-frequency spectra of the photoinduced conductivity for the P3HT:PCBM film after excitation at 800 nm and 560 nm. The spectral signature of the conductivity response is almost identical for both excitation wavelengths, again indicating that the same type of species is generated for above-gap and below-gap excitation, at high fluences.

For inorganic semiconductors [149] and heavily doped polymers [224, 225] the Drude model of free carriers has been found to model the terahertz conductivity accurately. The observed monotonic increase in the real and imaginary parts of the conductivity in Figure 6.4a is in clear disagreement with the Drude model, which predicts a maximum in the real part of the conductivity at $\omega = 0$ and a positive imaginary component peaked at the inverse scattering time of the carriers. Similar conductivity spectra have been recently reported for polymer:fullerene blends using high excitation fluences near the peak of the polymer absorption spectrum [112, 115, 117, 216]. The microscopic origin for the terahertz photoconductivity spectra of semiconducting polymers is currently a well-debated issue in the literature. It has been suggested

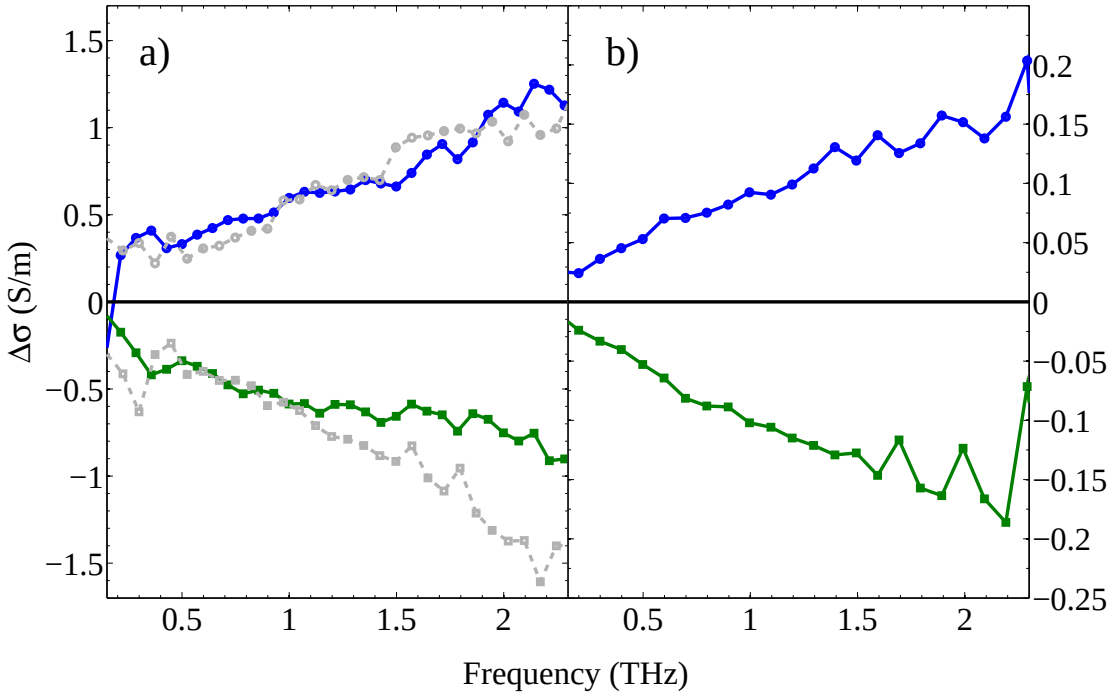

Figure 6.4: Photoinduced conductivity spectra across in the terahertz region for the P3HT:PCBM film (a) taken on the high-fluence amplifier system at 1.2 ns after excitation with 800 nm-photons of fluence 425 μJ cm^{-2} (blue and green lines) and after excitation with 560 nm-photons of fluence 210 μJ cm^{-2} (grey dashed lines, divided by 10 to allow comparison); (b) taken on the low-fluence oscillator system after excitation with 800 nm-photons of fluence 0.64 μJ cm^{-2} for a nominal delay time of 10 ps.

that such terahertz frequency response may arise from a charge conductivity limited by torsional disorder along the polymer backbone,[116] or from the back-scattering of charges from the ends of conjugated segments, leading to a maximum in the conductivity at non-zero frequency [112] as described in the Drude-Smith model [168]. Additionally, the terahertz-frequency conductivity of polarons in polymer blends has been modelled as a Debye relaxation process [115]. In order to distinguish between these competing models, THz-TDS experiments are required at frequencies higher than 2.5 THz (the maximum frequency accessible in this study, and also in those presented in References [112–114]).

Figure 6.5 shows the photoinduced conductivity for P3HT and P3HT:PCBM films

as a function of time after excitation at 800 nm, measured with the laser oscillator system at an excitation fluence roughly three orders of magnitude below that used to acquire the data shown in Figure 6.2. In order to obtain a sufficiently high signal-to-noise ratio at such low fluences using current techniques it is inevitable that higher pulse repetition rates be used. As a result, no increase in photoconductivity is now seen at $t = 0$ ps, suggesting that the predominant species present on time-averaging has a lifetime that exceeds the inter-pulse separation of the laser oscillator (12.5 ns) by a significant amount. For example, if it is assumed for simplicity that only one species was present which decayed exponentially, then its lifetime would need to exceed $\sim$100 ns for a rise near zero delay to be unresolvable due to signal fluctuations. The long-lived nature of the species strongly suggests that the low-fluence measurements predominantly probe free charges in the material. This conclusion is supported by the fact that a significant increase ($\times$24) in the time-averaged conductivity can be observed when PCBM is added to P3HT. P3HT:PCBM photovoltaic devices are known to exhibit good external quantum efficiency [89], and it is therefore to be expected that the primary time-averaged photoexcited species in these materials are free charge carriers. In order to determine the terahertz signature of free charges in the polymer, the photoinduced conductivity spectrum was taken for the P3HT:PCBM film, as shown in Figure 6.4b. Comparison with the data taken on the high-fluence system unambiguously confirms that for all three types of measurement, i.e. at 1 ns after excitation below-gap or above-gap with high fluence, and on time-average after excitation below-gap with low-fluence, the predominant species causing a change in terahertz transmission for P3HT:PCBM films are free charges. Section 6.4 contains further discussion on the possible charge generation mechanisms for polymers and polymer:fullerene blends photoexcited above and below the $\pi - \pi^*$ absorption edge.

Both high- and low-fluence OPTP systems were used to assess the fluence-dependence of the photoinduced conductivity, which may provide information about charge-carrier

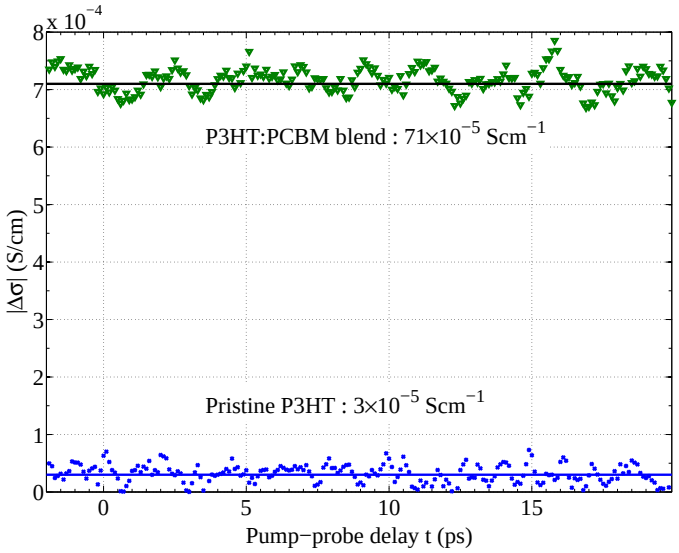

Figure 6.5: Photoinduced change in conductivity for neat P3HT and P3HT:PCBM blend films as a function of time after excitation at 800 nm using the low-fluence ($0.64\,\mu\mathrm{J\,cm^{-2}}$), high-repetition rate system. No rise in photoconductivity can be observed at zero delay (corresponding to the arrival of the excitation pulse), indicating that the photoconductivity lifetime is significantly longer than the laser inter-pulse period ($\Delta t = 12.5$ ns).

generation and carrier-carrier scattering mechanisms, and about the trap density in the material [111, 166]. Such measurements are particularly useful to attempt to relate the photovoltaic efficiency measured in a high-fluence laboratory setting to a real world (air mass 1.5) environment. Figure 6.6 shows the spectrally and temporally averaged photoconductivity as a function of excitation fluence f for P3HT:PCBM and MDMO-PPV:PCBM blends photoexcited at 800 nm. From the double-logarithmic representation it can be seen that the fluence-dependence of the conductivity follows a power law of the form $|\Delta\sigma| = Af^B$. Best fits to the data are shown as lines in the graph and yield an approximate dependence of the photoconductivity upon the square-root of the fluence for P3HT:PCBM and MDMO-PPV:PCBM within the low fluence regime ($B = 0.48 \pm 0.01$ and $B = 0.49 \pm 0.01$ respectively), and a linear dependence ($B = 0.98 \pm 0.02$) for P3HT:PCBM at high fluences. However, while the two polymers investigated show a similar fluence-dependence of the photoconductivity, its overall value is larger for P3HT than for MDMO-PPV by approximately

an order of magnitude. The implications of the fluence-dependence of the terahertz photoconductivity for the blend films on the mechanisms of charge carrier generation and recombination are examined in detail in the Discussion section below.

6.4 Discussion

In this section I aim to place the present and previous results from OPTP spectroscopy of polymeric semiconductors in the context of reported charge generation and transport mechanisms in these materials. The absorption of a photon by a π-conjugated polymer begins a chain of events that may result in charge generation. In neat polymer films, Coulombically bound electron-hole pairs (excitons) are the primary species created at low photoexcitation densities, with a photon-to-charge ratio ϕ of typically less than 1% [110]. In P3HT:PCBM blend films ϕ may be as large as 65%, facilitating the use of this blend in high-efficiency organic photovoltaic devices [92]. Once created, excitons may migrate either along a polymer chain by hopping to neighbouring conjugated segments, between chains, or into a charge-separated state. Alternatively, excitons may decay via a radiative or non-radiative process. A charge-separated state is one in which the (still-bound) electron and hole become separated between two conjugated segments, or over an interface [86, 221]. In these states, it is possible that an energy-mismatch between segments or components may help to overcome the exciton binding energy [36, 226, 227]. In the case of a P3HT:PCBM blend, charge separation has been proposed to occur predominantly at the bulk interface between the polymer and the fullerene, generating an electron on the PCBM and the hole on the polymer [83]. Using the above- and below-gap excitation dynamics and spectral conductivity "fingerprint" presented above, more detail can be presented regarding the charge generation and recombination mechanisms in these polymer-fullerene blends. Subsequently, an estimate of the lower bounds to the mobility μ and bimolecular

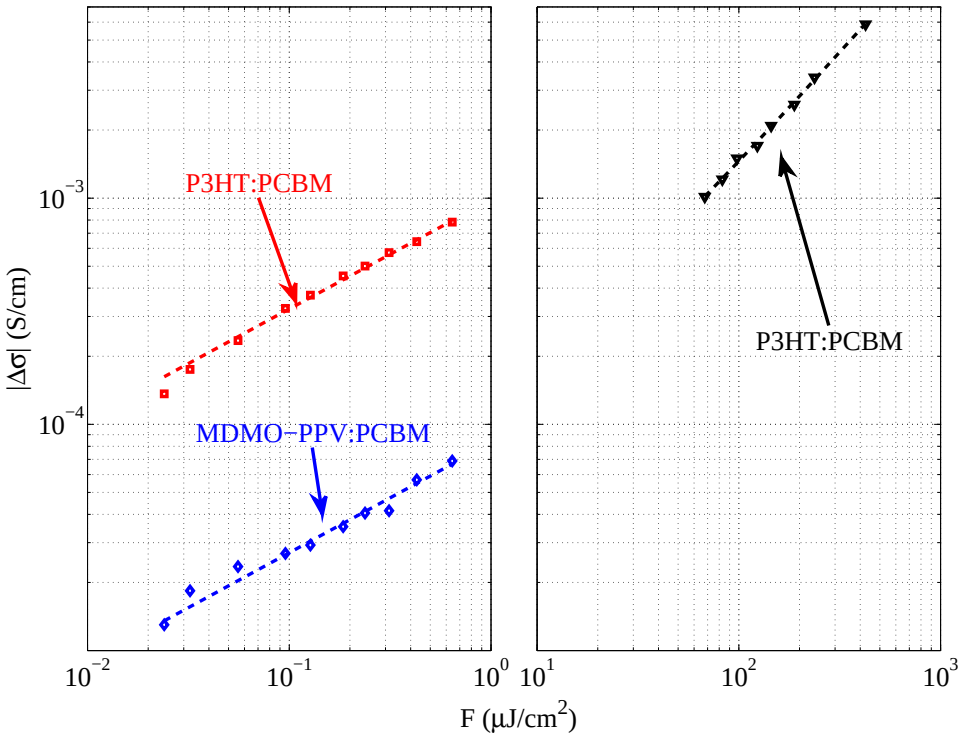

Figure 6.6: Fluence-dependence of the photoinduced change in conductivity at 800 nm for MDMO-PPV:PCBM (blue diamonds) and P3HT:PCBM (red squares) measured with the low-fluence system, and for P3HT:PCBM measured with the high-fluence system (black triangles). For the low-fluence regime the data points are the average of photoconductivity transients measured in the nominal delay range of -2–20 ps (as shown e.g. in Figure 6.5), while for the high-fluence regime the average was taken over the long-term delay scans between 0.08–1.2 ns (as displayed in the right panel of Figure 6.2). Both methods yield the spectrally averaged value of the terahertz photoconductivity for the times at which the spectrum carries a charge-carrier signature. The low-fluence data represent a time-averaged photoconductivity value, while the high-fluence data corresponds to the charge yield before recombination. The lines shown are power-law fits yielding approximately square root and linear dependencies for low fluence and high fluence experiments, respectively, as described in the text.

annihilation constant γ of charge carriers is presented, by calculating the products $\phi\mu$ and $\phi\gamma$ from the measured fluence-dependencies of the photoconductivity.

6.4.1 Carrier generation and recombination

The origin of the induced conductivity for photoexcitation at energies significantly below the peak of the $\pi - \pi^*$ absorption needs further consideration. Below, the discussion of the possible carrier generation mechanisms is divided into those applicable at low and high photon fluence, and the changes that occur on blending neat P3HT with PCBM are considered.

Charge generation routes that are intrinsic to neat conjugated polymer solids have been discussed in much detail in the literature [72, 75, 80, 228–230]. For the below-gap excitation of P3HT films, as carried out in the present study, it is possible that electronic states are excited in the low energy tail of the distribution, corresponding to very long conjugated polymer segments. The small yet finite absorbance of the samples at 800 nm suggests that this is feasible, in particular given the large thickness of the films. However, such states would have the minimum energy required for the generation of an exciton in the material, while a number of theoretical models indicate that an excess energy may be required for an exciton to dissociate into charges. Such excess energy may, for example, lead to a larger initial separation between electron and hole [74], which according to the Onsager model [70] will lead to a higher charge separation probability. Excess vibrational energy associated with the polymer backbone has also been postulated to enhance the on-chain dissociation probability [75]. In addition, the energetic mismatch between adjacent sites in the inhomogeneously broadened density of states present in the films may be utilised to overcome the barrier to charge separation of the exciton [72, 228, 229].

However, a number of studies on polythiophene films have demonstrated that these materials do not comply with such models and instead show charge generation effi-

ciencies that are essentially independent of the energy of the exciting photons across the lowest electronic transition band [79, 118, 219]. This effect has been attributed to either the presence of an ordered lamellar structure in regio-regular P3HT [79] or the availability of special "dissociation sites" comprising chain kinks, twists or aggregates [219, 231]. The former study proposed an intrinsic charge separation efficiency of 2% while the latter two concluded it to be as high as 13–20% within the lowest absorption band. According to these studies, direct intrinsic photogeneration of charges should be expected to occur to a significant extent for the P3HT films under investigation here.

Intrinsic charge generation cannot, however, be the only mechanism in operation as the addition of PCBM to P3HT is found to increase the initial photoconductivity, even though the density of P3HT spectroscopic units is reduced (Figure 6.2). Therefore, extrinsic mechanisms for charge generation in P3HT introduced through the addition of the electron acceptor PCBM also need to be considered. For the case of polymer-fullerene blends, a specific charge transfer state has recently been identified as an extrinsic, below-gap route to charge photogeneration. This directly accessible state with less than ∼1.5 eV excitation energy was found to be present in P3HT:PCBM and MDMO-PPV:PCBM blends, and absent in neat P3HT, MDMO-PPV or PCBM films [87]. Similar effects have also been noted in polyfluorene-fullerene blends [88, 227]. It was subsequently suggested that the relevant features in the absorption correspond to a weakly-bound polaron pair, as they occur concomitantly with efficient charge photogeneration [87, 88]. The final product of exciting these sub-gap features would thus be a charge separated state such as a free polaron, with an electron transferring to the PCBM and the hole remaining on the polymer chain [83, 226]. Using ultrafast transient absorption, Hwang *et al.* have recently shown that for P3HT:PCBM blends, a charge-transfer state exists operating as an intermediate state between the photoexcitation of an exciton and free polaron conduc-

tivity [81]. Such a state was not observed in neat P3HT films. The high photoinduced terahertz conductivity measured for below-gap excitation of these blends across all excitation fluences strongly suggests that such direct excitation of a sub-gap charge transfer state is a principal mechanism contributing to charge generation here.

Ultrafast (<100 fs) charge generation in conjugated polymeric films at high excitation fluences has been reported on a number of occasions,[73, 80, 82, 232–235] with the mechanisms remaining the subject of much controversy. For example, it has been suggested that a two-step, two-photon absorption to specific higher-lying even-parity states in poly-phenylenevinylene may lead to subsequent efficient relaxation of the exciton into a charge-separated state [73]. At high excitation densities, such states may be accessed by sequential two-photon absorption within the duration of the excitation pulse, leading to a super-linear dependence of the charge generation efficiency on excitation fluence. For example, Silva *et al.* have used photoinduced absorption measurements to show that the only route to photogeneration of polarons in thin films of a polyindenofluorene derivative is via such two-step excitation processes [80, 235]. Alternatively, Müller *et al.* have postulated that these two-step photon absorption processes in neat polymer films generate a fraction of bound polaron pairs as a first step, whose subsequent re-excitation by a second photon pulse leads to their dissociation into free charges [234]. Interestingly, a subsequent study by the same authors showed that for efficient polymer:PCBM photovoltaic blend films, such initial bound polaron pairs are absent, and therefore the arrival of a second pulse is unable to generate further free charges [82]. Both of the postulated mechanisms for direct, two-step charge photogeneration will thus lead to a super-linear increase in the charge generation efficiency for neat polymer films with photon fluence. However, for efficient donor-acceptor blends, a linear fluence-dependence of the photon-to-charge conversion efficiency may occur if extrinsic mechanisms at the heterojunction become the dominant pathway to charge generation.

In addition to the fluence-dependence of the initial generation of charges the subsequent recombination of charges has also to be considered. Here, bimolecular charge carrier recombination dynamics may lead to a sub-linear dependence of the time-dependent charge population with excitation fluence. Previous studies of microwave conductivity on P3HT:PCBM films noted an onset of bimolecular charge carrier recombination at an incident photon fluence of around $5\times10^{12}\,\mathrm{cm}^{-2}$, but did not report any evidence of two photon effects for fluences up to $10^{15}\,\mathrm{cm}^{-2}$ [111]. In a similar study, Dicker *et al.* used time-resolved microwave conductivity measurements on thin films of P3HT to demonstrate that the photoconductivity increases sub-linearly over the range $10^{13}\,\mathrm{cm}^{-2}$ to $4\times10^{15}\,\mathrm{cm}^{-2}$, attributing this to secondary processes (e.g. bimolecular charge recombination) [79]. An OPTP measurement taken on P3HT:PCBM blend films using a 500 nm optical pump in the range $2.5\times10^{14}\,\mathrm{cm}^{-2}$ to $2\times10^{15}\,\mathrm{cm}^{-2}$ also shows an initial sub-linear fluence dependence of photoconductivity with excitation power (over the time range $1 < t < 75\,\mathrm{ps}$), in agreement with bimolecular charge generation occurring already within the duration of the excitation pulse [112].

The incident fluence used in the experiments reported here ranged from $9\times10^{10}\,\mathrm{cm}^{-2}$ to $1.7\times10^{15}\,\mathrm{cm}^{-2}$ per pulse at 800 nm, therefore, all of the excitation processes discussed above are likely to contribute to some extent. In order to make a qualitative statement on their relative importance, the fluence-dependence of the terahertz photoconductivity signal has been measured over more than four orders of magnitude, which is now discuss in more detail.

6.4.2 Dependence of charge carrier conductivity on excitation fluence

An ultimate goal of the spectroscopic analysis of organic photovoltaic materials is to understand both the charge generation method and to find an appropriate model for

carrier mobility. However, without independent knowledge of the photon-to-charge branching ratio ϕ and in absence of a universally accepted model for high-frequency charge mobility μ, one can only compare the product of these two quantities. In the following the differences in fluence-dependence of the photoconductivity observed for the two fluence regimes are examined, and use this information to assess charge mobility and recombination in the material.

Figure 6.6 illustrates a marked contrast between the low and high fluence photoconductivity data measured for P3HT:PCBM films. As stated in Section 6.3, the data can be well modelled for both fluence regimes using a power-law function, with the low-fluence regimes displaying a square-root, and the high-fluence regime a linear dependence of photoconductivity upon incident fluence. However, for a meaningful comparison of the data sets taken within the two regimes one has to consider that the high-fluence photoconductivity is measured over the first nanosecond after excitation whereas the low-fluence data is essentially an average over the whole charge lifetime. For the high-fluence regime, the photoconductivity displayed in Figure 6.6 is an average over 0.08–1 ns after excitation, for which a constant value is observed in the conductivity dynamics (see Figure 6.2). These data thus represent the conductivity state of the material *after* the initial charge-generation processes have occurred within the first few picoseconds, but *before* any significant charge-carrier decay has occurred. The low-fluence data, on the other hand, is strongly influenced by "wrap-around" effects: the lack of any step-wise increase in the photoconductivity at $t = 0$ (see Figure 6.5) demonstrates that a significant photoexcited charge-population remains after 12.5 ns, the inter-pulse period of the laser. A meaningful comparison with the high-fluence data is only possible if the evolution of the conductivity signal beyond 1 ns after excitation is known as the low-fluence data must then be corrected for the build-up of carriers from previous excitation pulses.

In general, the photoconductivity of the blend is given by $\Delta\sigma = Nq\mu$, where N

is the carrier density, q is the electronic charge and μ is the effective carrier mobility for the conductive polaron species. For the *high-fluence* data, the linearity of the photoconductivity power-dependence suggests that extrinsic charge generation at the P3HT:PCBM heterojunction is the primary mechanism for initial photon-to-charge conversion even at fluences as high as $500\,\mu\mathrm{Jcm}^{-2}$. An initial (picosecond) value of $\phi\mu$ may then be extracted from the high-fluence measurements of the initial photoconductivity $\Delta\sigma_0$ using:

$$\phi\mu = \frac{\Delta\sigma_0}{q\, n_0^{\mathrm{photon}}} \tag{6.2}$$

where $n_0^{\mathrm{photon}} = \left(1 - e^{-\alpha d}\right) I_0/d$ is the initially generated average photon density derived from the absorption coefficient α, the sample thickness d, and the number of photons I_0 incident per unit area. Using this approach, a value of $\phi\mu$=0.11$\mathrm{cm}^2\mathrm{V}^{-1}\mathrm{s}^{-1}$ is determined for excitation at 800 nm by performing a linear fit to the fluence-dependence of the conductivity shown in the right side of Figure 6.6.

To interpret the *low-fluence* conductivity data, it has to be taken into account that the carrier density is built up by successive pulses creating the "wrap-around" effect mentioned in the previous paragraph. The sub-linear fluence-dependence observed could be caused by non-linear effects in the charge generation and/or recombination processes. However, the linear fluence dependence of the photoconductivity in the high-fluence regime suggests that the latter is the case. Following the treatment outlined by Dicker *et al.* in Reference [79], the rate of change of carrier density taking into account a bimolecular decay route, can be written as

$$\frac{dN}{dt} = \frac{\phi n_0^{\mathrm{photon}}}{\Delta t} - \gamma N^2 \tag{6.3}$$

where γ is the bimolecular charge annihilation constant. Since the inter-pulse separation Δt=12.5 ns is significantly shorter than the charge lifetime for the present case, the steady-state charge density N_∞ leading to the observed photoconductivity

is given by

$$N_\infty = \sqrt{\phi n_0^{\text{photon}}/(\Delta t\,\gamma)}. \tag{6.4}$$

Since it is observed that there is a dependence of photoconductivity on the square-route of excitation fluence, such bimolecular charge annihilation effects appear to be the predominant mechanism for the photoconductivity decay over the lifetime of the charge species, both in P3HT:PCBM and MDMO-PPV:PCBM blend films. The product $\phi\gamma$ of the photon-to-charge branching ratio and the bimolecular charge annihilation constant may then be written as:

$$\phi\gamma = \frac{n_0^{\text{photon}}}{\Delta t}\left(\frac{q\,\phi\mu}{\Delta\sigma}\right)^2. \tag{6.5}$$

A square-root fit to the low-fluence photoconductivity data for P3HT:PCBM blends (Figure 6.6, left) provides a value of $\phi\gamma$=1.94×10^{-11} cm^{3}s^{-1} using the high-fluence value of $\phi\mu$=0.11 cm^{2}V^{-1}s^{-1}.

Using Equation 6.4 and these calculated values, it is possible to calculate the steady-state carrier density in the low-fluence case, as shown in Figure 6.7. Since the photon-to-charge branching ratio must be smaller than one, the above considerations provide lower limits to the charge mobility and bimolecular charge annihilation constant of 0.11 cm^{2}V^{-1}s^{-1} and 1.94×10^{-11} cm^{3}s^{-1}, respectively, for photoexcitation of P3HT:PCBM blends at 800 nm. However, as previous studies have suggested a high initial photon-to-charge conversion ratio for such blend systems [112, 236] these values are likely to be of the same order of magnitude as the actual charge mobility and bimolecular annihilation constant. As previously reported [112], the early time conductivity dynamic ($<$ 1 ns) often differs significantly from the later time dynamic as the competition between the possible decay routes varies; i.e. between charge recombination at an interface and polaron-polaron annihilation. In the presented case, the high-fluence data provides an early time measurement in which exciton-dissociation

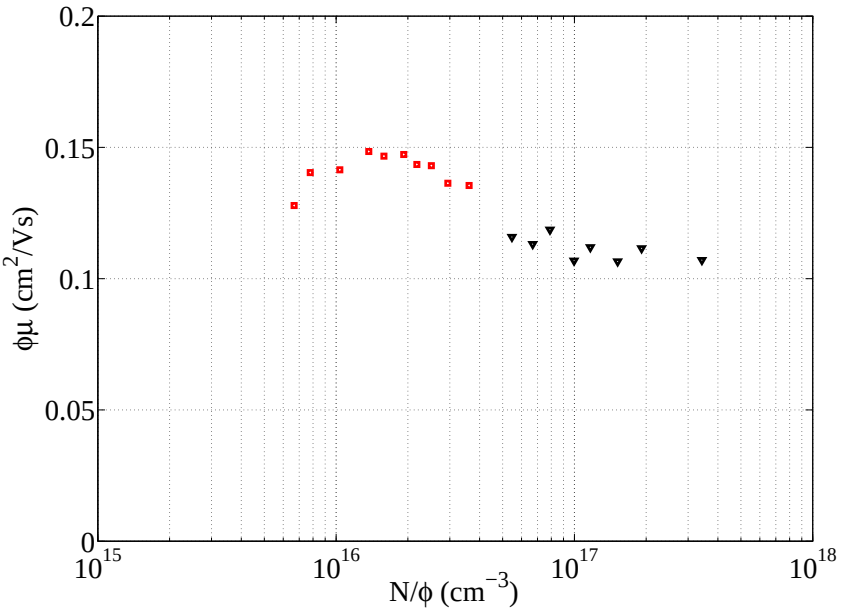

Figure 6.7: Using Equation 6.2 (Equation 6.4), the value of $\phi\mu$ can be calculated for each instantaneous (steady-state) carrier density for the high-fluence (low-fluence) system, respectively.

λ (nm)	Fluence regime	$\phi\mu$ ($\mathbf{cm^2V^{-1}s^{-1}}$) P3HT	P3HT:PCBM
800	H	0.073	0.11
	L	N/A	*0.11*[1]
560	H	N/A	0.072

Table 6.2: Summary table for $\phi\mu$. Fluence regime refers to either H (high-fluence, low-repetition rate) or L (low-fluence, high-repetition rate).

at a P3HT:PCBM interface dominates, while the low-fluence data represents a time-averaged measurement over the lifetime of the photoexcited species for which polaron-polaron annihilation is the primary decay route [79].

To compare these values with those recorded under above-gap photoexcitation, the product $\phi\mu$ was extracted from the photoconductivity data shown in the insert of Figure 6.2 as measured for excitation at 560 nm with a fluence of 210 μJcm^{-2}. A value of $\phi\mu_{560\text{nm}} = 0.072\,\text{cm}^2\text{V}^{-1}\text{s}^{-1}$ is obtained at 5 ps after excitation, somewhat

[1]The value of $\phi\mu$ was fixed at the high fluence value, to be able to extract γ from the experimental data.

smaller than the value at 800 nm of $\phi\mu_{800\text{nm}} = 0.11\,\text{cm}^2\text{V}^{-1}\text{s}^{-1}$. If similar carrier mobilities for the charge-separated state produced after the photoexcitation of excitons at 560 nm and the photo-product at 800 nm were assumed this would imply that the charge generation efficiency is surprisingly high when the charge transfer state is excited resonantly. For actual photovoltaic devices incorporating thin (d≈100 nm) films this charge transfer state may however still not provide a major route towards photocurrent generation as the associated sub-gap absorption appears to be relatively weak [87].

The lower limit of $1.94\times10^{-11}\,\text{cm}^3\text{s}^{-1}$ found for the charge annihilation rate is significantly lower than values for γ found previously for neat polymer films: For both neat P3HT [79] and poly(phenylene vinylene) [220] a value of γ has been determined to be $\sim 1\times10^{-8}\,\text{cm}^3\text{s}^{-1}$. For P3HT it was suggested that the value correlates with the charge carrier density for which there appear to be a significantly high number of lamellae with two carriers present, leading to efficient charge annihilation within a lamellae [79]. The value determined for the blend is approximately 2–3 orders of magnitude smaller than those seen for neat polymer films, which should be expected since it is the interface surface forming the heterojunction between P3HT and PCBM that will influence the probability of an encounter between oppositely charged polarons in the blend thus lowering the probability of bimolecular charge recombination. This contrast between the charge recombination in neat and blend films is self-evident from the conductivity dynamics for the two materials displayed in Figure 6.2.

The values of $\phi\mu$ reported here is approximately an order of magnitude larger than those observed using the time-resolved microwave conductivity technique with a similar excitation fluence [111, 237]. This observation is in accordance with the frequency spectrum of the conductivity displayed in Figure 6.4, from which a significant conductivity drop towards microwave frequency should be expected. The mobility and quantum efficiency values reported by both Ai *et al.* and Cunningham *et al.* us-

ing OPTP are significantly larger than those presented here [112, 113]. This is likely to be a result of the use of Drude-Smith modelling in these studies, as the presence of a strong back-scattering parameter requires that a larger carrier mobility must be used to explain a given conductivity.

Finally, the product $\phi\mu$ for neat P3HT films photoexcited at 800 nm at very high fluences ($425\,\mu\mathrm{Jcm}^{-2}$) was determined to be $\phi\mu = 0.073\,\mathrm{cm}^2\mathrm{V}^{-1}\mathrm{s}^{-1}$. This value is only slightly below that determined for the P3HT:PCBM blend films, and therefore surprisingly high given that the addition of PCBM is expected to increase significantly the quantum efficiency of charge generation. If the photon-to-charge branching ratio were indeed significantly lower for the neat film than for the blend, a strong reduction of charge mobility would be required upon blending to achieve the observed values of $\phi\mu$. The addition of PCBM should decrease the mobility of carriers in P3HT to some extent [238], since the polymer:fullerene heterojunction is most effective where the micro-crystalline phases in the blend are around 5-10 nm in size [52, 82]. However, recent investigations of P3HT:PCBM blend films indicate that that self-organisation of P3HT into ordered domains is still effective even in the presence of 50 wt% PCBM [202]. Any decreases in mobility with blending are thus likely to be small, suggesting that ϕ for the neat P3HT film cannot be much lower than that for the blend, at the high photon fluences used for excitation here. It is therefore likely that in the high-fluence regime, additional non-linear mechanisms of charge generation, as discussed in detail the previous section, are in operation for neat P3HT. However, the linear increase of the initial photoconductivity with excitation fluence observed for P3HT:PCBM films suggests that for these a direct photogeneration of charges at the heterojunction is the predominant mechanism, in agreement with the interpretation by Müller *et al.* [82] of transient absorption and photocurrent enhancement measurements conducted on PCBM:MDMO-PPV blend films.

6.5 Conclusions

In this chapter, the terahertz-frequency photoconductivity of two model polymer-fullerene blends has been presented, varying the incident fluence over four orders of magnitude. It is observed that a qualitatively similar time dynamic and terahertz-frequency conductivity spectrum arise upon photoexcitation at energies resonant with the peak of the $\pi - \pi^*$ absorption and well below it. The values of $\phi\mu$ (summarised in Table 6.2), the quantum efficiency for charge generation multiplied by the carrier mobility, are comparable at these two photoexcitation energies, suggesting that the direct excitation of an intermediate charge-transfer complex is an efficient route to free charge generation. The time-averaged terahertz photoconductivity, obtained using a terahertz spectrometer based on a laser oscillator, reveal that the photoconductivity is enhanced by a factor of over 20 upon blending P3HT with PCBM. Finally, the fluence dependence of the photoconductivity demonstrate that different mechanisms for charge relaxation occur over different timescales; at early times ($< 1\,\mathrm{ns}$) the linear dependence of photoconductivity upon fluence indicates that interfacial charge transfer dominates as an exciton decay pathway, generating charges with mobility of at least $\sim 0.1 \mathrm{cm}^2\mathrm{V}^{-1}\mathrm{s}^{-1}$. At later times, a sub-linear relationship shows that carrier-carrier recombination effects influence the conductivity on a longer timescale ($> 1\,\mu\mathrm{s}$). Analysis of the time-averaged photoconductivity data suggests that the bimolecular charge annihilation constant for these blends is approximately 2–3 orders of magnitude smaller than that typical for neat polymer films, in accordance with a more stable charge-separated state for the blend system.

Chapter 7

Conclusion

In this thesis, the electronic processes that occur in reduced dimensionality semiconductor blends, nanoscale inorganic semiconductors and bulk heterojunctions of organic semiconductors have been presented, which were investigated using ultrafast spectroscopic measurements. The unifying feature of these topics lies in the strongly non-bulk behaviour of these nanoscale materials, however each system varies in the nature of their specific response due to spatial confinement. Both organic and inorganic semiconductors have been examined, and while each is inherently different on the microscopic level (for example, showing considerably different processes following the absorption of a photon), the applicability of the ultrafast photoconductivity measurements to both permits generalisation of concepts across the semiconductor field. In this chapter, the key results are briefly reviewed, and suggestions for future extension of the work are given.

In Chapter 4, three common luminescence polymers were blended to permit white-light emission. The energy transfer mechanism responsible for the downhill exciton migration was shown to be well modelled by Förster incoherent dipole coupling. Förster transfer has an explicit dependence upon the separation of donor and acceptor molecules – when a spatial ensemble is taken over a polymer ensemble, the energy

transfer rate becomes dependent upon the dimensionality of the system. By dividing the photoluminescence decay transient of the donor molecule (F8) both without and with the guest molecules present, the component of the decay due to energy transfer was isolated. By performing this analysis for a thin-film sample (three-dimensional) and a sample in which the blend is intercalated into the interplane galleries of an inorganic semiconductor matrix (quasi-two dimensional), the theoretical predictions from Förster theory could be compared with experimental data. A strong agreement between the theory and experiment was taken as evidence that the dimensionality-dependent Förster model was appropriate for this system. In addition, the results suggested that the approximations of the theory (particularly the point-dipole approximation) were sound in this system. The restriction of energy transfer using dimensionality reduction is preferable to using strong dilution of the guest molecule, as a percolation path through the material is maintained.

In Chapter 5, the ultrafast photoconductivity of a nanoscale inorganic semiconductor was presented. Performing electrical conductivity measurements upon nanoscale inorganic materials present many of the same challenges as their organic semiconductor counterparts – primarily the difficulty creating electrical contacts and issues associated with ultrashort carrier lifetimes. Gallium Arsenide nanowires were studied, and the carrier lifetime was found to be several orders of magnitude shorter than that in bulk Gallium Arsenide, and strongly non-exponential. Using optical-pump terahertz-probe spectroscopy, the complex conductivity was obtained over the terahertz spectrum. By applying modelling based upon a morphological ensemble of nanowires, two types of nanowires were identified. The nanowires with their long axis aligned along the terahertz probe electric field produced a Drude-type response, associated with free carriers. However, those aligned perpendicular to the terahertz probe exhibited a surface plasmonic response, associated with direct excitation of normally forbidden surface electronic modes. The surface plasmon mode provided a reliable

handle upon the carrier density, and the emergence of the surface plasmon mode was shown to occur within the first 300 fs after excitation. The carrier mobility extracted using this technique was only 1/3 of that observed for bulk Gallium Arsenide, suggesting a pure and defect-free growth. In order to understand the effect of surface trap states, a surface passivation technique was applied. While the carrier lifetime was seen to improve, no significant decrease in surface trap states was noted. This was attributed to a non-optimal passivation protocol, however, the sample was seen to remain passivated over several days in air indicating the promise of this technique in reducing surface trap density.

In Chapter 6, the electronic processes in neat and fullerene blended polymers following photon absorption were studied. The photoconductivity of P3HT, P3HT:PCBM and MDMO-PPV:PCBM was examined using terahertz spectroscopy after sub-gap and above-gap excitation. The effect of adding PCBM was shown to be an increase in photoconductivity and a large increase in carrier lifetime, suggesting that once the exciton is separated over the heterojunction interface it remains stable for many hundreds of nanoseconds, with a lifetime ultimately controlled by bimolecular recombination. By comparing the photoconductivity observed with sub-gap and above-gap excitation, a clear sub-gap route to charge generation was found. As the sub-gap excitation has insufficient energy to create a free exciton on the polymer, a directly accessible interfacial charge-transfer state was hypothesised. This was in agreement with recent work by Goris *et al.* and others, in which the sub-gap state was seen as an essential intermediate state for exciton dissociation with a distinct sub-gap photoluminescence [81, 87, 88].

7.1 Future work

As suggested in the previous section, the surface of nanostructured Gallium Arsenide appears to have a strong effect upon the electronic dynamics. It would be of great interest to combine the techniques of Chapter 5 and 6 in order to use the nanowires together with an organic semiconductor to make a bulk heterojunction interface. The advantages of this approach lie in the proven high mobility of the Gallium Arsenide nanowires, providing a clear path for the electrons to the contacts of a photovoltaic device. In addition, the polymer will provide a high photon absorption, spectrally matched with solar emission.

An alternative experiment would be to combine the methods of PLUCS and OPTP-TDS to study aggregates and isolated chains of an organic semiconductor. By comparing the excitonic lifetime with the polaronic lifetime, a full picture of energy dynamics in organic semiconductors could be approached. In particular, both PLUCS and OPTP-TDS are polarisation-sensitive techniques – by aligning the polymer backbone, the excitonic electronic dipole moment of absorption and emission might be compared with the conductivity anisotropy. In combination with isolated polymer chains, the effect of reducing or eliminating intermolecular energy transfer can be seen for both excitons and polarons, providing unprecedented nanoscale, ultrafast information of energy dynamics in polymeric semiconductors.

Appendix A

Pump-probe analysis for thin non-uniform media

The conductivity of photoexcited Gallium Arsenide nanowires is presented in Chapter 5. In the case of non-uniform media, the analysis in Chapter 3 is no longer valid and the thin-film approach cannot be taken directly. Several techniques for treating such non-uniform cases have been presented, typically relying on an effective medium theory (EMT), such as the Bruggeman EMT [201] or the Maxwell-Garnett EMT [239]. EMT approaches typically rely on treating a sample as an interpenetrating matrix of two materials, each with an independent dielectric function. Both the Bruggeman and the Maxwell-Garnet approaches have been shown to work well within specific limits and approximations; Reference [240] provides a review of the principles and applications of generalised effective medium theory. However, these theories are not appropriate for the nanowires as presented. They do not have an effective thickness, and in some places the sample has no nanowires present. For this reason, an alternative method of extracting the photoexcited conductivity must be used, which is presented here.

Figure A.1 shows an scanning electron micrograph (SEM) of a typical section of

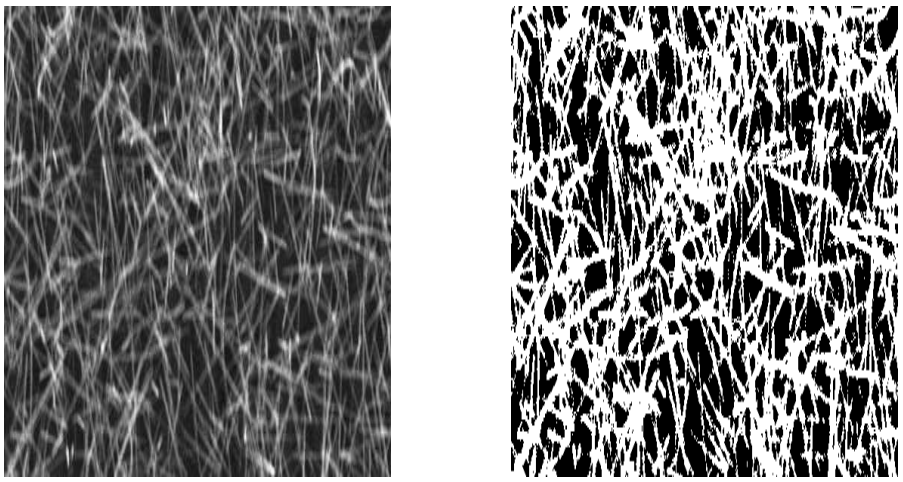

Figure A.1: The effective fill factor of nanowires is shown here. On the left is a standard 4000× magnification SEM image of a section of the nanowires. By discriminating the image based on grey-level, the right panel is produced, showing a 51% fill factor.

the nanowires sample. Using a discrimination algorithm, this image can be cleaned, and the effective areal fill factor of nanowires is obtained as $f_s = 0.51$. Following the working presented in Reference [166] and [241], the measured terahertz electric field with and without the optical pump is defined as

$$E_{\text{on}} = f_s E_{\text{s}^*} + (1 - f_s) E_{\text{r}^*}, \tag{A.1}$$

$$E_{\text{off}} = f_s E_{\text{s}} + (1 - f_s) E_{\text{r}}, \tag{A.2}$$

where E_{s} and E_{r} are the terahertz transmission through the sample and substrate, and the substrate only, and the $*$ indicates a photoexcited state. Assuming that the pump beam does not change the complex refractive index of the 'reference' material,

the electric fields may now be written as

$$E_{\mathrm{r}} = e^{in_{\mathrm{r}}\omega\delta/c}E_{\mathrm{i}} \tag{A.3}$$

$$E_{\mathrm{s}} = t_{\mathrm{vs}}t_{\mathrm{sv}}e^{in_{\mathrm{s}}\omega\delta/c}\mathrm{FP}_{\mathrm{vsv}}\mathrm{E_i} \tag{A.4}$$

$$E_{\mathrm{s}^*} = t_{\mathrm{vs}^*}t_{\mathrm{s}^*\mathrm{v}}e^{in_{\mathrm{s}^*}\omega\delta/c}\mathrm{FP}_{\mathrm{vs}^*\mathrm{v}}\mathrm{E_i} \tag{A.5}$$

where t_{ij} and FP are defined as the Fresnel transmission function and term corresponding to the Fabry-Perot effect, as in Section 3.3.3. In addition, one may assume that the reference material is vacuum, as in all but the vertically aligned case the terahertz probe will progress from vacuum to sample to vacuum. Experimentally $\Delta E(\tau,\omega)/E(\tau,\omega)$ is determined, and coupled with Equations A.1 and A.2 the following relationship can be written:

$$\frac{\Delta E}{E} = \frac{E_{\mathrm{on}} - E_{\mathrm{off}}}{E_{\mathrm{off}}} = \frac{f_s\left(E_{\mathrm{s}^*} - E_{\mathrm{s}}\right)}{f_s E_{\mathrm{s}} + (1-f_s)E_{\mathrm{r}}}, \tag{A.6}$$

from which a simple rearrangement provides

$$\frac{\Delta E}{E} = \frac{f_s\left(\frac{E_{\mathrm{s}^*}}{E_{\mathrm{s}}} - 1\right)}{f_s + (1-f_s)\frac{E_{\mathrm{r}}}{E_{\mathrm{s}}}}. \tag{A.7}$$

The ratio $E_{\mathrm{s}}/E_{\mathrm{r}}$ given by Equations A.3 and A.4, and is approximately constant for semi-insulating GaAs over the low terahertz range (well below the 8.0 THz optical-phonon mode), and equal to $E_{\mathrm{s}}/E_{\mathrm{r}} = 0.67$. To analytically determine the other ratio, $E_{\mathrm{s}^*}/E_{\mathrm{s}}$, the thin-film limit is required, where we are able to make the approximation

$$\frac{n\omega\delta}{c} \ll 1 \rightarrow e^{in\omega\delta/c} = 1 + i(n\omega\delta/c). \tag{A.8}$$

In this case, rearrangement of the Fabry-Perot terms in Equations A.4 and A.5, explicit manipulation of the Fresnel transmission coefficients and use of the thin-film

approximation allow the ratio E_{s^*}/E_s to be written as

$$\frac{E_{s^*}}{E_s} = \frac{2 - i\frac{\omega\delta}{c}(1 + n_s^2)}{2 - i\frac{\omega\delta}{c}(1 + n_{s^*}^2)}. \tag{A.9}$$

The following general relations can now be substituted into Equation A.9,

$$n_{s^*} = \epsilon_{s^*}^2 \tag{A.10}$$

$$\epsilon_{s^*} = \epsilon_s + \frac{i\sigma}{\omega\epsilon_0} \tag{A.11}$$

where ϵ_0 is the permittivity of free space. A final substitution back into Equation A.7 allows the conductivity σ to be related to the experimental data, with a final expression:

$$\sigma = \left(\left[2 - \frac{i\omega\delta}{c} - A\left(2 - \frac{i\omega\delta}{c}(1 + \epsilon_s)\right)\right]\frac{c}{i\omega\delta} - \epsilon_{rms}\right)\frac{\omega\epsilon_0}{i} \tag{A.12}$$

$$A = \left[\frac{1}{f_s}\frac{\Delta E}{E}\left(f_s + (1 - f_s)\frac{E_r}{E_s}\right) + 1\right]^{-1} \tag{A.13}$$

This equation was used to retrieve the photoconductivity of GaAs nanowires, as shown in Chapter 5.

Bibliography

[1] J Bardeen and W H Brattain. Physical principles involved in transistor action. *Phys. Rev.*, 75:1208–1225, 1949.

[2] M Pope, P Magnante, and H P Kallmann. Electroluminescence in organic crystals. *J. Chem. Phys.*, 38:2042, 1963.

[3] W Helfrich and W G Schneider. Transients of volume-controlled current and of recombination radiation in anthracene. *J. Chem. Phys.*, 44:2902, 1966.

[4] John Singleton. *Band Theory and Electronic Properties of Solids*. Oxford Master Series in Condensed Matter Physics. Oxford University Press, first edition, 2001.

[5] L H Chen, D W McBranch, H L Wang, R Helgeson, F Wudl, and D G Whitten. Highly sensitive biological and chemical sensors based on reversible fluorescence quenching in a conjugated polymer. *Proc. Natl. Acad. Sci. U. S. A.*, 96:12287–12292, 1999.

[6] G Horowitz. Organic field-effect transistors. *Adv. Mater.*, 10:365–377, 1998.

[7] P Peumans, A Yakimov, and S R Forrest. Small molecular weight organic thin-film photodetectors and solar cells. *J. Appl. Phys.*, 93:3693, 2003.

[8] R H Friend, R W Gymer, A B Holmes, J H Burroughes, R N Marks, C Taliani, D D C Bradley, JL Brédas, M Logdlund, and W R Salaneck. Electroluminescence in conjugated polymers. *Nature*, 397:121–128, 1999.

[9] Y Yang, E Westerweele, C Zhang, P Smith, and A J Heeger. Enhanced performance of polymer light-emitting-diodes using high-surface-area polyaniline network electrodes. *J. Appl. Phys.*, 77:694–698, 1995.

[10] T J Prosa, M J Winokur, J Moulton, P Smith, and A J Heeger. X-ray structural studies of poly(3-alkylthiophenes) - an example of an inverse comb. *Macromolecules*, 25:4364–4372, 1992.

[11] E Aharon, M Kalina, and G L Frey. Inhibition of energy transfer between conjugated polymer chains in host/guest nanocomposites generates white photo- and electroluminescence. *J. Am. Chem. Soc.*, 128:15968–15969, 2006.

[12] Peter Atkins and R Friedman. *Molecular quantum mechanics*. Oxford University Press, third edition, 1997.

[13] Mark Fox. *Optical Properties of Solids*. Oxford Master Series in Condensed Matter Physics. Oxford University Press, first edition, 2001.

[14] M Yan, L J Rothberg, F Papadimitrakopoulos, M E Galvin, and T M Miller. Defect quenching of conjugated polymer luminescence. *Phys. Rev. Lett.*, 73: 744–747, 1994.

[15] R Jakubiak, C J Collison, W C Wan, L J Rothberg, and B R Hsieh. Aggregation quenching of luminescence in electroluminescent conjugated polymers. *J. Phys. Chem. A*, 103:2394, 1999.

[16] E Hückel. Quantum-theoretical contributions to the benzene problem. i. the electron configuration of benzene and related compounds. *Zeitscrift für Physik*, 70:204, 1931.

[17] E Hückel. Quantum theoretical contributions to the problem of aromatic and non-saturated compounds. *Zeitscrift für Physik*, 76:658, 1932.

[18] Frank Pilar. *Elementary quantum chemistry*. McGraw-Hill, second edition, 2001.

[19] van Mullekom, J A J M Vekemans, E E Havinga, and E W Meijer. Developments in the chemistry and band gap engineering of donor-acceptor substituted conjugated polymers. *Mater. Sci. Eng. R-Rep.*, 32:1–40, 2001.

[20] Ira Levine. *Quantum Chemistry*. Prentice Hall, fifth edition, 2000.

[21] W P Su, J R Schrieffer, and A J Heeger. Solitons in polyacetylene. *Phys. Rev. Lett.*, 42:1698–1701, 1979.

[22] A J Heeger, S Kivelson, J R Schrieffer, and W P Su. Solitons in conducting polymers. *Rev. Mod. Phys.*, 60:781–850, 1988.

[23] D K Campbell and A R Bishop. Solitons in polyacetylene and relativistic-field-theory models. *Phys. Rev. B*, 24:4859–4862, 1981.

[24] K Fesser, A R Bishop, and D K Campbell. Optical-absorption from polarons in a model of polyacetylene. *Phys. Rev. B*, 27:4804–4825, 1983.

[25] C K Chiang, C R Fincher, Y W Park, A J Heeger, H Shirakawa, E J Louis, S C Gau, and A G MacDiarmid. Electrical-conductivity in doped polyacetylene. *Phys. Rev. Lett.*, 39:1098, 1977.

[26] M C J M Vissenberg and M Matters. Theory of the field-effect mobility in amorphous organic transistors. *Phys. Rev. B*, 57:12964, 1998.

[27] C Tanase, E J Meijer, P W M Blom, and D M de Leeuw. Local charge carrier mobility in disordered organic field-effect transistors. *Org. Electron.*, 4:33–37, 2003.

[28] C X Sheng, M Tong, S Singh, and Z V Vardeny. Experimental determination of the charge/neutral branching ratio eta in the photoexcitation of pi-conjugated polymers by broadband ultrafast spectroscopy. *Phys. Rev. B*, 75:085206, 2007.

[29] U Rauscher, H Bässler, D D C Bradley, and M Hennecke. Exciton versus band description of the absorption and luminescence spectra in poly(para-phenylenevinylene). *Phys. Rev. B*, 42:9830–9836, 1990.

[30] M Chandross, S Mazumdar, S Jeglinski, X Wei, Z V Vardeny, E W Kwock, and T M Miller. Excitons in poly(para-phenylenevinylene). *Phys. Rev. B*, 50: 14702–14705, 1994.

[31] M Chandross, F Guo, and S Mazumdar. Excitons and biexcitons in poly(para-phenylenevinylene). *Synth. Met.*, 69:625–628, 1995.

[32] JL Brédas, J Cornil, and A J Heeger. The exciton binding energy in luminescent conjugated polymers. *Adv. Mater.*, 8:447, 1996.

[33] P G Dacosta and E M Conwell. Excitons and the band-gap in poly(phenylene vinylene). *Phys. Rev. B*, 48:1993–1996, 1993.

[34] J M Leng, S Jeglinski, X Wei, R E Benner, Z V Vardeny, F Guo, and S Mazumdar. Optical probes of excited-states in poly(p-phenylenevinylene). *Phys. Rev. Lett.*, 72:156–159, 1994.

[35] H S Woo, O Lhost, S C Graham, D D C Bradley, R H Friend, C Quattrocchi, JL Brédas, R Schenk, and K. Müllen. Optical-spectra and excitations in phenylene vinylene oligomers. *Synth. Met.*, 59:13–28, 1993.

[36] Charles Swenberg Martin Pope. *Electronic Processes in Organic Crystals and Polymers*. Monographs on the Physics and Chemistry of Materials. Oxford Science Publications, second edition, 1999.

[37] D. R. Baigent, R. H. Friend, A. B. Holmes, and S. C. Moratti. *Electronic processes associated with electroluminescence in conjugated polymers*, volume 81 of *Springer proceedings in physics*, page 231. Springer, Tokyo, 1996.

[38] M B Johnston, L M Herz, A L T Khan, A. Köhler, A G Davies, and E H Linfield. Low-energy vibrational modes in phenylene oligomers studied by thz time-domain spectroscopy. *Chem. Phys. Lett.*, 377:256–262, 2003.

[39] Charles Kittel. *Introduction to Solid State Physics*. Wiley, seventh edition, 1995.

[40] R F Mahrt and H Bässler. Light and heavy excitonic polarons in conjugated polymers. *Synth. Met.*, 45:107, 1991.

[41] Michael Kasha. Characterization of electronic transitions in complex molecules. *Discussions of the Faraday Society*, 9:14–19, 1950.

[42] A. Kearwell and F. Wilkinson. *Chemistry of electronically excited states of organic molecules*, volume 1 of *Transfer and Storage of Energy by Molecules*, pages 94–161. Wiley Interscience, London, 1969.

[43] M H Chang, M J Frampton, H L Anderson, and L M Herz. Photoexcitation dynamics in thin films of insulated molecular wires. *Appl. Phys. Lett.*, 89: 232110, 2006.

[44] J Y Kim, S H Kim, H H Lee, K Lee, W L Ma, X Gong, and A J Heeger. New architecture for high-efficiency polymer photovoltaic cells using solution-based titanium oxide as an optical spacer. *Adv. Mater.*, 18:572, 2006.

[45] D Beljonne, G Pourtois, C Silva, E Hennebicq, L M Herz, R H Friend, G D Scholes, S Setayesh, K. Müllen, and JL Brédas. Interchain vs. intrachain energy transfer in acceptor-capped conjugated polymers. *Proc. Natl. Acad. Sci. U. S. A.*, 99:10982–10987, 2002.

[46] B Movaghar, M Grunewald, B Ries, H Bässler, and D Wurtz. Diffusion and relaxation of energy in disordered organic and inorganic materials. *Phys. Rev. B*, 33:5545–5554, 1986.

[47] T Q Nguyen, I B Martini, J Liu, and B J Schwartz. Controlling interchain interactions in conjugated polymers: the effects of chain morphology on exciton-exciton annihilation and aggregation in meh-ppv films. *J. Phys. Chem. B*, 104: 237, 2000.

[48] Bernard Valeur. *Molecular fluorescence : principles and applications*. Wiley-VCH, first edition, 2002.

[49] M H Chang, M J Frampton, H L Anderson, and L M Herz. Intermolecular interaction effects on the ultrafast depolarization of the optical emission from conjugated polymers. *Phys. Rev. Lett.*, 98:027402, 2007.

[50] JG Müller, U Lemmer, G Raschke, M Anni, U Scherf, J M Lupton, and J Feldmann. Linewidth-limited energy transfer in single conjugated polymer molecules. *Phys. Rev. Lett.*, 91:267403, 2003.

[51] P Parkinson, E Aharon, M H Chang, C Dosche, G L Frey, A. Köhler, and L M Herz. Dimensionality-dependent energy transfer in polymer-intercalated SnS_2 nanocomposites. *Phys. Rev. B*, 75:165206, 2007.

[52] M Theander, A Yartsev, D Zigmantas, Villy Sundström, W Mammo, M R Andersson, and Olle Inganäs. Photoluminescence quenching at a polythiophene/C_60 heterojunction. *Phys. Rev. B*, 61:12957, 2000.

[53] R Kersting, U Lemmer, R F Mahrt, K Leo, H Kurz, H Bässler, and EO Göbel. Femtosecond energy relaxation in pi-conjugated polymers. *Phys. Rev. Lett.*, 70: 3820–3823, 1993.

[54] E E Nesterov, Z G Zhu, and T M Swager. Conjugation enhancement of intramolecular exciton migration in poly(p-phenylene ethynylene)s. *J. Am. Chem. Soc.*, 127:10083–10088, 2005.

[55] R E Palacios and P F Barbara. Single molecule spectroscopy of poly 3-octylthiophene (P3OT). *J. Fluoresc.*, 17:749, 2007.

[56] K Kanemoto, T Sudo, I Akai, H Hashimoto, T Karasawa, Y Aso, and T Otsubo. Intrachain photoluminescence properties of conjugated polymers as revealed by long oligothiophenes and polythiophenes diluted in an inactive solid matrix. *Phys. Rev. B*, 73:235203, 2006.

[57] F. Perrin. Theorie de la fluorescence polarise (influence de la viscosite). *Compt. Rend.*, 180:581, 1925.

[58] F. Perrin. Polarisation de la lumiére de fluorescence. vie moyenne des molécules dans l'etat excité. *J. Phys. Radium.*, 7:390–401, 1926.

[59] T. Förster. Zwischemolekular Energiewanderung und Fluoreszenz. *Annalen der Physik*, 2:55, 1948.

[60] T. Förster. 10th spiers memorial lecture. transfer mechanisms of electronic excitation. *Discuss. Faraday Soc.*, 27:7–17, 1959.

[61] J Clark, C Silva, R H Friend, and F C Spano. Role of intermolecular coupling in the photophysics of disordered organic semiconductors: aggregate emission in regioregular polythiophene. *Phys. Rev. Lett.*, 98:206406, 2007.

[62] F C Spano. Modeling disorder in polymer aggregates: the optical spectroscopy of regioregular poly(3-hexylthiophene) thin films. *J. Chem. Phys.*, 122:234701, 2005.

[63] V M Kenkre and R S Knox. Generalized-master-equation theory of excitation transfer. *Phys. Rev. B*, 9:5279–5290, 1974.

[64] V M Kenkre and R S Knox. Theory of fast and slow excitation transfer rates. *Phys. Rev. Lett.*, 33:803–806, 1974.

[65] R C Powell and Z G Soos. Singlet exciton energy-transfer in organic solids. *J. Lumines.*, 11:1, 1975.

[66] L M Herz, C Daniel, C Silva, F J M Hoeben, A P H J Schenning, E W Meijer, R H Friend, and R T Phillips. Exciton dynamics in supramolecular assemblies of p-phenylenevinylene oligomers. *Synth. Met.*, 139:839–842, 2003.

[67] Laura Maria Herz. *Aggreagation effects in conjugated polymer films studied by time-resolved photoluminescence spectroscopy.* PhD thesis, Cambridge, Nov 2001.

[68] C F Wang, J D White, T L Lim, J H Hsu, S C Yang, W S Fann, K Y Peng, and S A Chen. Illumination of exciton migration in rodlike luminescent conjugated polymers by single-molecule spectroscopy. *Phys. Rev. B*, 67:035202, 2003.

[69] M H Chang, F J M Hoeben, P Jonkheijm, A P H J Schenning, E W Meijer, C Silva, and L M Herz. Influence of mesoscopic ordering on the photoexcitation transfer dynamics in supramolecular assemblies of oligo-p-phenylenevinylene. *Chem. Phys. Lett.*, 418:196–201, 2006.

[70] L. Onsager. Initial recombination of ions. *Phys. Rev.*, 54:554, 1938.

[71] D M Pai and R C Enck. Onsager mechanism of photogeneration in amorphous selenium. *Phys. Rev. B*, 11:5163, 1975.

[72] S Barth and H Bässler. Intrinsic photoconduction in PPV-type conjugated polymers. *Phys. Rev. Lett.*, 79:4445, 1997.

[73] S V Frolov, Z Bao, M Wohlgenannt, and Z V Vardeny. Ultrafast spectroscopy of even-parity states in pi-conjugated polymers. *Phys. Rev. Lett.*, 85:2196, 2000.

[74] A. Köhler, D Beljonne, Z Shuai, JL Brédas, A B Holmes, A Kraus, K. Müllen, and R H Friend. Charge separation in localized and delocalized electronic states in polymeric semiconductors. *Nature*, 392:903, 1998.

[75] V I Arkhipov, E V Emelianova, and H Bässler. Hot exciton dissociation in a conjugated polymer. *Phys. Rev. Lett.*, 82:1321, 1999.

[76] V I Arkhipov, E V Emelianova, S Barth, and H Bässler. Ultrafast on-chain dissociation of hot excitons in conjugated polymers. *Phys. Rev. B*, 61:8207–8214, 2000.

[77] U Albrecht and H Bässler. Yield of geminate pair dissociation in an energetically random hopping system. *Chem. Phys. Lett.*, 235:389, 1995.

[78] H Sirringhaus, P J Brown, R H Friend, M M Nielsen, K Bechgaard, B M W Langeveld-Voss, A J H Spiering, R A J Janssen, E W Meijer, and P Herwig. Two-dimensional charge transport in self-organized, high-mobility conjugated polymers. *Nature*, 401:685–688, 1999.

[79] G Dicker, L D A Siebbeles, and J M Warman. Electrodeless time-resolved microwave conductivity study of charge-carrier photogeneration in regioregular poly(3-hexylthiophene) thin films. *Phys. Rev. B*, 70:045203, 2004.

[80] C Silva, A S Dhoot, D M Russell, M A Stevens, A C Arias, J D MacKenzie, N C Greenham, R H Friend, S Setayesh, and K. Müllen. Efficient exciton dissociation via two-step photoexcitation in polymeric semiconductors. *Phys. Rev. B*, 6412:125211, 2001.

[81] I W Hwang, D Moses, and A J Heeger. Photoinduced carrier generation in P3HT/PCBM bulk heterojunction materials. *J. Phys. Chem. C*, 112:4350, 2008.

[82] JG Müller, J M Lupton, J Feldmann, U Lemmer, M C Scharber, N S Sariciftci, C J Brabec, and U Scherf. Ultrafast dynamics of charge carrier photogeneration and geminate recombination in conjugated polymer : fullerene solar cells. *Phys. Rev. B*, 72:195208, 2005.

[83] N S Sariciftci, L Smilowitz, A J Heeger, and F Wudl. Photoinduced electron-transfer from a conducting polymer to buckminsterfullerene. *Science*, 258:1474, 1992.

[84] J J M Halls, C A Walsh, N C Greenham, E A Marseglia, R H Friend, S C Moratti, and A B Holmes. Efficient photodiodes from interpenetrating polymer networks. *Nature*, 376:498–500, 1995.

[85] G Yu, J Gao, J C Hummelen, F Wudl, and A J Heeger. Polymer photovoltaic cells - enhanced efficiencies via a network of internal donor-acceptor heterojunctions. *Science*, 270:1789–1791, 1995.

[86] A C Morteani, P Sreearunothai, L M Herz, R H Friend, and C Silva. Exciton regeneration at polymeric semiconductor heterojunctions. *Phys. Rev. Lett.*, 92: 247402, 2004.

[87] L Goris, A Poruba, L Hod'akova, M Vanecek, K Haenen, M Nesladek, P Wagner, D Vanderzande, and J V Manca. Observation of the subgap optical absorption in polymer-fullerene blend solar cells. *Appl. Phys. Lett.*, 88:052113, 2006.

[88] J J Benson-Smith, L Goris, K Vandewal, K Haenen, J V Manca, D Vanderzande, D D C Bradley, and J Nelson. Formation of a ground-state charge-transfer complex in polyfluorene [6,6]-phenyl-c_{61} butyric acid methyl ester (PCBM) blend films and its role in the function of polymer/PCBM solar cells. *Adv. Funct. Mater.*, 17:451–457, 2007.

[89] K Kim, J Liu, M A G Namboothiry, and D L Carroll. Roles of donor and acceptor nanodomains in 6annealed polymer photovoltaics. *Appl. Phys. Lett.*, 90:163511, 2007.

[90] M Dante, J Peet, and T Q Nguyen. Nanoscale charge transport and internal structure of bulk heterojunction conjugated polymer/fullerene solar cells by scanning probe microscopy. *J. Phys. Chem. C*, 112:7241–7249, 2008.

[91] Y Kim, S A Choulis, J Nelson, D D C Bradley, S Cook, and J R Durrant. Device annealing effect in organic solar cells with blends of regioregular poly(3-hexylthiophene) and soluble fullerene. *Appl. Phys. Lett.*, 86:063502, 2005.

[92] G Li, V Shrotriya, J S Huang, Y Yao, T Moriarty, K Emery, and Y Yang. High-efficiency solution processable polymer photovoltaic cells by self-organization of polymer blends. *Nat. Mater.*, 4:864–868, 2005.

[93] F C Grozema and L D A Siebbeles. Mechanism of charge transport in self-organizing organic materials. *Int. Rev. Phys. Chem.*, 27:87–138, 2008.

[94] O Ostroverkhova, D G Cooke, S Shcherbyna, R F Egerton, F A Hegmann, R R Tykwinski, and J E Anthony. Bandlike transport in pentacene and functionalized pentacene thin films revealed by subpicosecond transient photoconductivity measurements. *Phys. Rev. B*, 71:035204, 2005.

[95] V C Sundar, J Zaumseil, V Podzorov, E Menard, R L Willett, T Someya, M E Gershenson, and J A Rogers. Elastomeric transistor stamps: reversible probing of charge transport in organic crystals. *Science*, 303:1644–1646, 2004.

[96] C Tanase, E J Meijer, and P W M Blom. Unification of the hole transport in polymeric field-effect transistors and light-emitting diodes. *Phys. Rev. Lett.*, 91:216601, 2003.

[97] H Sirringhaus, N Tessler, and R H Friend. Integrated optoelectronic devices based on conjugated polymers. *Science*, 280:1741, 1998.

[98] R J Kline, M D McGehee, E N Kadnikova, J S Liu, and J M J Frechet. Controlling the field-effect mobility of regioregular polythiophene by changing the molecular weight. *Adv. Mater.*, 15:1519, 2003.

[99] H Scher and E W Montroll. Anomalous transit-time dispersion in amorphous solids. *Phys. Rev. B*, 12:2455, 1975.

[100] Y Kim, S Cook, S M Tuladhar, S A Choulis, J Nelson, J R Durrant, D D C Bradley, M Giles, I McCulloch, C S Ha, and M Ree. A strong regioregularity effect in self-organizing conjugated polymer films and high-efficiency polythiophene: fullerene solar cells. *Nat. Mater.*, 5:197–203, 2006.

[101] K R Amundson, B J Sapjeta, A J Lovinger, and Z N Bao. An in-plane anisotropic organic semiconductor based upon poly(3-hexyl thiophene). *Thin Solid Films*, 414:143, 2002.

[102] J Kirkpatrick, V Marcon, J Nelson, K Kremer, and D Andrienko. Charge mobility of discotic mesophases: A multiscale quantum and classical study. *Phys. Rev. Lett.*, 98:227402, 2007.

[103] P M Borsenberger, R Richert, and H Bässler. Dispersive and nondispersive charge transport in a molecularly doped polymer with superimposed energetic and positional disorder. *Phys. Rev. B*, 47:4289–4295, 1993.

[104] A Miller and E Abrahams. Impurity conduction at low concentrations. *Phys. Rev.*, 120:745–755, 1960.

[105] M Scheidler, U Lemmer, R Kersting, S Karg, W Riess, B Cleve, R F Mahrt, H Kurz, H Bässler, EO Göbel, and P Thomas. Monte carlo study of picosecond exciton relaxation and dissociation in poly(phenylenevinylene). *Phys. Rev. B*, 54:5536–5544, 1996.

[106] P Prins, F C Grozema, J M Schins, S Patil, U Scherf, and L D A Siebbeles. High intrachain hole mobility on molecular wires of ladder-type poly(p-phenylenes). *Phys. Rev. Lett.*, 96:146601, 2006.

[107] M C Beard, G M Turner, and C A Schmuttenmaer. Size-dependent photoconductivity in cdse nanoparticles as measured by time-resolved terahertz spectroscopy. *Nano Lett.*, 2:983–987, 2002.

[108] G Dicker, T J Savenije, B H Huisman, and J M Warman. Photoconductivity enhancement of poly(3-hexylthiophene) by increasing inter- and intra-chain order. *Synth. Met.*, 137:863–864, 2003.

[109] R J O M Hoofman, L D A Siebbeles, and J M Warman. Highly mobile electrons and holes on isolated chains of the semiconducting polymer poly(phenylenevinylene). *Nature*, 392:54–56, 1998.

[110] P Prins, F C Grozema, J M Schins, T J Savenije, S Patil, U Scherf, and L D A Siebbeles. Effect of intermolecular disorder on the intrachain charge transport in ladder-type poly(p-phenylenes). *Phys. Rev. B*, 73:045204, 2006.

[111] T J Savenije, J E Kroeze, X N Yang, and J Loos. The formation of crystalline p3ht fibrils upon annealing of a PCBM:P3HT bulk heterojunction. *Thin Solid Films*, 511:2, 2006.

[112] X Ai, M C Beard, K P Knutsen, S E Shaheen, G Rumbles, and R J Ellingson. Photoinduced charge carrier generation in a poly(3-hexylthiophene) and methanofullerene bulk heterojunction investigated by time-resolved terahertz spectroscopy. *J. Phys. Chem. B*, 110:25462–25471, 2006.

[113] P D Cunningham and L M Hayden. Carrier dynamics resulting from above and below gap excitation of P3HT and P3HT/P3HT investigated by optical-pump terahertz-probe spectroscopy. *J. Phys. Chem. C*, 112:7928, 2008.

[114] O Esenturk, J S Melinger, and E J Heilweil. Terahertz mobility measurements on poly-3-hexylthiophene films: device comparison, molecular weight, and film processing effects. *J. Appl. Phys.*, 103:023102, 2008.

[115] H Němec, H K Nienhuys, F Zhang, Olle Inganäs, A Yartsev, and Villy Sundström. Charge carrier dynamics in alternating polyfluorene copolymer: fullerene blends probed by terahertz spectroscopy. *J. Phys. Chem. C*, 112:6558, 2008.

[116] F C Grozema, Y A Berlin, M A Ratner, and L D A Siebbeles. Intramolecular charge transport along isolated chains of conjugated polymers: effect of torsional disorder and polymerization defects. *J. Phys. Chem. B*, 106:7791, 2002.

[117] E Hendry, J M Schins, L P Candeias, L D A Siebbeles, and M Bonn. Efficiency of exciton and charge carrier photogeneration in a semiconducting polymer. *Phys. Rev. Lett.*, 92:196601, 2004.

[118] J Lloyd-Hughes, T Richards, H Sirringhaus, M B Johnston, and L M Herz. Exciton dissociation in polymer field-effect transistors studied using terahertz spectroscopy. *Phys. Rev. B*, 77:125203, 2008.

[119] J Lloyd-Hughes, T Richards, H Sirringhaus, E Castro-Camus, L M Herz, and M B Johnston. Charge trapping in polymer transistors probed by terahertz spectroscopy and scanning probe potentiometry. *Appl. Phys. Lett.*, 89:112101, 2006.

[120] A Salleo, F Endicott, and R A Street. Reversible and irreversible trapping at room temperature in poly(thiophene) thin-film transistors. *Appl. Phys. Lett.*, 86:263505, 2005.

[121] L Bürgi, T Richards, M Chiesa, R H Friend, and H Sirringhaus. A microscopic view of charge transport in polymer transistors. *Synth. Met.*, 146:297–309, 2004.

[122] R.A Smith. *Semiconductors*. Cambridge University Press, first edition, 1959.

[123] Y Li, F Qian, J Xiang, and C M Lieber. Nanowire electronic and optoelectronic devices. *Mater. Today*, 9:18, 2006.

[124] X F Duan, Y Huang, R Agarwal, and C M Lieber. Single-nanowire electrically driven lasers. *Nature*, 421:241, 2003.

[125] A Fujiwara, K Yamazaki, and Y Takahashi. Detection of single charges and their generation-recombination dynamics in si nanowires at room temperature. *Appl. Phys. Lett.*, 80:4567, 2002.

[126] M Law, L E Greene, J C Johnson, R Saykally, and P D Yang. Nanowire dye-sensitized solar cells. *Nat. Mater.*, 4:455–459, 2005.

[127] M Law, J Goldberger, and P D Yang. Semiconductor nanowires and nanotubes. *Ann. Rev. Mater. Res.*, 34:83, 2004.

[128] P Drude. Zur elektronentheorie der metalle. *Annalen der Physik*, 306:566–613, 1900.

[129] W Shockley and W T Read. Statistics of the recombinations of holes and electrons. *Phys. Rev.*, 87:835–842, 1952.

[130] M V Lebedev. Surface modification of III-V semiconductors: chemical processes and electronic properties. *Prog. Surf. Sci.*, 70:153–186, 2002.

[131] L V Titova, T B Hoang, H E Jackson, L M Smith, J M Yarrison-Rice, Y Kim, H J Joyce, H H Tan, and C Jagadish. Temperature dependence of photoluminescence from single core-shell GaAs-AlGaAs nanowires. *Appl. Phys. Lett.*, 89: 173126, 2006.

[132] E Yablonovitch, C J Sandroff, R Bhat, and T Gmitter. Nearly ideal electronic-properties of sulfide coated GaAs-surfaces. *Appl. Phys. Lett.*, 51:439–441, 1987.

[133] J Lloyd-Hughes, S K E Merchant, L Fu, H H Tan, C Jagadish, E Castro-Camus, and M B Johnston. Influence of surface passivation on ultrafast carrier dynamics and terahertz radiation generation in GaAs. *Appl. Phys. Lett.*, 89:232102, 2006.

[134] D Pines and D Bohm. A collective description of electron interactions: Ii. collective *vs* individual particle aspects of the interactions. *Phys. Rev.*, 85: 338–353, 1952.

[135] R H Ritchie. Plasma losses by fast electrons in thin films. *Phys. Rev.*, 1:874–881, 1957.

[136] J M Pitarke, V M Silkin, E V Chulkov, and P M Echenique. Theory of surface plasmons and surface-plasmon polaritons. *Rep. Prog. Phys.*, 70:1–87, 2007.

[137] P P Infelta, M P D Haas, and J M Warman. Study of transient conductivity of pulse irradiated dielectric liquids on a nanosecond timescale using microwaves. *Radiat. Phys. Chem.*, 10:353–365, 1977.

[138] Paul Horowitz and Winfield Hill. *The Art of Electronics*. Cambridge University Press, first edition, 1980.

[139] S N Vainshtein, V S Yuferev, and J I Kostamovaara. Analyses of the picosecond range transient in a high-power switch based on a bipolar gaas transistor structure. *IEEE Trans. Electron Devices*, 52:2760–2768, 2005.

[140] J D Simon. Ultrashort light pulses. *Rev. Sci. Instrum.*, 60:3597–3624, 1989.

[141] J Squier, F Salin, G Mourou, and D Harter. 100-fs pulse generation and amplification in Ti:Al_2O_3. *Opt. Lett.*, 16:324–326, 1991.

[142] Spectra-Physics. Spitfire pro manual, March 2005.

[143] Robert R. Alfano. *The Supercontinuum Laser Source*. Springer, second edition, 2006.

[144] Claude Rullière, editor. *Femtosecond Laser Pulses : Principles and Experiments*. Springer-Verlag, first edition, 1998.

[145] D N Nikogosyan. Beta barium borate (BBO). *Appl. Phys. A-Mater. Sci. Process.*, 52:359, 1991.

[146] Paul Lorrain, Dale Corson, and Francois Lorrain. *Electromagnetic Fields and Waves*. W.H. Freeman, third edition, 1988.

[147] John Jackson. *Classical electrodynamics*. Wiley, third edition, 1999.

[148] G L Dakovski, B Kubera, S Lan, and J Shan. Finite pump-beam-size effects in optical pump-terahertz probe spectroscopy. *J. Opt. Soc. Am. B-Opt. Phys.*, 23:139–141, 2006.

[149] M C Beard, G M Turner, and C A Schmuttenmaer. Transient photoconductivity in GaAs as measured by time-resolved terahertz spectroscopy. *Phys. Rev. B*, 62:15764–15777, 2000.

[150] L Xu, X C Zhang, and D H Auston. Terahertz beam generation by femtosecond optical pulses in electrooptic materials. *Appl. Phys. Lett.*, 61:1784, 1992.

[151] A Rice, Y Jin, X F Ma, X C Zhang, D Bliss, J Larkin, and M Alexander. Terahertz optical rectification from ¡110¿ zincblende crystals. *Appl. Phys. Lett.*, 64:1324, 1994.

[152] Q Wu, M Litz, and X C Zhang. Broadband detection capability of znte electro-optic field detectors. *Appl. Phys. Lett.*, 68:2924–2926, 1996.

[153] C Winnewisser, P U Jepsen, M Schall, V Schyja, and H Helm. Electro-optic detection of THz radiation in $LiTaO_3$, $LiNbO_3$, and ZnTe. *Appl. Phys. Lett.*, 70:3069, 1997.

[154] J Shan, A Nahata, and T F Heinz. Terahertz time-domain spectroscopy based on nonlinear optics. *J. Nonlinear Opt. Phys. Mater.*, 11:31–48, 2002.

[155] J A Valdmanis, G A Mourou, and C W Gabel. Subpicosecond electrical sampling. *IEEE J. Quantum Electron.*, 19:664–667, 1983.

[156] Kiyomi Sakai, editor. *Terahertz Optoelectronics*. Topics in Applied Physics. Springer, first edition, 2005.

[157] E Hendry, M Koeberg, J M Schins, H K Nienhuys, Villy Sundström, L D A Siebbeles, and A Bonn. Interchain effects in the ultrafast photophysics of a semiconducting polymer: THz time-domain spectroscopy of thin films and isolated chains in solution. *Phys. Rev. B*, 71:125201, 2005.

[158] H K Nienhuys and Villy Sundström. Intrinsic complications in the analysis of optical-pump, terahertz probe experiments. *Phys. Rev. B*, 71:235110, 2005.

[159] L Duvillaret, F Garet, and J L Coutaz. A reliable method for extraction of material parameters in terahertztime-domain spectroscopy. *IEEE J. Sel. Top. Quantum Electron.*, 2:739–746, 1996.

[160] K P H Lui and F A Hegmann. Ultrafast carrier relaxation in radiation-damaged silicon on sapphire studied by optical-pump–terahertz-probe experiments. *Appl. Phys. Lett.*, 78:3478–3480, 2001.

[161] P Kužel, F Kadlec, and H Němec. Propagation of terahertz pulses in photoexcited media: Analytical theory for layered systems. *J. Chem. Phys.*, 127:11, 2007.

[162] Euan Hendry. *Charge Dynamics in Novel Semiconductors*. PhD thesis, Universiteit van Amsterdam, 2005.

[163] Otfried Madelung, editor. *Semiconductors, basic data*. Springer, second edition, 1996.

[164] J Lloyd-Hughes, D Prabhakaran, A T Boothroyd, and M B Johnston. Low-energy collective dynamics of charge stripes in the doped nickelate $La_{2-x}Sr_xNiO_{4+\delta}$ observed with optical conductivity measurements. *Phys. Rev. B*, 77:195114, 2008.

[165] H K Nienhuys and Villy Sundström. Influence of plasmons on terahertz conductivity measurements. *Appl. Phys. Lett.*, 87:012101, 2005.

[166] P Parkinson, J Lloyd-Hughes, Q Gao, H H Tan, C Jagadish, M B Johnston, and L M Herz. Transient terahertz conductivity of GaAs nanowires. *Nano Lett.*, 7:2162–2165, 2007.

[167] M C Beard, G M Turner, J E Murphy, O I Micic, M C Hanna, A J Nozik, and C A Schmuttenmaer. Electronic coupling in inp nanoparticle arrays. *Nano Lett.*, 3:1695–1699, 2003.

[168] N V Smith. Classical generalization of the drude formula for the optical conductivity. *Phys. Rev. B*, 64:155106, 2001.

[169] D W Davidson and R H Cole. Dielectric relaxation in glycerol, propylene glycol, and n-propanol. *J. Chem. Phys.*, 19:1484–1490, 1951.

[170] K S Cole and R H Cole. Dispersion and absorption in dielectrics i. alternating current characteristics. *J. Chem. Phys.*, 9:341–351, 1941.

[171] R A Kaindl, M A Carnahan, D Hagele, R Lovenich, and D S Chemla. Ultrafast terahertz probes of transient conducting and insulating phases in an electron-hole gas. *Nature*, 423:734–738, 2003.

[172] R H M Groeneveld and D Grischkowsky. Picosecond time-resolved far-infrared experiments on carriers and excitons in GaAs-AlGaAs multiple-quantum wells. *J. Opt. Soc. Am. B-Opt. Phys.*, 11:2502, 1994.

[173] J Cerne, J Kono, M S Sherwin, M Sundaram, A C Gossard, and G E W Bauer. Terahertz dynamics of excitons in gaas/algaas quantum wells. *Phys. Rev. Lett.*, 77:1131, 1996.

[174] J Lloyd-Hughes, H E Beere, D A Ritchie, and M B Johnston. Terahertz magnetoconductivity of excitons and electrons in quantum cascade structures. *Phys. Rev. B*, 77:125322, 2008.

[175] J S Huang, G Li, E Wu, Q F Xu, and Y Yang. Achieving high-efficiency polymer white-light-emitting devices. *Adv. Mater.*, 18:114–117, 2006.

[176] N Ananthakrishnan, G Padmanaban, S Ramakrishnan, and J R Reynolds. Tuning polymer light-emitting device emission colors in ternary blends composed of conjugated and nonconjugated polymers. *Macromolecules*, 38:7660, 2005.

[177] T W Lee, O O Park, H N Cho, J M Hong, C Y Kim, and Y C Kim. White emission from a ternary polymer blend by incomplete cascade energy transfer. *Synth. Met.*, 122:437–441, 2001.

[178] E Aharon, A Albo, M Kalina, and G L Frey. Stable blue emission from a polyfluorene/layered-compound guest/host nanocomposite. *Adv. Funct. Mater.*, 16:980–986, 2006.

[179] E Hennebicq, G Pourtois, G D Scholes, L M Herz, D M Russell, C Silva, S Setayesh, A C Grimsdale, K. Müllen, JL Brédas, and D Beljonne. Exciton migration in rigid-rod conjugated polymers: an improved förster model. *J. Am. Chem. Soc.*, 127:4744, 2005.

[180] T Q Nguyen, J J Wu, V Doan, B J Schwartz, and S H Tolbert. Control of energy transfer in oriented conjugated polymer-mesoporous silica composites. *Science*, 288:652–656, 2000.

[181] T Q Nguyen, J Wu, S H Tolbert, and B J Schwartz. Control of energy transport in conjugated polymers using an ordered mesoporous silica matrix. *Adv. Mater.*, 13:609, 2001.

[182] M G Kanatzidis, R Bissessur, D C Degroot, J L Schindler, and C R Kannewurf. New intercalation compounds of conjugated polymers - encapsulation of polyaniline in mos_2. *Chem. Mat.*, 5:595–596, 1993.

[183] G D Scholes. Long-range resonance energy transfer in molecular systems. *Annu. Rev. Phys. Chem.*, 54:57–87, 2003.

[184] P Anfinrud, R L Crackel, and W S Struve. Excitation transport and trapping in a two-dimensional disordered system - cresyl violet on quartz. *J. Phys. Chem.*, 88:5873–5882, 1984.

[185] J Baumann and M D Fayer. Excitation transfer in disordered two-dimensional and anisotropic 3-dimensional systems - effects of spatial geometry on time-resolved observables. *J. Chem. Phys.*, 85:4087–4107, 1986.

[186] A Dogariu, R Gupta, A J Heeger, and H Wang. Time-resolved förster energy transfer in polymer blends. *Synth. Met.*, 100:95–100, 1999.

[187] L M Herz, C Silva, A C Grimsdale, K. Müllen, and R T Phillips. Time-dependent energy transfer rates in a conjugated polymer guest-host system. *Phys. Rev. B*, 70:165207, 2004.

[188] P K Wolber and B S Hudson. Analytic solution to the förster energy-transfer problem in 2 dimensions. *Biophys. J.*, 28:197–210, 1979.

[189] S Karabunarliev, M Baumgarten, E R Bittner, and K. Müllen. Rigorous franck-condon absorption and emission spectra of conjugated oligomers from quantum chemistry. *J. Chem. Phys.*, 113:11372, 2000.

[190] S Karabunarliev, E R Bittner, and M Baumgarten. Franck-condon spectra and electron-libration coupling in para-polyphenyls. *J. Chem. Phys.*, 114:5863–5870, 2001.

[191] A Blumen and J Manz. Concentration and time-dependence of the energy-transfer to randomly distributed acceptors. *J. Chem. Phys.*, 71:4694–4702, 1979.

[192] Michael Hobson Kenneth Riley and Stephen Bence. *Mathematical methods for physics and engineering*. Cambridge University Press, third edition, 2006.

[193] G Duportail, F Merola, and P Lianos. Fluorescence energy-transfer in lipid vesicles - a time-resolved analysis using stretched exponentials. *J. Photochem. Photobiol. A-Chem.*, 89:135–140, 1995.

[194] M M L Grage, Y Zaushitsyn, A Yartsev, M Chachisvilis, Villy Sundström, and T Pullerits. Ultrafast excitation transfer and trapping in a thin polymer film. *Phys. Rev. B*, 67:205207, 2003.

[195] J Cornil, X Crispin, R Silbey, and JL Brédas. Influence of interchain interactions on the absorption and luminescence of conjugated oligomers and polymers: A quantum-chemical characterization. *J. Am. Chem. Soc.*, 120:1289–1299, 1998.

[196] B S Robinson, A J Kerman, E A Dauler, R O Barron, D O Caplan, M L Stevens, J J Carney, S A Hamilton, J K W Yang, and K K Berggren. 781 Mbit/s photon-counting optical communications using a superconducting nanowire detector. *Opt. Lett.*, 31:444, 2006.

[197] Y Cui, Z H Zhong, D L Wang, W U Wang, and C M Lieber. High performance silicon nanowire field effect transistors. *Nano Lett.*, 3:149, 2003.

[198] C A Schmuttenmaer. Exploring dynamics in the far-infrared with terahertz spectroscopy. *Chem. Rev.*, 104:1759–1779, 2004.

[199] D G Cooke, A N MacDonald, A Hryciw, J Wang, Q Li, A Meldrum, and F A Hegmann. Transient terahertz conductivity in photoexcited silicon nanocrystal films. *Phys. Rev. B*, 73:193311, 2006.

[200] P U Jepsen, W Schairer, I H Libon, U Lemmer, N E Hecker, M Birkholz, K Lips, and M Schall. Ultrafast carrier trapping in microcrystalline silicon observed in optical pump-terahertz probe measurements. *Appl. Phys. Lett.*, 79:1291, 2001.

[201] J B Baxter and C A Schmuttenmaer. Conductivity of ZnO nanowires, nanoparticles, and thin films using time-resolved terahertz spectroscopy. *J. Phys. Chem. B*, 110:25229, 2006.

[202] Y Kim, H J Joyce, O Gao, H H Tan, C Jagadish, M Paladugu, J Zou, and A A Suvorova. Influence of nanowire density on the shape and optical properties of ternary InGaAs nanowires. *Nano Lett.*, 6:599, 2006.

[203] A V Zayats and I I Smolyaninov. Near-field photonics: surface plasmon polaritons and localized surface plasmons. *J. Opt. A-Pure Appl. Opt.*, 5:S16–S50, 2003.

[204] X L Wang and V Voliotis. Epitaxial growth and optical properties of semiconductor quantum wires. *J. Appl. Phys.*, 99:121301, 2006.

[205] G W Bryant and W Jaskolski. Surface effects on capped and uncapped nanocrystals. *J. Phys. Chem. B*, 109:19650–19656, 2005.

[206] R Huber, F Tauser, A Brodschelm, M Bichler, G Abstreiter, and A Leitenstorfer. How many-particle interactions develop after ultrafast excitation of an electron-hole plasma. *Nature*, 414:286–289, 2001.

[207] C J Sandroff, R N Nottenburg, J C Bischoff, and R Bhat. Dramatic enhancement in the gain of a GaAs/AlGaAs heterostructure bipolar-transistor by surface chemical passivation. *Appl. Phys. Lett.*, 51:33–35, 1987.

[208] V N Bessolov and M V Lebedev. Chalcogenide passivation of III-V semiconductor surfaces. *Semiconductors*, 32:1141–1156, 1998.

[209] T B Hoang, L V Titova, J M Yarrison-Rice, H E Jackson, A O Govorov, Y Kim, H J Joyce, H H Tan, C Jagadish, and L M Smith. Resonant excitation and imaging of nonequilibrium exciton spins in single core-shell GaAs-AlGaAs nanowires. *Nano Lett.*, 7:588–595, 2007.

[210] P Parkinson, J Lloyd-Hughes, M B Johnston, and L M Herz. Efficient generation of charges via below-gap photoexcitation of polymer-fullerene blend films investigated by terahertz spectroscopy. *Phys. Rev. B*, 78:115321, 2008.

[211] C J Brabec, F Padinger, N S Sariciftci, and J C Hummelen. Photovoltaic properties of conjugated polymer/methanofullerene composites embedded in a polystyrene matrix. *J. Appl. Phys.*, 85:6866, 1999.

[212] L M Herz, C Silva, R T Phillips, S Setayesh, and K. Müllen. Exciton migration to chain aggregates in conjugated polymers: influence of side-chain substitution. *Chem. Phys. Lett.*, 347:318, 2001.

[213] G Dicker, J M Warman, and L D A Siebbeles. The disperse charge-carrier kinetics in regioregular poly(3-hexylthiophene). *J. Phys. Chem. B*, 108:17818, 2004.

[214] P J Brown, D S Thomas, A. Köhler, J S Wilson, J S Kim, C M Ramsdale, H Sirringhaus, and R H Friend. Effect of interchain interactions on the absorption and emission of poly(3-hexylthiophene). *Phys. Rev. B*, 67:064203, 2003.

[215] V Gulbinas, Y Zaushitsyn, H Bässler, A Yartsev, and Villy Sundström. Dynamics of charge pair generation in ladder-type poly(para-phenylene) at different excitation photon energies. *Phys. Rev. B*, 70:035215, 2004.

[216] E Hendry, M Koeberg, J M Schins, L D A Siebbeles, and M Bonn. Free carrier photogeneration in polythiophene versus poly(phenylene vinylene) studied with thz spectroscopy. *Chem. Phys. Lett.*, 432:441, 2006.

[217] M Koeberg, E Hendry, J M Schins, C F J Flipse, K Reimann, M Woerner, T Elsaesser, and M Bonn. Simultaneous ultrafast probing of intramolecular vibrations and photoinduced charge carriers in rubrene using broadband time-domain THz spectroscopy. *Phys. Rev. B*, 75:195216, 2007.

[218] P Prins, F C Grozema, and L D A Siebbeles. Efficient charge transport along phenylene-vinylene molecular wires. *J. Phys. Chem. B*, 110:14659, 2006.

[219] Y Zaushitsyn, V Gulbinas, D Zigmantas, F Zhang, Olle Inganäs, Villy Sundström, and A Yartsev. Ultrafast light-induced charge pair formation dynamics in poly[3-(2'-methoxy-5' octylphenyl)thiophene]. *Phys. Rev. B*, 70:075202, 2004.

[220] C Soci, D Moses, Q H Xu, and A J Heeger. Charge-carrier relaxation dynamics in highly ordered poly(p-phenylene vinylene): Effects of carrier bimolecular recombination and trapping. *Phys. Rev. B*, 72:245204, 2005.

[221] P Sreearunothai, A C Morteani, I Avilov, J Cornil, D Beljonne, R H Friend, R T Phillips, C Silva, and L M Herz. Influence of copolymer interface orientation on the optical emission of polymeric semiconductor heterojunctions. *Phys. Rev. Lett.*, 96:117403, 2006.

[222] T I Jeon, D Grischkowsky, A K Mukherjee, and R Menon. Electrical and optical characterization of conducting poly-3-methylthiophene film by THz time-domain spectroscopy. *Appl. Phys. Lett.*, 79:4142–4144, 2001.

[223] T I Jeon, D Grischkowsky, A K Mukherjee, and R Menon. Electrical and optical characterization of conducting poly-3-methylthiophene film by THz time-domain spectroscopy (vol 79, pg 4142, 2001). *Appl. Phys. Lett.*, 81:2902, 2002.

[224] T I Jeon, D Grischkowsky, A K Mukherjee, and R Menon. Electrical characterization of conducting polypyrrole by thz time-domain spectroscopy. *Appl. Phys. Lett.*, 77:2452, 2000.

[225] T I Jeon, D Grischkowsky, A K Mukherjee, and R Menon. Electrical and optical characterization of conducting polymers by thz time-domain spectroscopy. *Synth. Met.*, 135:451, 2003.

[226] I W Hwang, C Soci, D Moses, Z G Zhu, D Waller, R Gaudiana, C J Brabec, and A J Heeger. Ultrafast electron transfer and decay dynamics in a small band gap bulk heterojunction material. *Adv. Mater.*, 19:2307, 2007.

[227] M A Loi, S Toffanin, M Muccini, M Forster, U Scherf, and M Scharber. Charge transfer excitons in bulk heterojunctions of a polyfluorene copolymer and a fullerene derivative. *Adv. Funct. Mater.*, 17:2111, 2007.

[228] S Barth, H Bässler, H Rost, and H H Horhold. Extrinsic and intrinsic dc photoconductivity in a conjugated polymer. *Phys. Rev. B*, 56:3844, 1997.

[229] S Barth, H Bässler, U Scherf, and K. Müllen. Photoconduction in thin films of a ladder-type poly-para-phenylene. *Chem. Phys. Lett.*, 288:147, 1998.

[230] M Wohlgenannt, W Graupner, G Leising, and Z V Vardeny. Photogeneration action spectroscopy of neutral and charged excitations in films of a ladder-type poly(para-phenylene). *Phys. Rev. Lett.*, 82:3344–3347, 1999.

[231] A Ruseckas, M Theander, M R Andersson, M Svensson, M Prato, Olle Inganäs, and Villy Sundström. Ultrafast photogeneration of inter-chain charge pairs in polythiophene films. *Chem. Phys. Lett.*, 322:136–142, 2000.

[232] C Gadermaier, G Cerullo, G Sansone, G Leising, U Scherf, and G Lanzani. Time-resolved charge carrier generation from higher lying excited states in conjugated polymers. *Phys. Rev. Lett.*, 89:117402, 2002.

[233] W Graupner, G Cerullo, G Lanzani, M Nisoli, E J W List, and G Leising. Direct observation of ultrafast field-induced charge generation in ladder-type poly(para-phenylene). *Phys. Rev. Lett.*, 81:3259–3262, 1998.

[234] JG Müller, U Lemmer, J Feldmann, and U Scherf. Precursor states for charge carrier generation in conjugated polymers probed by ultrafast spectroscopy. *Phys. Rev. Lett.*, 88:147401, 2002.

[235] X P Zhang, Y J Xia, R H Friend, and C Silva. Sequential absorption processes in two-photon-excitation transient absorption spectroscopy in a semiconductor polymer. *Phys. Rev. B*, 73:245201, 2006.

[236] S E Shaheen, C J Brabec, N S Sariciftci, F Padinger, T Fromherz, and J C Hummelen. 2.5% efficient organic plastic solar cells. *Appl. Phys. Lett.*, 78: 841–843, 2001.

[237] J Piris, N Kopidakis, D C Olson, S E Shaheen, D S Ginley, and G Rumbles. The locus of free charge-carrier generation in solution-cast $Zn_{1-x}Mg_xo$/poly(3-hexylthiophene) bilayers for photovoltaic applications. *Adv. Funct. Mater.*, 17: 3849, 2007.

[238] M Caironi, T Agostinelli, D Natali, M Sampietro, R Cugola, M Catellani, and S Luzzati. External quantum efficiency versus charge carriers mobility in polythiophene/methanofullerene based planar photodetectors. *J. Appl. Phys.*, 102:024503, 2007.

[239] E Hendry, M Koeberg, B O'Regan, and M Bonn. Local field effects on electron transport in nanostructured TiO_2 revealed by terahertz spectroscopy. *Nano Lett.*, 6:755, 2006.

[240] Tuck C. Choy. *Effective medium theory : principles and applications.* International series of monographs on physics. Oxford : Clarendon Press, 1999.

[241] J. Lloyd-Hughes. Private communication, 2008.